GALACTIC SOURCES OF ULTRAHIGH-ENERGY COSMIC RAYS

Niels C.M. Martens

MartensNiels@gmail.com

MSc Theoretical Physics, University of Groningen (s1610600)

Graduate Visiting Student, Corpus Christi College, Oxford University (s2811287)

Supervisors: Prof. O. Scholten[a,b], Dr. P. Mertsch[c], Prof. S. Sarkar[c]

[a] *Faculty of Mathematics & Natural Sciences, University of Groningen, The Netherlands*

[b] *Kernfysisch Versneller Instituut (KVI), Groningen, The Netherlands*

[c] *Rudolf Peierls Centre for Theoretical Physics, Oxford University, United Kingdom*

A thesis submitted in partial fulfillment of the requirements for the degree of

Master of Science in Theoretical Physics of the University of Groningen

August 27, 2012

Abstract

Ultrahigh-energy cosmic rays (UHECR; $E \geq 55$ EeV) are usually assumed to originate outside our Galaxy, since at these energies (1) a Milky Way of arrival directions and (2) a dipole-anisotropy in the arrival directions are expected from Galactic sources, whereas the Pierre Auger Observatory has observed UHECR from all directions and has set strict upper bounds on the dipole-anisotropy. A quantitative response to these two arguments is given, which takes into account recent suggestions of a heavier composition at these energies. Proton and iron UHECR trajectories are simulated through (several versions of) two Galactic magnetic field (GMF) models by Sun *et al* [1, 2] and one model by Jansson & Farrar [3]. Two complementary methods are used: forwardtracking of cosmic rays from specific source distributions until the Earth is reached, and backtracking of the observed arrival directions until the backtracked trajectory intersects the Galactic plane. Both methods confirm that proton UHECR indeed form a Milky Way of arrival directions. However, iron UHECR can reach most regions of the sky if either a dipole field component is added to the models by Sun *et al.*, or if their Halo field component is modified. The dipole-anisotropies obtained from forwardtracking iron UHECR from a spiral arm source distribution of 540 sources is several times the experimental upper bound, for all GMF models. Similar dipole amplitudes are obtained when the amount of sources or the energy is lowered, or when a fine-tuned source distribution is used. This rules out a Galactic origin of UHECR, even for an iron composition. It is furthermore argued that the lack of knowledge of the GMF forms the main bottleneck in the search for the extragalactic sources of UHECR, since the GMF can deflect extragalactic iron cosmic rays up to $\sim 160°$ before they reach the Earth.

Contents

Chapter 1

Introduction

The study of cosmic rays started almost a century ago [4], when physicists tried to prove that radioactivity caused the seemingly spontaneous creation of $\sim 10-20$ ions per cubic centimetre of air per second. It turned out that the actual perpetrators are energetic particles and nuclei originating outside our solar system: cosmic rays. Cosmic Ray Physics has been crucial to the development of Quantum Electrodynamics and the Electromagnetic Cascade Theory and it enables Carbon-14 dating. In the 1930s and 1940s, antimatter, pions, muons and strange particles have all been discovered through cosmic rays [5]. The large distances travelled by cosmic rays give rise to significant neutrino flavour mixing, which formed the first sign of physics beyond the standard model in the 1980s and 1990s. Moreover, Particle/Cosmic Ray Astronomy forms a valuable channel to probe the universe in addition to the limited channel of Photon Astronomy. Ever since Linsley [6] detected a cosmic ray particle with an energy of 10^{20} eV (i.e. a single nucleus with the kinetic energy of a tennis ball with a speed of 25 km/h!), cosmic ray particles have formed an invaluable probe to high energy physics, reaching an energy level of seven orders of magnitude higher than the LHC beam. Photon Astronomy, on the other hand, becomes increasingly difficult above this scale due to attenuation ($\gamma\gamma \to e^+e^-$) on the Cosmic Microwave/Infrared Background [7]. Furthermore, if the sources of cosmic rays are known, charged cosmic rays can be used to examine the structure of galactic and extragalactic magnetic field, due to the deflection of charged cosmic rays in these fields.

Although substantial progress has been made on determining the sources of cosmic rays of energies up to $\sim 10^{16} - 10^{18}$ eV, almost fifty years after Linsley's discovery we are still clueless as to the sources of cosmic rays with the highest energies. The mystery of how and where these particles are accelerated to such extreme energies poses one of the prime questions in astrophysics. Although the sources are usually assumed to be extragalactic, the reasons for this assumption are partially outdated. Recent experimental results suggest a heavier composition than usually assumed, new source types (such as magnetars) are being considered, and the galactic magnetic field models have been improved. No proper quantitative statement has been made about the possibility of galactic sources of ultrahigh-energy cosmic rays (UHECR) in the light of these new findings. Key observables that provide hints toward the origins of UHECR are the spectrum, distribution of arrival directions and the composition. Reproducing the high energy end of the spectrum with a galactic source distribution is briefly discussed by Fang, Kotera & Olinto [8, Chapter 4.6]. In this thesis we focus on reproducing the observed distribution of arrival directions with a galactic source distribution, updating and expanding upon the work of for instance Takami & Sato [9, 10, 11], Van Vliet [12] and Nagar & Matulich [13, Chapter 4.7].

We address the question whether galactic sources could be responsible for the observed distribution of arrival directions of UHECR by considering specific source distributions placed in three different models of the magnetic field of our galaxy, and by simulating the propagation of cosmic rays with varying compositions (protons and iron nuclei) emitted by these sources. In Chapter 2 we define more precisely what ultrahigh-energy cosmic rays are. Recent experimental setups and available mathematical tools are discussed, followed by an overview of current results. We furthermore examine the reasons for favouring either a galactic or extragalactic origin. Chapter 3 introduces our specific galactic candidate, the magnetar, although all further results are valid for any galactic source able to accelerate particles up to the required energy. Chapter 4 briefly recalls the behaviour or charged particles in magnetic fields, followed by a description of two recent models of our galactic magnetic field by Sun *et al.* [1, 2] and one very recent model by Jansson & Farrar [3]. One would naively expect galactic sources to produce a 'milky way of cosmic ray arrival directions', whereas the observed arrival directions are, to first approximation, spread across the whole observable sky. Therefore, our first step is to obtain arrival directions out of the galactic plane. Using the cosmic ray propgation code CRT (explained in Appendix A) to perform an initial scan over all regions in our galaxy, we find that sufficient spread can be obtained for the case of iron nuclei, although not for protons (Chapter 5). Hence, in Chapter 6 we present a second set of simulations, with specific source distributions emitting iron nuclei.

Chapter 2

Ultrahigh-energy Cosmic Rays

2.1 What are (ultrahigh-energy) cosmic rays and where do they come from?

Cosmic rays are high-energy particles incident on the Earth's atmosphere from outer space [5] (see [4] for a review and [14] for a summary of cosmic ray data). Research has mainly focussed on charged cosmic rays. The primary particles of charged cosmic rays consist of protons (∼86%), helium nuclei (∼11%), heavier nuclei (∼1%) and electrons (∼ 2%), although the composition depends on energy (see Chapter 2.4). Moreover, a small proportion is believed to consist of positrons and antiprotons from secondary origin (i.e. they are generated by interactions of the primary particles with interstellar gas). Recently, the focus of research is shifting to neutral cosmic rays such as γ-rays, neutrinos and antineutrinos.

When the (charged) primary particles approach the Earth, they interact with atoms and molecules in the atmosphere, thereby converting their large kinetic energy into the creation of millions of secondary particles through electromagnetic and hadronic cascades, the so-called air showers. These showers prevent direct detection of primary particles with surface detectors, but this would be nearly impossible anyway at the ultrahigh energies we are interested in due to the extremely low flux ($\sim 1\text{km}^{-2}\text{century}^{-1}$). On the other hand, the spread of the shower and the large number of particles involved makes detection at the Earth's surface *relatively* easy, which enables reconstruction of the energy and arrival direction of the primary particle if sufficient detailed models of the shower are available. Thus, all in all, we should thank nature for providing us with the atmosphere as a detector.

Unfortunately the reconstructed arrival directions do not point back directly towards the much sought origins of cosmic rays, due to the deflection of charged primaries in the galactic and intergalactic magnetic field. At low and intermediate energies the trajectories of charged cosmic rays through the galaxy can be approximated by a random walk through the turbulent magnetic field: the diffusive regime. Information about the origins of individual particles is completely lost. We are however interested in ultrahigh energies. Although the Pierre Auger Observatory (see Chapter 2.2) makes use of a threshold varying between 55 and 57 EeV (1 EeV = 10^{18} eV,) [15, 16] we will define UHECR as cosmic rays with an energy E $\geq$ 55 EeV. At these energies the radius of curvature is much larger than the coherence length of the turbulent magnetic field and we enter the ballistic regime, where the trajectories are governed by the large scale regular field. Hence, if the charge and regular (inter)galactic fields are known in sufficient detail one could correct for the deflection and pinpoint the origin.

The literature contains a wealth of candidates for the production of (UHE) cosmic rays, which are usually categorised into top-down and bottom-up sources. In the top-down scenario no acceleration is necessary; the particles are directly produced with the required energies, via e.g. the decay of some supermassive Big Bang relic or by the collapse of topological defects. Top-down scenarios have however been disfavoured by recent experimental results [17, 18]. In the bottom-up scenario, particles are taken at rest and accelerated all the way up to the required energies. Candidate sources require (1) sufficient energy, (2) a combination of magnetic field strength and spatial extension sufficient to contain the particles until they are accelerated to ultrahigh energies, and (3) an acceleration mechanism that is efficient enough and capable of acceleration up to the required energies (within the lifetime of the source). Of course the sources should also (4) be distributed appropriately in order to reproduce the observed arrival directions. The necessary (but not sufficient) condition 2 is usually cited as the Hillas criterium [19]; popular candidates have been plotted in the corresponding Hillas plot (see Figure 2.1). A source needs to lie above the diagonal line in order to satisfy the Hillas criterium.

2.2 Experimental apparatus

Although the size of UHECR detectors has been growing enormously ever since Linsley detected the first cosmic ray in the 10^{20} eV range with a detector covering 8 km^2 [6], the total global UHECR count is still quite low due to the extremely low flux at these energies. The three largest and most recent experimental setups are the Akeno Giant Air Shower Array (AGASA[1], 100 km^2), the High Resolution Fly's Eye (HiRes[2]) and the South Station of the Pierre Auger Observatory (PAO[3], 3000 km^2). In this thesis we will focus mostly on the results of the largest and newest detector, the PAO in Argentina. The PAO is a hybrid detector composed of both a surface array and a fluorescence detector [4]. The surface array consists of 1600 water Cherenkov tanks, placed on a triangular grid with spacings of 1.5 km. When muons, electrons, positrons or photons from the shower pass through the tank, a glow of Cherenkov light is emitted, which is being detected by photomultiplier tubes. The fluorescence detector consists of 24 telescopes distributed over four sites at the periphery of the surface array. These detectors detect the UV-light that is being produced by charged particles in the shower through nitrogen fluorescence. When these particles interact with nitrogen molecules in the atmosphere, the molecules emit light isotropically into several optical spectral bands. The spatial and temporal

[1] http://www-akeno.icrr.u-tokyo.ac.jp/AGASA
[2] http://www.cosmic-ray.org
[3] http://www.auger.org

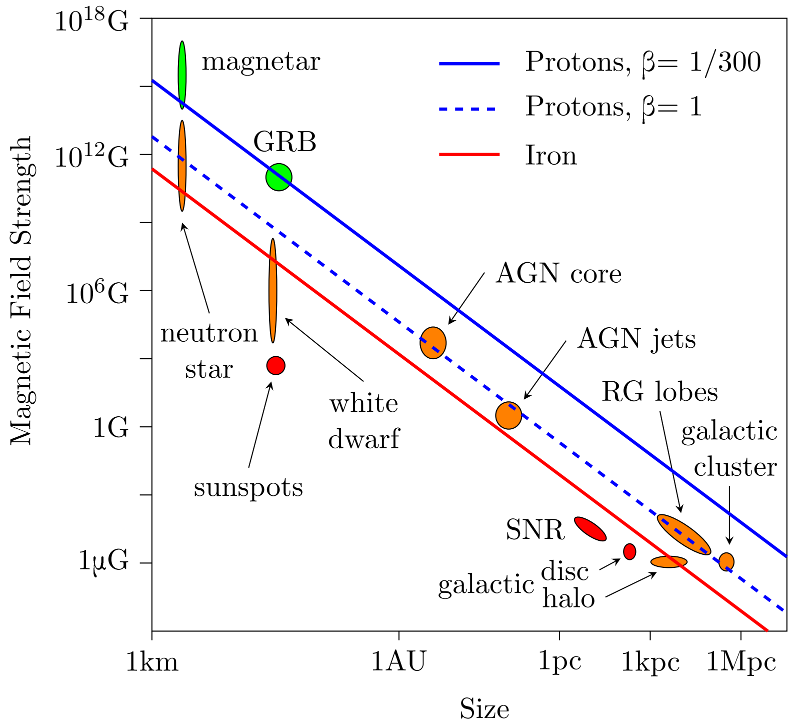

Figure 2.1: Hillas plot of popular sources in the literature (based upon [4, 19]). In order for a source to satisfy the Hillas criterium, it has to lie above the diagonal line. The solid red line corresponds to iron nuclei, the blue dashed line to protons with $\beta = 1$ and the solid blue line to protons with $\beta = 1/300$, where β represents the velocity of the accelerating shock wave or the efficiency of the accelerator. GRB = Gamma Ray Burst; AGN = Active Galactic Nucleus; SNR = Supernova Remnant; RG Lobes = Radio Galaxy Lobes.

information obtained from both the surface array and the fluorescence detectors are combined to obtain information about the arrival direction (with an angular resolution better than 1°), energy and composition of the primary cosmic rays for showers with a maximum zenith angle of 60 degrees. Due to this limit on the zenith angle and the location of the South Station on the southern hemisphere, there is no full-sky coverage, although the galactic centre can be observed. A future north station would be able to observe the remaining part of the sky.

2.3 Mathematical toolbox

In this section we discuss the mathematical toolbox available to help us find the sources of UHECR. If the sources of UHECR are not uniformly distributed, we expect that the arrival directions of cosmic rays with the highest energies are anisotropic (i.e. either a clustering of arrival directions from individual sources would be observed, or a correlation of the arrival directions with a catalogue of astronomical objects), provided that the deflections caused by intervening magnetic fields upon the cosmic ray trajectories are small enough for the arrival directions to still point back to their origin (i.e. the sources must be sufficiently nearby, have a sufficiently high energy and a sufficiently low charge) [15, 20]. Indeed, the PAO has rejected the hypothesis of isotropy [15]. This anisotropy gives valuable hints pointing towards the origins of UHECR. In order to understand these hints, the following tools are available to quantise the observed anisotropy.

2.3.1 Correlation with source catalogue

When one has a specific source candidate in mind, the correlation between a chosen course catalogue and the observed arrival directions can be calculated. Firstly, an initial data set (which is discarded afterwards) is used to optimise the relevant correlation parameters, such as the maximum angular separation allowed between a source and arrival direction ψ, the maximum distance z_{max} and the energy threshold E_{th}. ψ represents the deflection due to the magnetic field, and hence depends on the rigidity (the ratio of momentum and charge) and the length of the trajectory. Subsequently, applying these optimised parameters to a new data set, one counts the number of arrival directions which are within a maximum angular distance ψ from any one source. This value is compared to the percentage of arrival directions from an isotropic distribution which are within a maximum angular distance ψ from any one source (i.e. basically the percentage of sky covered by circles of radius ψ centred on the sources in the catalogue). Alternatively, one can create a source model of one's choice, and calculate the likelihood that this model would have produced the observed arrival directions (see [16]).

2.3.2 Autocorrelation

If one has no specific source candidate in mind, calculating the auto-correlation of the arrival direction distribution can still give useful information about clustering, suggesting important source regions. To obtain the auto-correlation of an arrival direction distribution, the number of pairs of events with an angular separation smaller than a given value is compared with the number of pairs expected from an isotropic distribution. Absence of an excess of pairs at small angles suggests that there are many contributing sources and/or that there is a large angular separation between arrival directions from the same source (suggesting a heavy composition, far away sources and/or strong intervening magnetic fields) [16].

2.3.3 Dipole-anisotropies & higher multipoles

Prior to discussing dipole-anisotropies, we should briefly clarify some terminology. 'Galactic' does not mean 'in *a* galaxy', but 'in *our* galaxy'. In a similar vein, 'extragalactic' does not refer to 'objects outside *any* galaxy', but to 'objects outside *our* galaxy' which are almost always located 'in *another* galaxy'. When attempting to distinguish between galactic and extragalactic origins, the dipole-anisotropy of the arrival direction distribution forms the main signature of a Galactic origin. A dipole-anisotropy entails an excess of cosmic rays from one direction (the direction of the dipole) and a relative deficiency of cosmic rays from the opposite direction. There are several reasons why a (galactic) source distribution could result in a distribution of arrival directions exhibiting a dipole-anisotropy, see Figure 2.2. In this figure our galaxy is represented by a disc with a radius of 15 kpc (1 kpc $= 3.1 \cdot 10^{19}$m), which is negligibly thin (only a few hundred pc). The location of our Sun, $\odot$, is approximately 8.5 kpc from the centre of our galaxy (the blue cross). It could simply be the case that (a) the dipole-anisotropy results from a dipole in the source distribution, which is especially the case when only a few discrete sources are considered. However, even when (b) the source distribution is distributed symmetrically around our Sun, a dipole-pattern might show up due to the (de)magnifying effect of the (galactic) magnetic field upon the cosmic ray trajectories. The main cause of the 'Galactic dipole' that is usually referred to in the literature when one wants to distinguish between a galactic and extragalactic origin is (c) the dipole resulting from the offset of our Sun with respect to the centre of our Galaxy. At the high end of the diffusive regime, the galaxy is usually pictured as a 'leaky box'; although the cosmic rays propagate via a random walk, they can escape from the galaxy easier in the direction opposite to the galactic centre (from the perspective of our Sun) than in the direction of the galactic centre. This results in a dipole pointing towards the galactic centre. In the ballistic regime we will also obtain this dipole, simply because there are more galactic sources in the direction of the galactic centre than in the opposite direction. Thus, a dipole of type c (of course combined with the effects of the magnetic field (b) and possible fluctuations in the case of a low number of sources (a)) is a signature of a galactic source distribution. Nevertheless, we would also expect (d) a small dipole from an (isotropic) extragalactic source distribution, due to the movement of our Galaxy with respect to the frame of extragalactic isotropy, the so-called *Compton-Getting effect*. This dipole has been calculated to be only 0.6% [21], which is below the expectations for a galactic dipole.

The best way to calculate the dipole-anisotropy is through an expansion of the data in

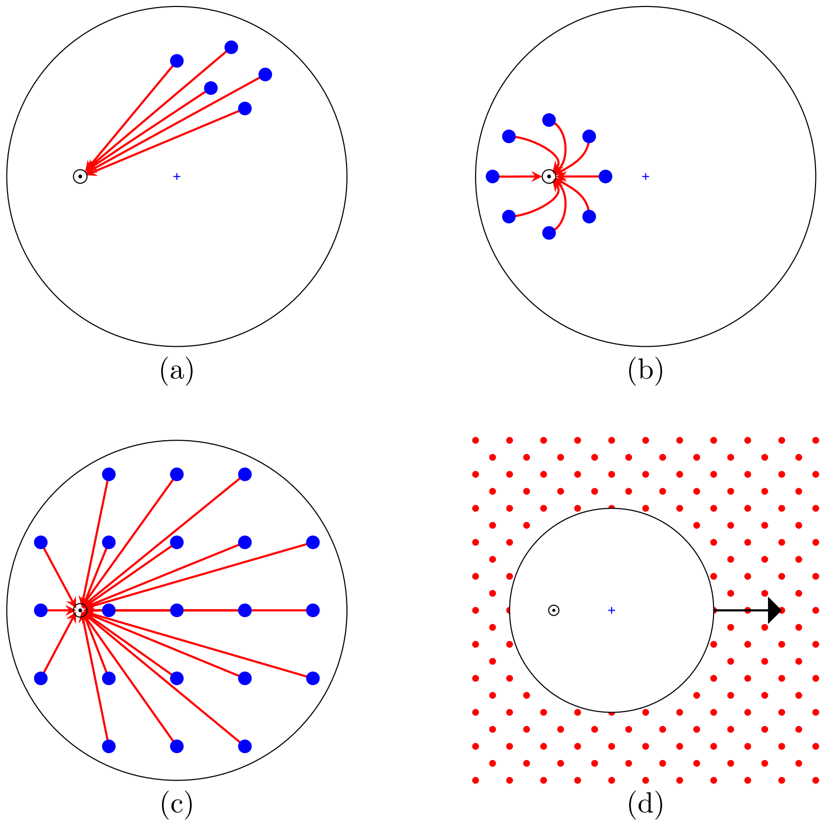

Figure 2.2: Four possible causes of a dipole-anisotropy in the cosmic ray arrival directions at Earth. See text for an explanation of the representation of our galaxy. Blue dots represent sources, whereas red dots represent (trajectories of) cosmic rays. A dipole-anisotropy can result from (a) a dipole-anisotropy in the source distribution, or (b) the (de)magnifying effects of the magnetic field (even if the source distribution itself is isotropic), or (c) the off-set of the Sun from the Galactic center or (d) the Compton-getting effect (see text). Combinations of these four causes are also possible.

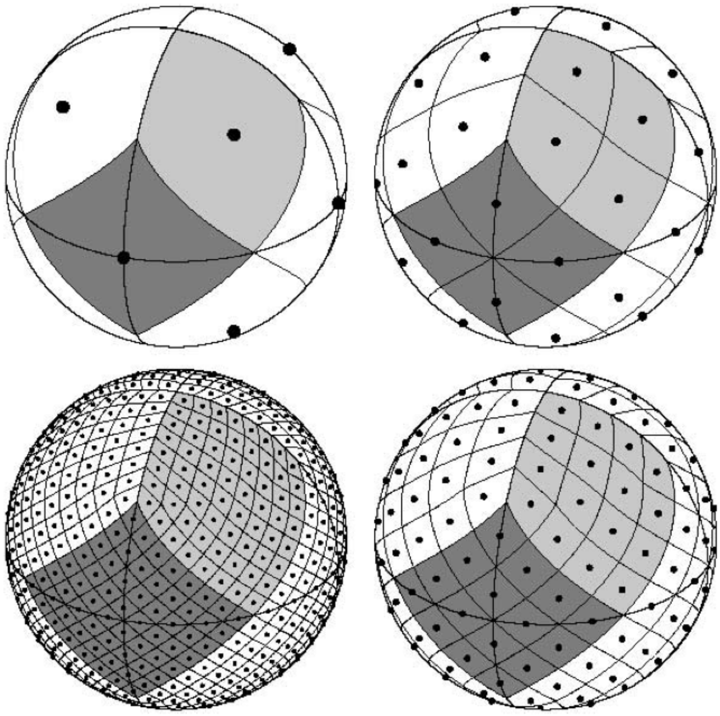

Figure 2.3: Orthographic view of the HEALPix partition of the sphere. The overplot of equator and meridians illustrates the octahedral symmetry of HEALPix. Light gray shading shows one of the 8 (4 north and 4 south) identical polar base-resolution pixels. Dark gray shading shows one of the 4 identical equatorial base-resolution pixels. Moving clockwise from the top left panel, the grid is hierarchically subdivided with the grid resolution parameter equal to $N_{side} = 1, 2, 4, 8$, and the corresponding total number of pixels equal to $N_{pix} = 12 \cdot N_{side}^2 = 12, 48, 192, 768$. All pixel centres are located on $N_{ring} = 4N_{side} - 1$ rings of constant latitude. Within each panel the areas of all pixels are identical. Reproduced by permission of the AAS, and courtesy of the authors of [23].

spherical harmonics. This method not only allows one to calculate the monopole and the dipole, but also higher order multipoles. As a matter of fact, we will see in Chapter 7 that at UHE higher multipoles become relatively more important (see also [22]). In order to calculate the spherical harmonics (efficiently), one needs a pixelisation of the surface of the sphere (i.e. the full sky) satisfying (1) equal areas per pixel, (2) iso-latitude distribution of the pixels on the spherical surface and (3) a hierarchical structure of the data base storing the pixels. These requirements are satisfied by the Hierarchical Equal Area isoLatitude Pixelization software (HEALPix[4] [23]). HEALPix divides the surface of the sphere into 12 equal-area base-resolution pixels (see Figure 2.3). Depending on the order chosen, the sides of these base-pixels are subdivided into $N_{side} = 2^{order}$ partitions,

[4] http://healpix.jpl.nasa.gov

giving a total number of pixels $N_{pix} = 12 \cdot N_{side}^2$ and allowing for a calculation of the spherical harmonics up to degree $l = 2 \cdot N_{side}$. The South Station and the future North Station of the PAO combined can observe the full-sky, enabling calculation of (upper bounds on) the higher multipoles, which can be compared with the theoretical calculations in this thesis. These theoretical multipoles are obtained using HEALPix version 2.20a.

An expansion in spherical harmonics, which is the two-dimensional analogue of a Fourier expansion, takes into account both coordinates that are used to describe arrival directions on the sky, such as longitude and latitude (i.e. galactic coordinates, used mainly in theoretical physics), or right-ascension and declination (used in experimental physics). However, if, for any part of the sky, the detector has zero exposure (such as the South Station of the PAO), it is not possible to expand the data in spherical harmonics [24], unless one would define new pseudo-spherical harmonics which are orthogonal when integrated over the regions of the sky that can be observed by the detector, or by using the Monte-Carlo techniques described in [25]. Under certain circumstances it is still possible to calculate the dipole by taking into account only one coordinate, although higher multipoles cannot be calculated anymore. If it is known, for instance from theory, that the dipole lies in the galactic (equatorial) plane (i.e. the plane defined by zero latitude (declination)), meaning that there is no out-of-the-plane component, then the dipole is equal to the amplitude of the first harmonic amplitude in Galactic longitude (right-ascension). This is the case in galactic coordinates for e.g. a dipole of type c (see Figure 2.2), which points towards the galactic center. The usual formulas of Fourier analysis apply: for a set of N arrival directions described by $\psi_1, \psi_2, ..., \psi_N$ (e.g. longitude or right-ascension) such that $0 \leq \psi_i \leq 2\pi$, the fractional first harmonic amplitude r and the phase ψ are defined through

$$r = (a^2 + b^2)^{\frac{1}{2}} \tag{2.1}$$

where

$$a = \frac{2}{N}\sum_{i=1}^{N} \cos\psi_i, \qquad b = \frac{2}{N}\sum_{i=1}^{N} \sin\psi_i, \tag{2.2}$$

and

$$\psi = \begin{cases} \psi' & \text{if } b > 0, a > 0 \\ \psi' + \pi & \text{if } a < 0 \\ \psi' + 2\pi & \text{if } b < 0, a > 0, \end{cases} \tag{2.3}$$

where

$$\psi' = \arctan\left(\frac{b}{a}\right), \qquad -\frac{\pi}{2} \leq \psi' \leq \frac{\pi}{2}. \tag{2.4}$$

In order to estimate the uncertainty in the fractional amplitude, one often assumes a normal distribution centred at r with standard deviation equal to $(\frac{2}{N})^{\frac{1}{2}}$. However, this approach is only valid if $N \gg \frac{4}{r^2}$ [26]; this condition is often not satisfied due to the low (global) statistics in the UHE regime (cq. the PAO has only detected 69

UHECR events). The correct method is described by Linsley [26] and gives the following differential probability distribution of the true amplitude s (written in terms of $\xi = s/r$):

$$p_\xi = \frac{2(\frac{k_0}{\pi})^{\frac{1}{2}}}{I_0(\frac{k_0}{2})} e^{-k_0(\xi^2+\frac{1}{2})} I_0(2k_0\xi), \tag{2.5}$$

where $k_0 = \frac{r^2N}{4}$ and I_0 is the zeroth order modified Bessel function of the first kind, i.e. $I_0(x) = I_0'(ix)$, where $I_0'(x)$ is the zeroth order Bessel function of the first kind. As can be seen in Figure 2.4, the distribution only approximates a normal distribution for

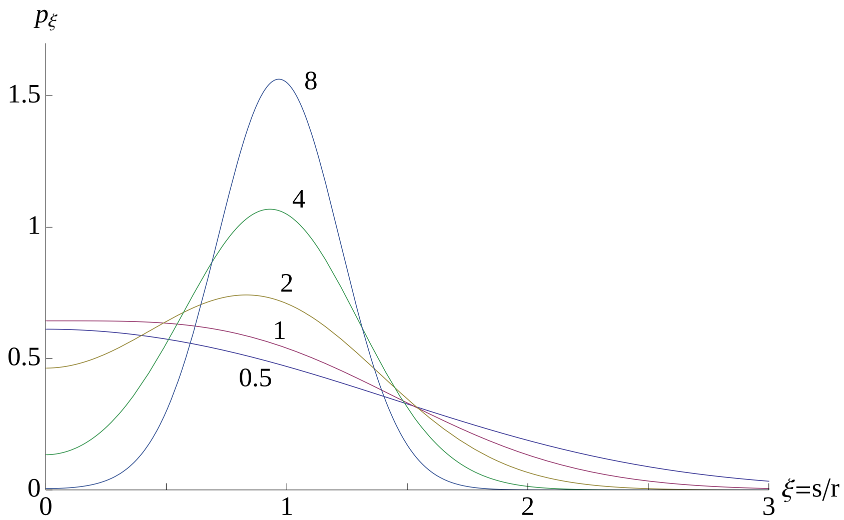

Figure 2.4: Differential probability distributions of $\xi = s/r$ labeled with the values of parameter $k_0 = \frac{r^2N}{4}$ [26].

$k_0 \gg 1$, while it is highly asymmetric for lower values of k_0. This requires the definition of asymmetric standard deviations σ_s^+ and σ_s^-. If one wants to define these for instance to correspond to a 90% confidence limit, it is tempting to define them in the following way:

$$\int_{\langle\xi\rangle}^{\langle\xi\rangle+\sigma_\xi^+} P(\xi)\mathrm{d}\xi = 0.45, \tag{2.6}$$

$$\int_{\langle\xi\rangle-\sigma_\xi^-}^{\langle\xi\rangle} P(\xi)\mathrm{d}\xi = 0.45, \tag{2.7}$$

where $\langle\xi\rangle$ is the expected value, which is equal to $[(\pi k_0)^{\frac{1}{2}} \cdot e^{\frac{-k_0}{2}} \cdot I_0(\frac{k_0}{2})]^{-1}$. This has been done by for instance [27]. However, these equations are ill-defined, since the distributions are asymmetric and hence $\int_0^{\langle\xi\rangle} P(\xi)\mathrm{d}\xi \neq 0.5$. Therefore, eqs. 2.6 and 2.7 do not always have a solution. Thus, in this thesis we define 5% and 95% confidence limits of ξ as follows:

$$\int_0^{\xi^-} P(\xi)\mathrm{d}\xi = 0.05, \tag{2.8}$$

and

$$\int_0^{\xi^+} P(\xi)\mathrm{d}\xi = 0.95; \tag{2.9}$$

such that we are 90% confident that the true value of ξ lies between ξ^- and ξ^+.

If it is known or assumed that the real dipole has an out-of-the-plane component that is *small* (e.g. the declination of the galactic centre in equatorial coordinates is $-29°$ instead of $0°$), it remains possible to use eqs. 2.1-2.4 to calculate the component of the dipole in the plane if one applies a corrective factor based upon $\langle \cos \delta \rangle$, where δ is the declination [21, Appendix]. Nevertheless, whenever possible, it is better to calculate the full dipole through an expansion in spherical harmonics over the complete sky, which takes into account both angles (e.g. longitude and latitude, or right-ascension and declination) and eliminates the need for premature assumptions about the direction of the dipole. The described method of calculating the uncertainty in the fractional dipole obtained through a Fourier expansion is equally valid for the dipole obtained from an expansion in spherical harmonics.

2.3.4 Patterns from individual sources

Cosmic rays emanating from the same source produce a recognisable pattern of arrival directions at Earth; the arrival directions of the highest energy cosmic rays point (almost) directly back towards the source, and are surrounded by a 'halo' of lower energy cosmic rays. The specific shape of this halo depends on the magnetic field configuration. An example of such a pattern from a source emitting cosmic rays isotropically has been plotted in a galactic skymap in Figure 2.5, using a Hammer-Aitoff projection and galactic coordinates, i.e. galactic longitude and latitude. A Galactic skymap should be understood in the following way. It represents the entire sky as seen from our Earth. The origin points towards the Galactic centre, and the rest of the horizontal axis (i.e. the line defined by zero latitude and $-180° \leq$ longitude $\leq 180°$ where longitude increases in the counterclockwise direction as seen from the galactic North Pole) defines the galactic plane, the well-known 'Milky Way'. The locations of the Galactic North and South pole are at $90°$ and $-90°$ latitude, respectively. With sufficient knowledge of these patterns (and the magnetic fields), one could in principle use them to track the origins of cosmic rays. Unfortunately it turns out that the statistical significance of this method is extremely difficult to determine; it is very hard to calculate the probability that a pattern is fake (i.e. cosmic rays from several sources mimicking the pattern from one individual source). Furthermore, real sources do not emit cosmic rays isotropically, but for instance in narrow jets. This distorts the patterns significantly. For these reasons this method has never been published, but it is most likely to be attributed to James Cronin, a Nobel laureate who co-initiated the Pierre Auger Project.

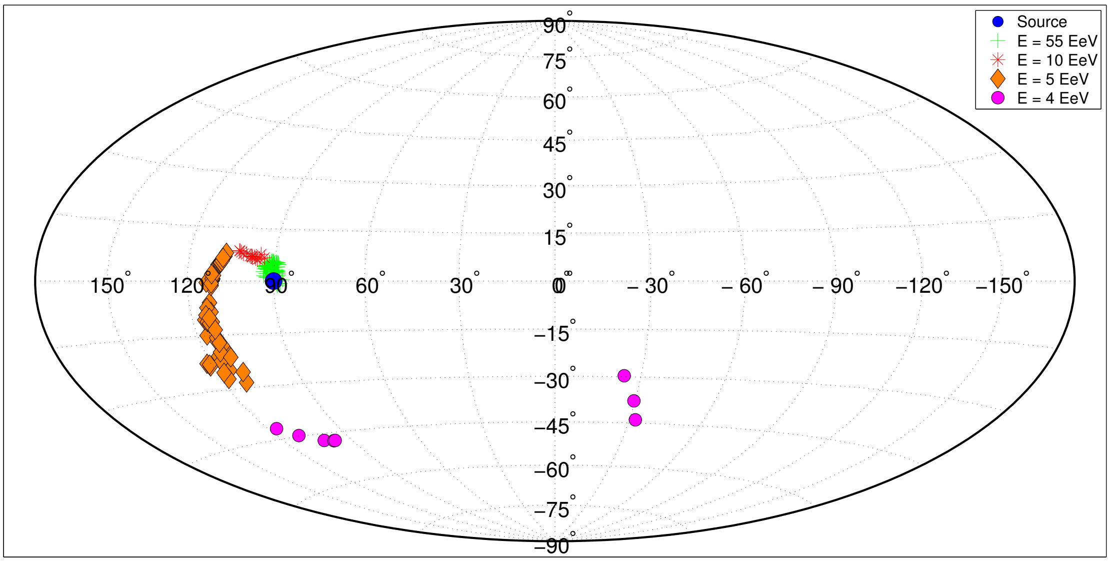

Figure 2.5: Galactic skymap of a pattern of arrival directions of cosmic rays with varying energies emanating from an individual source, plotted in galactic longitude (horizontal axis) and latitude (vertical axis). See text for an interpretation of galactic skymaps. This specific pattern was obtained with a point source at a distance of $8kpc$ in a *bss_s hmr* Galactic magnetic field (see http://crt.osu.edu/).

2.4 Current results

As mentioned before, the PAO has rejected the hypothesis of isotropy [15]. Further relevant recent results, mostly by the PAO, are listed below (see [14] for an overview of cosmic ray data).

2.4.1 Spectrum

See Figure 2.6 for the cosmic ray energy spectrum. Apart from the arc at low energies (which stems from the effects of the heliomagnetic and geomagnetic fields which prevent the cosmic rays from reaching the earth) the spectrum follows a power law ($\propto E^{-\alpha}$) with three kinks where the spectral index α changes [4, 5]. These kinks suggest e.g. source cut-offs, transitions from one dominant source type to another (e.g. a galactic-extragalactic transition) or a cut-off due to energy losses during propagation between the source and the Earth. Any theory for the origin of cosmic rays has to be able to explain these features in the spectrum. The spectral index α below the first kink, dubbed the Knee, is 2.7. At the Knee ($E_{\text{Knee}} \sim 10^{15} - 10^{16}$eV, flux $\sim$ 1 particle m^{-2} year^{-1}) the spectrum steepens and α increases to 3. At the second kink, dubbed the Ankle ($E_{\text{Ankle}} \sim 3 \cdot 10^{18}$eV, flux $\sim$ 1 particle km^{-2} year^{-1}), the spectrum flattens again to $\alpha = 2.69$. The cut-off at $E \sim 4 \cdot 10^{19}$eV (flux $\sim$ 1 particle km^{-2} century^{-1}) is usually called the GZK-cutoff, see Chapter 2.5. Besides the contribution of solar cosmic rays at

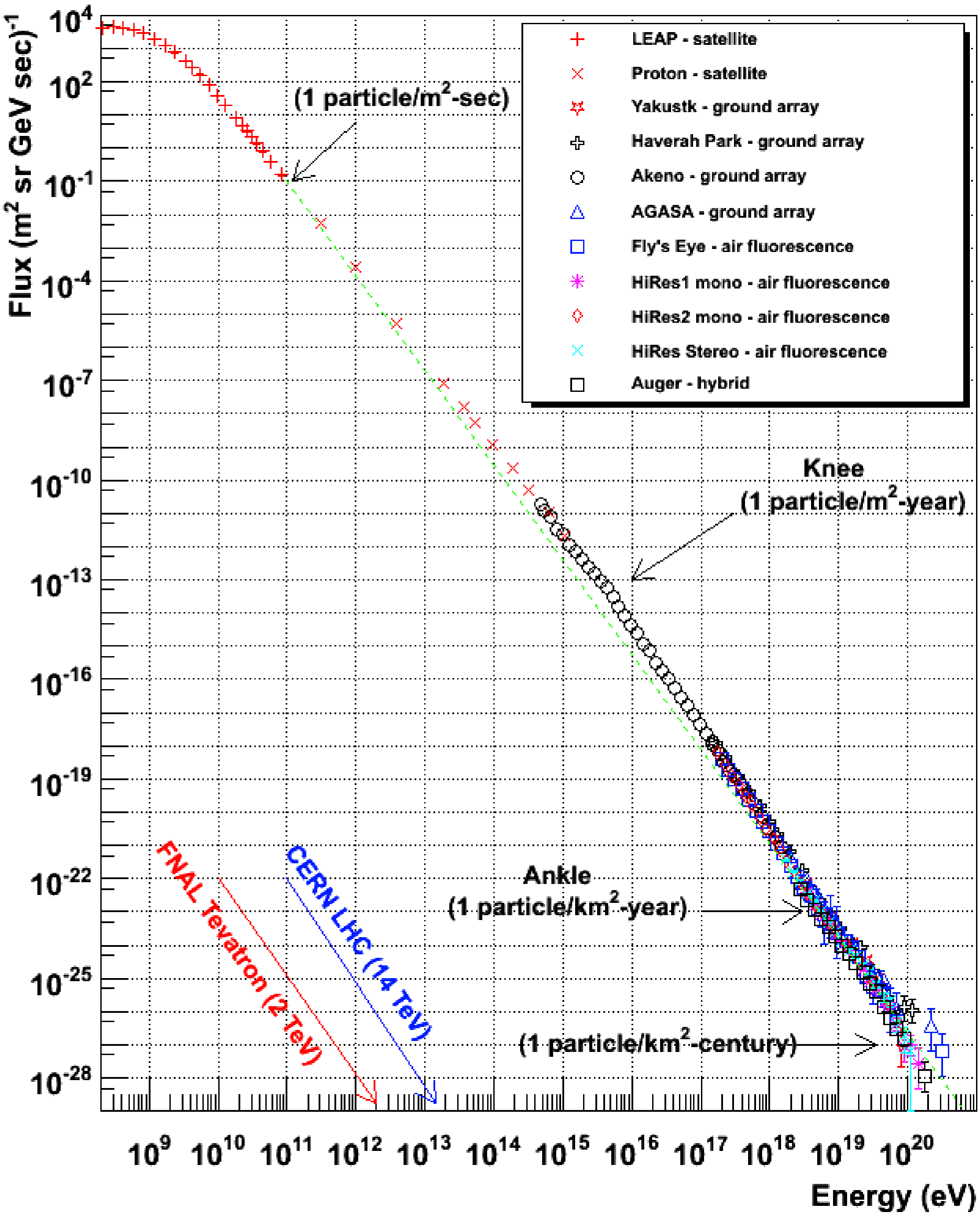

Figure 2.6: Cosmic ray energy spectrum from various experiments. Reproduced from http://www.physics.utah.edu/~whanlon/spectrum.html courtesy of W. Hanlon.

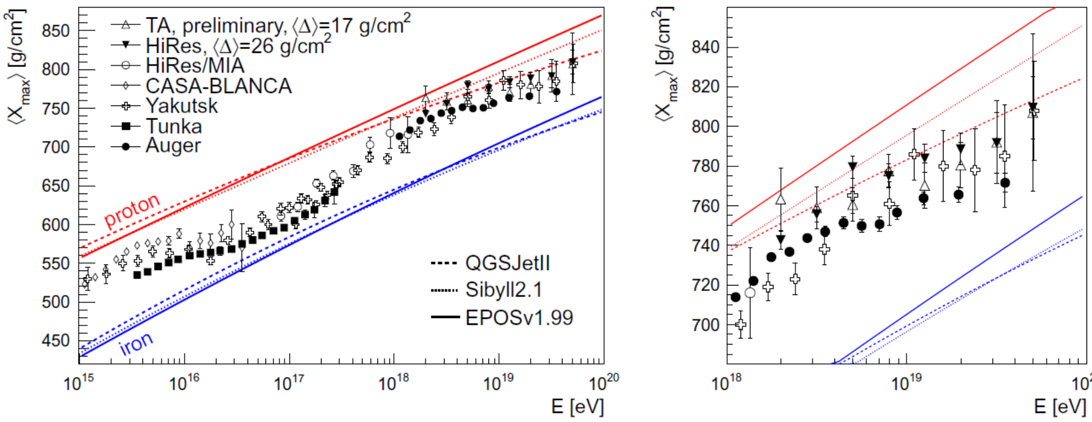

Figure 2.7: Measurements of $\langle X_{\max} \rangle$, the depth of the air shower when the maximum number of particles is reached, compared to air shower simulations with protons and iron nuclei as primary particles. The right panel shows a zoom to the ultrahigh energy region. Reproduced from [28] courtesy of K.-H. Kampert.

low energies, the main source type candidate for the production of low and intermediate energy cosmic rays is the supernova remnant (SNR), which accelerates particles through shock-front acceleration. SNR may be capable of accelerating protons up to either the Knee (and only heavier nuclei up to a higher energy, explaining the steepening of the spectrum) or perhaps even up to the Ankle. Above these energies it is unknown which sources produce the cosmic rays although it is often assumed that the Knee is a signature of the transition from galactic to extra-galactic sources, but see Chapter 2.5.

2.4.2 Composition

As mentioned in Chapter 2.1 the composition of cosmic rays at low and intermediate energies is dominated by protons. However, above the Knee the composition becomes heavier ([28], see Figure 2.7), consistent with a source cut-off (e.g. SNR which are able to accelerate protons up to the Knee, but only heavier nuclei beyond the Knee due to their higher charge), returning to a light composition at the Ankle. Surprisingly, recent measurements suggest that the composition becomes heavier again beyond the Ankle (although the error bars are admittedly quite large), contrary to the focus of UHECR research in the past decade on protons [29, 28]!

2.4.3 Arrival directions

Until now the PAO has detected 69 UHECR events [16]. The arrival directions are plotted in galactic coordinates in Figure 2.8.

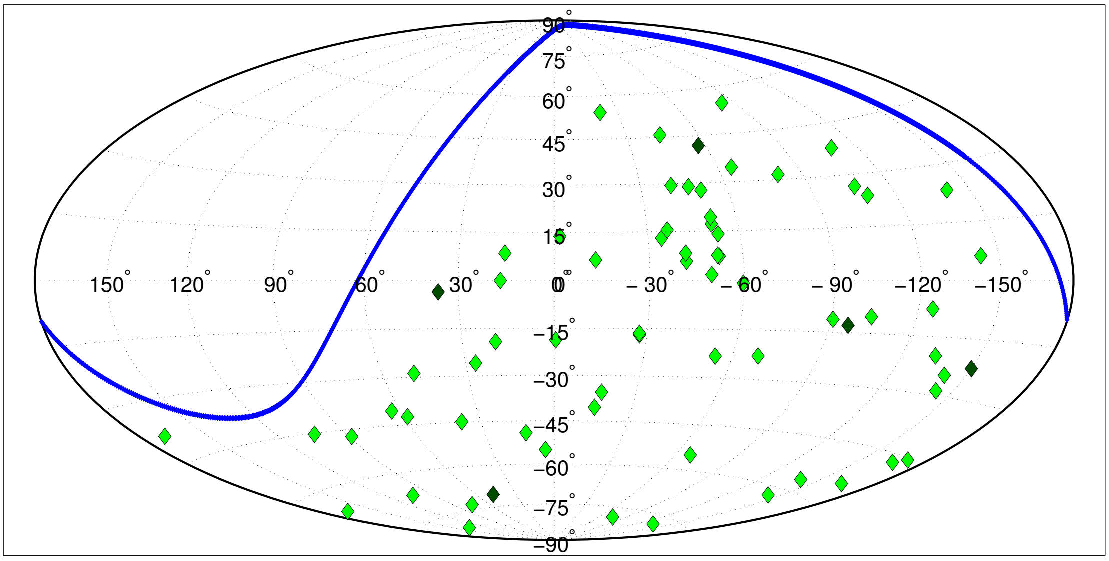

Figure 2.8: Galactic skymap of the 69 UHECR events detected by the South Station of the Pierre Auger Observatory [16], plotted in galactic coordinates (i.e. galactic longitude and latitude). The five most energetic events (ranging from 93 to 142 EeV) are coloured in dark green. The blue line represents the boundary of the exposure of the detector; only the region of the sky below the boundary can be observed by PAO. It should be realised that the exposure varies, i.e. it increases with the distance from the boundary, see [16].

2.4.4 Correlation

In 2007 the PAO collaboration claimed a correlation of $(69^{+11}_{-13})\%$ between UHECR arrival directions and nearby Active Galactic Nuclei (AGN), compared to an isotropic expectation of 21% [15, 20, 16]. Using their 2004-2006 initial dataset to optimise the correlation parameters they found a maximum angular separation $\psi = 3.1°$, consistent with proton cosmic rays. However, this is biased since the scan was only performed for $\psi \leq 8°$ because at that time a light composition was still assumed at UHE. As described in Chapter 2.4.2, the composition at these energies becomes heavier again; therefore we would only expect a true correlation at larger maximum angular distances. Indeed, the correlation of $(69^{+11}_{-13})\%$ obtained from the 2006-2007 dataset went down to only $(38^{+7}_{-6})\%$ when the 2007-2009 dataset was added [16]. Furthermore, none of the five events with the highest energies (the dark green diamonds in Figure 2.8) correlated with an AGN. Several authors have subsequently calculated correlations with different catalogues, but it is impossible to calculate the significance of these correlations because they are performed a posteriori and are therefore biased due to the lack of a blind protocol to optimise the correlation parameters from a separate new data set.

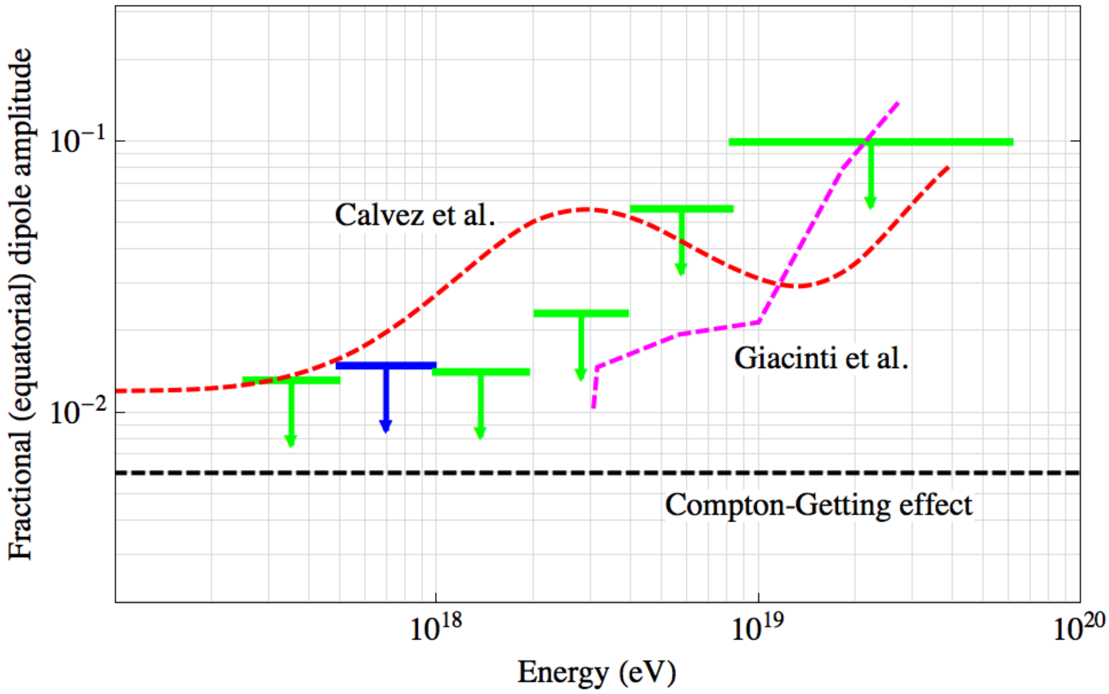

Figure 2.9: Upper limits (99% C.L.) on the fractional equatorial dipole amplitude, from the PAO (green, [21]) and AGASA (blue, [30]). Theoretical predictions of the fractional dipole by Calvez *et al.* [31] and Giacinti *et al.* [22] are also plotted. It should be noted that these represent the full dipole amplitude, and not only the equatorial component. Also shown is the dipole expected from the Compton-Getting effect.

2.4.5 Dipole upper bounds

The PAO has set upper bounds on the equatorial dipole amplitude of the distribution of arrival directions for $E \geq 2.5 \cdot 10^{17}$ eV, using the first harmonic modulation in right-ascension [21] (Figure 2.9). Celestial coordinates (i.e. right-ascension and declination) are analogous to galactic coordinates; right-ascension and declination assume the role of longitude and latitude respectively, the difference being that the plane defined by zero declination now defines the equatorial plane (i.e. the plane intersecting our Earth at the equator) rather than the galactic plane (zero latitude). Hence, the equatorial dipole amplitude is the component of the dipole in the equatorial plane. Two caveats should be made. Firstly, as mentioned in Chapter 2.3.3, a dipole pointing towards the Galactic centre does not lie in the equatorial plane, but is located at a declination of $-29°$. Although the PAO corrects for this fact when equating the equatorial amplitude to the first-harmonic modulation in right-ascencsion [21, Appendix], this means that the upper bound on the total dipole is less stringent than the upper bound on solely the equatorial component. A forteriori, although the phase of the dipole at energies below 1 EeV is compatible with the location of the galactic center, above 5 EeV the phase points in a radically different direction. Hence, there is no reason to assume that the dipole is anywhere near the equatorial plane. Due to this unrestricted possibility of a huge out-of-the-plane component, the equatorial upper bounds place no real restriction on the total dipole above 5 EeV [25]. Secondly, the highest energy bin used by the PAO is very wide; of the ~ 5000 events in this bin, only 69 events are UHECR. It is possible that these 69 events are characterised by a very large dipole-anisotropy, which is averaged out by binning them together with ~ 5000 events with a lower energy. Summarising, predictions of total dipole amplitudes (such as those by Calvez, Kusenko & Nagataki [31], by Giacinti *et al.* [22] and the predictions that will be made in this thesis) are consistent with the PAO results if they lie below the equatorial upper bounds; if they lie above the equatorial upper bounds it remains inconclusive whether the corresponding model is allowed (unless they are shown to lie in the equatorial plane in which case the model is ruled out). The mentioned predictions by Calvez, Kusenko & Nagataki and by Calvez *et al.* have already been plotted in Figure 2.9 to be compared to the PAO upper bounds, but will be discussed in Chapter 7 once the necessary terminology has been introduced. Finally, it should be noted that the 2011 upper bounds presented here are not yet sensitive to a dipole resulting from the Compton-Getting effect (Figure 2.2, type d), which is expected to be $\sim 0.6\%$. The current statistics are large enough to reach this scale and will be published soon.

2.5 Galactic or extragalactic origin?

As mentioned in Chapter 2.4.1, the Ankle is often assumed to signal the transition from galactic sources to extragalactic sources. Usually four reasons (which still assume the outdated light composition of UHECR) are mentioned why UHECR cannot be produced by sources in our Galaxy:

1. **A lack of plausible galactic source candidates**, i.e. a lack of candidates which fulfil the first three criteria mentioned in Chapter 2.1: (1) sufficient energy, (2) the Hillas criterium and (3) an adequate acceleration mechanism.

2. **The GZK cut-off**: Above an energy $E_{GZK} \sim 5 \cdot 10^{19}$ eV, cosmic ray particles interact with the Cosmic Microwave Background. They lose energy through pion photoproduction (for proton cosmic rays) or through nuclear photodisintegration (for heavier nuclei). Hence, cosmic rays reaching the Earth with energies above this threshold cannot have travelled for more than $\sim 100 - 200$ Mpc (depending on energy), the so-called GZK horizon (after Greisen, Zatsepin and Kuz'min [32, 33]). If the sources of cosmic rays are (partially) located beyond the GZK-horizon, one would expect a cut-off above the energy threshold in the spectrum observed at Earth, the so-called GZK cut-off. Since the cosmic ray energy spectrum indeed shows a cut-off around this energy (Figure 2.6), the origins of cosmic rays above the Ankle must be (partially) extragalactic.

3. **'A Milky Way of arrival directions'** would be expected from galactic UHECR (protons), since their trajectories are hardly influenced by the Galactic Magnetic

Field. However, the arrival directions reported by the PAO (Figure 2.8) are spread over the complete (observable) sky.

4. **A dipole-anisotropy** in the distribution of arrival directions would be expected from Galactic sources (Chapter 2.3.3), whereas the PAO has placed stringent upper bounds upon the dipoles (Chapter 2.4.5).

However, we have the following objections to these four arguments:

1. Mainstream Galactic source candidates indeed fail to satisfy the Hillas criterium for a proton composition. However, more possibilities show up for a heavier composition and by considering candidates that have received less attention in the literature until now (see Figure 2.1), such as specific types of γ-ray bursts [31] and magnetars. In this thesis we will focus on magnetars, although our results are valid for any galactic source satisfying the three criteria (energetics, Hillas & acceleration mechanism). In Chapter 3.2 we will show that magnetars may have sufficient energy available, and we will refer to work of others on magnetar acceleration mechanisms. Magnetars have actually been discussed as sources of UHECR before, but usually extragalactic populations are considered [34, 13, 35, 8]. However, we will show below that the cosmic ray emission from extragalactic magnetars (only two of which have been actually been observed yet) can be neglected compared to the dominating galactic population.

2. The GZK theory by itself simply implies that cosmic rays beyond the GZK energy threshold (i.e. UHECR) originate within the GZK horizon, which is consistent with a galactic origin. Now let us turn to the experimental facts. It might be the case that the observed cut-off is actually a source cut-off; protons can be accelerated maximally up to the cut-off energy, but heavier nuclei can be accelerated a bit beyond the cut-off due to their higher charge. This is consistent with measurements of a heavier composition at higher energies. On the one hand it might seem unlikely that such a source cut-off would occur at exactly the GZK energy. On the other hand, our main reason for investigating UHECR in the first place is that we are amazed by their extreme energies. Hence, we do not expect the spectrum to continue forever; we would expect a cut-off around the GZK energy scale anyway. Cut-offs similar to the observed cut-off can also be reproduced by adjusting the parameters of the acceleration mechanism [35, 8][5]. It has also been suggested that the cut-off could stem from protons leaking out of the galaxy, while heavier nuclei remain in the galaxy for much longer times [12]. In case the observed cut-off is indeed a GZK cut-off, this merely proves that cosmic rays between E_{Ankle} and E_{GZK} have an extragalactic component. Again, the cosmic rays above E_{GZK} ($\approx E_{\mathrm{UHECR}}$) must originate within the GZK horizon and therefore possibly in our own Galaxy.

[5] To be fair, [35] and [8] consider extragalactic (proto-)magnetars, but similar results might be obtained from galactic populations.

3. It is not *a priori* impossible for protons from galactic sources to obtain sufficient latitudinal spread as long as the total galactic magnetic field strength is sufficiently high ($\sim 5\mu G$), see Chapter 4.1. Moreover, in the light of the recent results suggesting a heavier composition, latitudinal spread becomes more likely. One of the main aims of this thesis is to make a quantitative statement about the possible latitudinal spread for protons and iron nuclei (Chapter 5). It will turn out that iron nuclei can actually be spread over the full sky.

4. As mentioned before, the equatorial upper bounds do not place a very strict limit upon the total dipole. Moreover, it will turn out that higher multipoles become relatively more important at UHE. Hence, it may be possible for galactic source models to stay below the limits set by the PAO.

As mentioned above, cosmic ray fluxes from extragalactic populations of sources which also appear in the galaxy, such as magnetars, can be neglected compared to the dominating galactic fluxes. This can be seen from the following coarse argument, in the style of Olber's paradox ([5]; P. Mertsch, personal communication, 2012). Let us assume for a moment that our observable universe is infinitely large, that there is a continuous distribution of cosmic ray sources and that energy losses are negligible. We can divide the universe into shells centred at the Earth, with radius r and thickness dr. The flux at Earth from a source in a shell is proportional to r^{-2}, but the number of sources per shell is proportional to r^2, so each shell contributes equally to the flux. An infinitely large universe contains an infinite numbers of shells, so we would expect an infinite flux. The continuity approximation is of course invalid; cosmic ray sources occur only in galaxies, and galaxies make up only a tiny percentage of the volume of the universe. If we would be located in a typical location in intergalactic space (i.e. the distance to the nearest galaxy being of the same order as the average distance between galaxies $L \sim$ Mpc, estimated by the distance between our Galaxy and the nearest spiral galaxy Andromeda), only the first few shells would give a small discrepancy compared to the continuous situation. We are however located in a most atypical position in our universe, we are sitting *inside* a Galaxy. The distance to the magnetars in our Galaxy $d \sim$ few kpc is many orders smaller than L. Therefore the flux from the magnetars in our own Galaxy is $(\frac{L}{d})^2 \sim 10^6$ times larger than the typical contribution from a shell of width L. Our galactic magnetars can outshine $\sim 10^6$ other shells of width L. Our actual observable galaxy is not infinitely large but ~ 10 Gpc, corresponding to only 10^4 shells. In fact, if we take into account energy losses (i.e. the GZK effect), our effective observable 'cosmic ray universe' shrinks to a size of $\sim 10^2$ Mpc corresponding to only 10^2 shells. Thus, the cosmic ray fluxes from extragalactic (proto-)magnetars that are considered by [34, 13, 35, 8] are actually negligible compared to their galactic counterparts. It should be noted that we have not taken into account the effect of the Galactic magnetic field. Further research should determine if the Galactic magnetic field for instance prevents Galactic cosmic rays from reaching the Earth and/or guides extragalactic cosmic rays toward the Earth.

Summarising, we have seen in this subsection that galactic sources cannot be ruled out *a priori* by the current measurements of arrival directions, dipole-anisotropies and the cut-off of the energy spectrum at the highest energies. We will need to perform detailed simulations to check if galactic source models for the production of UHECR can produce observables consistent with these measurements. This will be done in Chapter 5 and Chapter 6.

Chapter 3

Galactic candidate: magnetars

The specific galactic source candidate discussed in this thesis is the magnetar. We will first describe the features of a magnetar and subsequently give a rough estimation of the energetics involved.

3.1 What is a magnetar?

On March 5, 1979, several spacecraft detected an extremely intense pulse of gamma rays, 100 times as intense as any previous pulse of gamma rays detected from outside our solar system [36]. This was the first object discovered in a class that was soon to be dubbed Soft-Gamma Repeaters (SGR), the R stemming from the observation that the gamma pulse seemed to repeat itself (though with varying strengths and highly irregular periods), in contrast to the well-known gamma-ray bursts (GRB) which burst only once. Further characteristic properties of SGR are a five- to eight-second oscillation of the gamma ray signal (most probably due to a rotation of the source) and a steady X-ray emission. Its *extragalactic* source turned out to match the position of a supernova remnant in the Large Magellanic Cloud, a nearby galaxy. This implies an intrinsic luminosity of a million times the Eddington limit (i.e. the maximum luminosity of a stable star). These features imply an exotic source, such as a black hole or neutron star, which are indeed both believed to be associated with supernova remnants. Although the five- to eight-second modulation rules out a black hole, the identification of SGR with neutron stars faces its own problems; known neutron stars (radio pulsars) rotate with much shorter periods than the SGR & the power needed for the observed X-ray emission is too large to be provided by the rotation of a neutron star.

The first theory that correctly predicts all the observed features was put forward by Duncan & Thompson in 1992 [37] (see also [38]); the Magnetar Theory[1]. A 'magnetar' is a strongly magnetized neutron star. The 'residu' magnetic field ($\sim 10^{12}$ Gauss) of a 'normal' neutron star (a radio pulsar) stems from a failed attempt to produce a much

[1] Later it turned out that this theory explains Anomalous X-ray Pulsars (AXP) as well; AXP's are objects which characteristics very similar to SGR's (see for instance [36]).

stronger magnetic field through a phenomenon known as dynamo action. Dynamo action basically comes down to a transfer of convective and rotational kinetic energy into magnetic field energy. Only if the neutron star initially rotates fast enough (i.e. faster than the convective period of 10 milliseconds) the dynamo action is efficient enough to create a neutron star with magnetic field strengths up to $\sim 10^{17}$ Gauss, a magnetar. Such an object can account for the observed steady X-ray emission, SGR bursts and even the occasional giant flares, the necessary energy being provided by the magnetic field in contrast to normal neutron stars which power their radiation by converting rotational energy. The x-rays are explained by the friction of the moving material in the magnetar's interior (due to the magnetic field) which heats up the magnetar surface, and by the evolving exterior magnetic field. The magnetar remains active in this way for approximately 10,000 years. SGR bursts occur when the crust of the magnetar is unable to hold the unbearable magnetic forces, leading to strong dissipative currents above the magnetar, a 'starquake'. Occasionally the magnetic field becomes unstable on much larger scales, resulting in a giant flare that powers a 'fireball'. This 'fireball' is trapped by the exterior magnetic field, and evaporates in about three minutes while emitting hard X-ray/soft gamma photons. The extremely intense signal detected on the 5th of March 1979 is probably due to such a trapped 'fireball'. Furthermore, it should be noted that the 5th of March signal shows a four-peaked pattern, suggesting that the magnetic field near the magnetar is extremely complex.

The McGill SGR/AXP Online Catalog[2] [39] contains all observed magnetars (20) and magnetar candidates (3). Besides the 5th of March event, only one other extragalactic magnetar has been observed. The rest of the magnetars is located in the galactic disc. See Figure 3.1 for a galactic skymap of the observed magnetar distribution and for a map (containing only the 17 magnetars with an approximately known distance) viewed from the galactic North Pole. Our Galaxy might contain many more magnetars [40], especially in the region beyond the galactic centre which is difficult to observe.

3.2 Energetics

Arons is usually credited to be the first to have suggested magnetars as possible sources of UHECR in 2003 [41], but see Blanford's 2000 article [42]. As mentioned in Chapter 2.1, a source candidate for UHECR production needs to satisfy four requirements: (1) energetics, (2) the Hillas criterium, (3) an adequate acceleration mechanism and (4) a source distribution that can reproduce the observed arrival directions. In this subsection we give a very rough estimate of the energetics. This in no way proves that magnetars have sufficient energy available, but at least shows that they cannot be ruled out immediately. Magnetars have been shown to satisfy the Hillas criterium in Figure 2.1. The third condition lies outside of the scope of this thesis, but see [42, 40]. Quantising whether galactic magnetars satisfy the fourth criterium is one of the main aims of this thesis; this will be discussed in Chapter 6.1.

[2] http://www.physics.mcgill.ca/~pulsar/magnetar/main.html

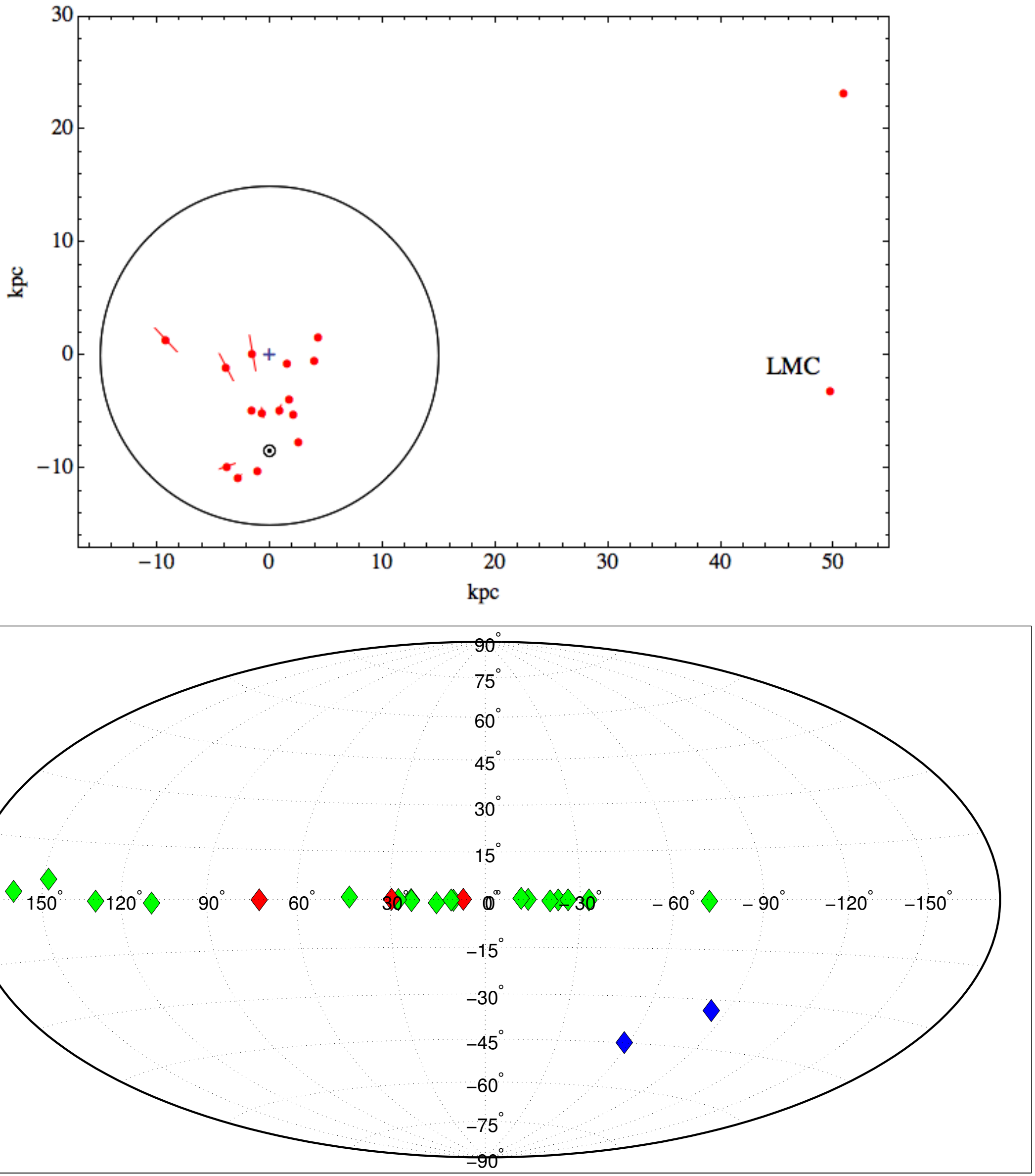

Figure 3.1: Distribution of observed magnetars and magnetar candidates. This data has been taken from the McGill SGR/AXP Online Catalog at http://www.physics.mcgill.ca/~pulsar/magnetar/main.html [39]. *Above:* Map of the 17 magnetars and magnetar candidates with approximately known distances. The red lines represent the uncertainty in the distance. One of the extragalactic magnetars is located in the Large Magellanic Cloud (LMC). *Below:* Galactic skymap of all 23 magnetars and magnetar candidates. Red diamonds represent unconfirmed (galactic) magnetars, green diamonds confirmed galactic magnetars and blue diamonds confirmed extragalactic magnetars.

We will first determine the (UHE) cosmic ray power requirement for our Galaxy and subsequently estimate how many galactic magnetars would be needed to supply this power. If we assume a galactic cosmic ray energy density of 1.80 eV/cm^{-3} [43] and furthermore take for the effective thickness of our Galactic disc 700 pc, for the radius 15 kpc [44] and for the average age of a cosmic ray particle in the galaxy $\tau = 3 \cdot 10^6$ years [5], we obtain a total cosmic ray power requirement for our Galaxy of

$$W_{Total,Gal} = \frac{\rho_{E,CR} \pi R^2 D}{\tau} = 4 \cdot 10^{34} J/s = 2.6 \cdot 10^{44} GeV/s. \tag{3.1}$$

This value represents the total energy in cosmic rays, due to all objects in the galaxy, whereas we are only interested in producing UHECR. If we approximate the cosmic ray energy spectrum in Figure 2.6 using values from [5, 14] and integrate the full spectrum, we find $\frac{W_{UHECR,Gal}}{W_{Total,Gal}} \sim 10^{-8}$ and hence $W_{UHECR} \sim 10^{36}$ Gev/s. As expected, UHECR form only a tiny fraction of the total cosmic ray energy.

To give a rough estimate of the energy content of magnetars we consider the following types of magnetar energy:

Rest mass energy The mass of a neutron star varies between 0.1 and 1 solar masses [44]. This corresponds to a rest mass energy of $\sim 10^{56} - 10^{57}$ GeV $\sim 10^{53} - 10^{54}$ erg.

Rotational energy Let us estimate the initial rotational kinetic energy of an extremely simplified model of a newborn magnetar. We take a radius $R \sim 10$ km and a mass $M \sim M_\odot$, where we ignore the neutron star crust and assume a uniform density, since the crust's density is negligible compared to the density of the inner part [45]. Furthermore we ignore differential rotation by assuming a uniform rotational period of $\tau \sim 1$ ms. These values give a moment of inertia $I = \frac{2MR^2}{5} = 8 \cdot 10^{37}$ kg $\cdot$ m^2 (which agrees with [46]). Since we are looking for an order of magnitude only, and the γ-factor is maximally 1.02, we need not worry about relativistic corrections (which will be maximally a few percent). Combining this information, we find an initial rotational energy of $E_r = \frac{1}{2} I \omega^2 \sim 1.4 \cdot 10^{45}$ J $\sim 10^{55}$ GeV. Kouveliotou *et al.* [36] estimate that $\sim$ 10% of this rotational energy is used to build up the magnetic field of the magnetar. However, it might be worth investigating whether the magnetic field is not instead due to the surrounding accretion disk [47].

Magnetic energy An alternative calculation of the magnetic field energy is given by

$$E_{mag} = \frac{B^2}{2\mu} \cdot V \sim 2 \cdot 10^{40} \left(\frac{B}{10^{15} G} \right)^2 \left(\frac{R}{10 km} \right)^3 J. \tag{3.2}$$

Energy in X-rays, bursts and giant flares The observed X-ray emission is $\sim 10^{35}$ erg s^{-1} [46]. Hence, a typical magnetar lifetime of $\sim 10^4$ years (i.e. the period during which the magnetar is actively emitting X-rays) gives a total energy dissipated through X-rays of $\sim 3 \cdot 10^{46}$ erg $= 3 \cdot 10^{39}$ J. The energy emitted in the optical and IR region can be neglected compared to this value [46]. The energy contained in SGR bursts is more difficult to calculate, due to the highly irregular time between bursts (i.e. the time between bursts varies over a range of 7 orders of magnitude) [48]. Taking SGR 1806-20 as an example (111 bursts have been observed from this SGR over a ten year period) we find as a typical value $\sim 10^5$ bursts during the lifetime of a magnetar. SGR bursts have a maximum peak luminosity of $\sim 10^{42}$ erg s^{-1} and durations $\sim 0.1 - 1$ s. Hence the total energy of one burst is $\sim 10^{41}$ erg and the total 'burst energy' during a magnetars lifetime is $\sim 10^{46}$ erg, similar to the energy associated with X-ray emission. However, the main part of the energy budget is spent on giant flares. After observing 5 magnetars for 30 years, only three giant flares have been observed, the largest of which contained an energy of $\sim 5 \cdot 10^{46}$ erg, which is two order of magnitudes higher than the other two [49]. This indicates a typical occurence of ~ 70 powerful giant flares in a magnetar lifetime, corresponding to a total of $\sim 4 \cdot 10^{48}$ erg $\sim 4 \cdot 10^{41}$ J $\sim 2 \cdot 10^{50}$ GeV. Thus, the radiation energy loss is mainly due to the powerful giant flares.

Gravitational radiation I have ignored gravitational radiation for the moment, but please see [50, 51, 52].

Assuming that the emitted radiation and cosmic rays are due to conversion of magnetic field energy, there is approximately $2 \cdot 10^{40} - 10^{44}$ J available per magnetar, whereas there is $\sim 4 \cdot 10^{41}$ J required for the powerful giant flares and a negligible amount for X-ray emission and for bursts . This leaves potentially no energy (for magnetar field strengths below $\sim 5 \cdot 10^{15}$ G) and maximally $\sim 10^{44}$ J for cosmic ray acceleration. Assuming the maximum energy, and an acceleration efficiency of a few %, we obtain for the cosmic ray power per magnetar (again using a typical lifetime of $\sim 10^4$ years):

$$W_{UHECR,mag} = 3 \cdot 10^{30} J/s \sim 3 \cdot 10^{40} GeV/s. \tag{3.3}$$

Concluding, whereas at the moment 18 confirmed galactic magnetars have been observed, one single magnetar seems sufficient to produce $\sim 10^4$ times the required UHECR density. Although a more detailed energy calculation is obviously necessary, there is at first sight no doubt that magnetars could satisfy the energy requirement for UHECR production.

Chapter 4

The Galactic Magnetic Field

Prior to describing the three models of our Galactic Magnetic Field that will be used for the simulations, we briefly review the behaviour of charged particles in a magnetic field.

4.1 Behaviour of charged particles in a magnetic field

The motion of charged ultrahigh-energy cosmic rays in the galactic magnetic field is governed by the relativistic Lorentz force. If the momentum is parallel to the magnetic field line, no work is done and the cosmic ray follows the field line. If the momentum is orthogonal to the field line, the result is circular motion in the plane orthogonal to the field line, with a radius

$$r_{\text{gyro}} = \frac{p_\perp}{Z \cdot B}, \tag{4.1}$$

which goes by the names Larmor radius, gyroradius or cyclotron radius, where r_{gyro} is in kpc, $p_\perp$ is in EeV/c and B is in μG. A particle with a momentum consisting of both a parallel and orthogonal component will spiral along the magnetic field line, as long as the magnetic field varies slowly on the scale set by the gyroradius. It can be shown [44] that, under this assumption, the particle's guiding centre motion follows the mean magnetic field direction, and the radius of curvature of its path is such that a constant magnetic flux is enclosed by its orbit, see Figure 4.1. Although this assumption is not always valid at UHE, this behaviour still forms a useful reference point when trying to understand the behaviour of cosmic rays in our Galactic Magnetic Field (GMF). At low energies, where the gyroradius is smaller than the coherence length of the turbulent component of the GMF ($\sim 0.1 - 0.3$ kpc [31]), the dynamics of cosmic rays is best approximated by a random walk. Therefore, this energy regime is named the diffusive regime. At UHE the gyroradius is larger than the coherence length of the turbulent component and so the cosmic rays will only 'see' the average field strength which is zero for the turbulent component. Hence, UHECR trajectories are determined by the regular component of the GMF.

We can make an educated guess of the (maximal) deflection of UHECR in the GMF by considering the following situation. The furthest possible galactic source is located

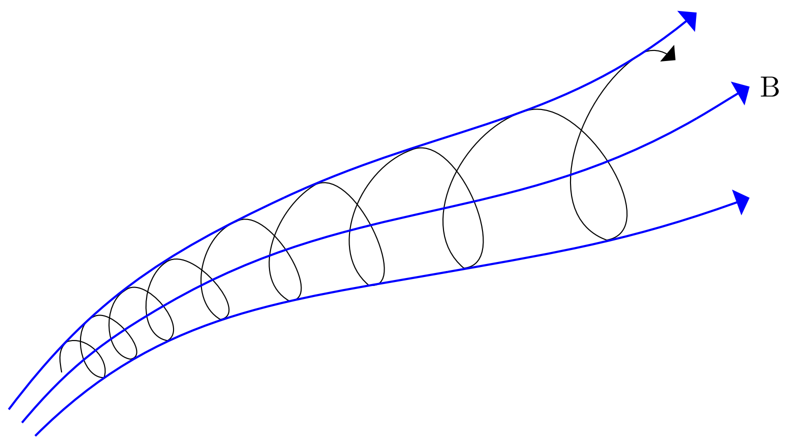

Figure 4.1: The trajectory of a charged particle in a slowly changing magnetic field. The particle's guiding centre motion follows the mean magnetic field direction, and the radius of curvature of its path is such that a constant magnetic flux is enclosed by its orbit [44].

23.5 kpc away from the Earth, assuming a distance between the Earth and the Galactic Centre of 8.5 kpc and a Galactic Radius of 15 kpc. The deflection of a cosmic ray which is emitted from that source and arrives at the Earth after having propagated through a uniform magnetic field orthogonal to the galactic plane is plotted in Figure 4.2 as a function of the magnetic field strength B, for both a proton and iron composition. This plot equivalently represents the maximum angular deflection possible for galactic sources in a GMF with a maximum field strength B_{max}. Several factors might lead to a smaller deflection than the maximal possible value:

- The GMF components (e.g. the disc field and the halo field) will probably not point in the same direction everywhere, reducing the total B.
- The GMF components will probably not reach their maximum value everywhere.
- The field will probably not always be orthogonal to the cosmic ray trajectory.
- We are mainly interested in latitudinal deflections (see Chapter 5), which are in general smaller than the total deflection.

We will see in the next subsection that the total GMF strength is $\lesssim 10$ μG. Hence, it is *a priori* not impossible for both protons and iron nuclei to reach all latitudes. Nevertheless, we expect the factors mentioned above to prevent protons from reaching the highest latitudes; iron nuclei are more likely to reach all latitudes. It will still prove useful to quantise how close we can get to the ideal case for protons, and contrast this with the results for iron nuclei.

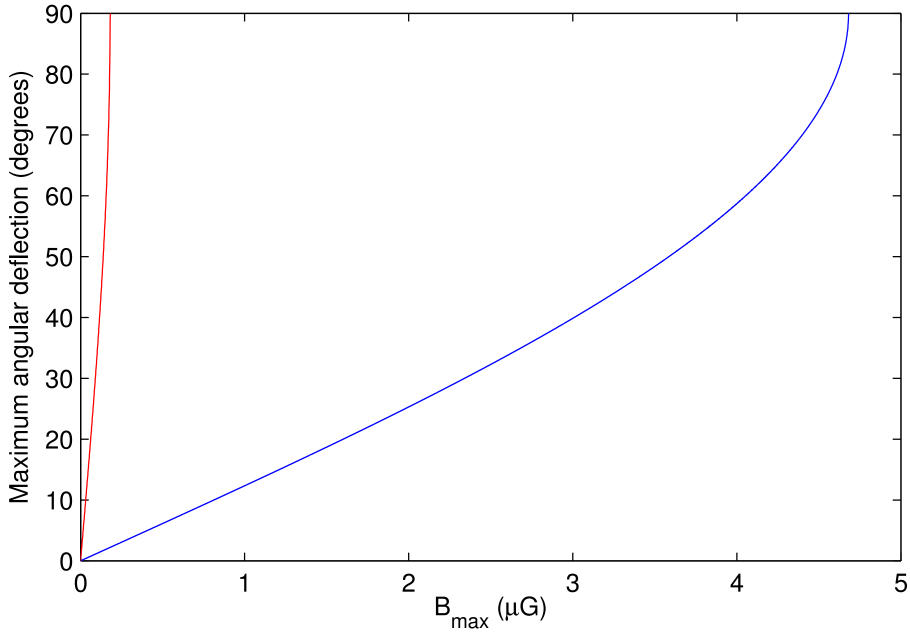

Figure 4.2: Angular deflections of proton (blue) and iron (red) cosmic rays from the furthest possible galactic source arriving at Earth after propagation through a uniform magnetic field orthogonal to the galactic plane with a field strength $B = B_{\max}$. This plot equivalently represents the maximum angular deflection possible from a galactic source for a GMF with a maximum strength $B_{\max}$.

4.2 Models of our galactic magnetic field

The main message of this section is that, despite the many claims about Galactic Magnetic Field (GMF) strengths and structures being made in the literature, there is hardly any consensus about the exact form of the GMF. That being said, a rough estimate of the field strength and knowledge of the different possible types of GMF components will already allow us to conclude a lot about the possibility of galactic sources producing UHECR.

GMF strengths vary from ~ 5 μG for radio faint galaxies like M 31 and M 33, to $\sim 20 - 30$ μG for the spiral arms of gas-rich spiral galaxies with high star-formation rates, like M 51, M 83 and NGC 6946, up to $\sim 50 - 100$ μG in starburst galaxies [53]. A typical total strength for spiral galaxies such as our own Galaxy is believed to be ~ 10 μG. In our own Galaxy this value might be reached in the centre, but the field strength is probably lower in other regions.

The GMF components in our Milky Way are usually categorised as either random/turbulent or regular field types, although a third type has recently been considered, which has been named the anisotropic [54, 53] or striated-random field type [3]. This latter type is regular on large scales, but reverses its direction by 180 degrees on smaller scales. We will ignore random fields in this thesis, since UHECR only 'see' the average of the random field, which is zero (see Chapter 4.1), and because random fields significantly increase computing time. See for example reference [22] for simulations including the random field type. Regular fields are further subdivided into disk fields (which form spiral patterns in almost every galaxy [54]), halo fields and an out-of-the-plane component. It is controversial whether an out-of-the-plane component indeeds exists. Mao *et al.* argue that there is no vertical magnetic field [55]. On the other hand, Nagar & Matulich [13], Takami [11] and Takami & Sato [9] do assume a vertical component. Furthermore, we will see that the third model of the GMF that we will use, by Jansson & Farrar [3], reproduces the observed Faraday rotation measures (see below) better if an X-shaped out-of-the-plane component is added, similar to the out-of-plane components we observe in many other galaxies, such as NGC 891 and NGC 253 [54, 53]. We will allow for the uncertainty in the existence of a vertical component by repeating all simulations with our first two models by Sun *et al.* [1, 2] (which do not contain vertical components) with an additional dipole field.

Models of the GMF are constrained by four key observables: Zeeman splitting (ZS) of radio spectral lines, linear polarisation data (PL) (mainly from synchrotron emission emanating from cosmic ray electrons spiralling around magnetic field lines, but also from optical, IR, submillimeter and radio data), Faraday rotation measures (RM) and the total intensity (I) of synchrotron emission [44, 54, 53, 3]. ZS mainly constrains the nearby GMF, while the other three observables constrain the magnetic field everywhere in our Galaxy. RM, PL and I all depend on the combination of the magnetic field and the (relativistic) electron density, which is usually modelled by the NE2001 electron distribution [56]. The RM (PL) is a line-integrated quantity and depends on the component of the field parallel (perpendicular) to the line-of-sight and the electron density. Regular fields contribute to RM, PL and I, whereas random fields contribute only to I. The striated field types contribute only to I and PI. The 2003 GMF model by Prouza and Šmída [57] has long been the model that best reproduces the observables. However, the recent increase of PM and PL data has lead to publications of many improved models, although it must be admitted that it is hard to determine whether these models are indeed better. There is however a strong suggestion that the magnetic structure of the Galactic disk is significantly different from that of the halo [58]. We will perform our simulations using (several versions of) two models by Sun *et al.* [1, 2] (see also [59] for a similar model) and one model by Jansson & Farrar [3]. These are the only 'composite' models in literature, that is the only models that consist of separate submodels for the halo and disk field.

4.2.1 Sun *et al.*'s GMF models: ASS+Ring & ASS+Arm

Sun *et al.* [1] proposed two GMF models in 2008 (and updated the strength of the Halo component in 2010 [2]), which are claimed to reproduce the Faraday Rotation Measure data better than any previous model. It must be admitted though that this comparison has been done by eye rather than quantitatively, and it is not specified how the values of the field parameters have been obtained. Both fields consist of a disk and halo component (and we will add a dipole field). Random and striated components are ignored. In both cases the disc field is an axi-symmetric spiral (ASS) field with no dependence on the azimuthal angle. We introduce cylindrical coordinates (R, ϕ, z), where R is the Galactocentric radius, ϕ the azimuthal angle starting from $long = 180°$ and increasing in the anti-clockwise direction as seen from the Galactic North Pole, and z is the distance to the Galactic plane. In these coordinates the disk field, which is set to zero for $R > 20$ kpc, is given by

$$\begin{aligned} B_r^D &= D_1(R,\phi,z)D_2(R,\phi,z)\sin p \\ B_\phi^D &= -D_1(R,\phi,z)D_2(R,\phi,z)\cos p \\ B_z^D &= 0 \end{aligned} \tag{4.2}$$

where $D_1(R, \phi, z)$ defines the spatial variation of the field strength and $D_2(R, \phi, z)$ adds reversals and/or asymmetries. The pitch angle p is the angle between the spiral magnetic field and the *clockwise* tangent to a Galactocentric circle, and is defined to be positive if it is directed outside that circle. For both models $p = -12°$. For both disk fields, $D_1(R, \phi, z)$ is parameterised by

$$D_1(R,z) = \begin{cases} B_0 \cdot \exp\left(-\frac{R-R_\odot}{R_0} - \frac{|z|}{z_0}\right) & R > R_c \\ B_c & R \leq R_c \end{cases} \tag{4.3}$$

where $R_\odot = 8.5$ kpc and the other variables depend on the model. The constant field strength B_c at the galactic centre represents the lack of sufficient RM data for that direction. The first model, the ASS+RING model, features reversals in rings. The parameters corresponding to $D_1(R, z)$ are $R_0 = 10$ kpc, $z_0 = 1$ kpc, $R_c = 5$ kpc, $B_0 = 2\mu G$ and $B_c = 2$ µG. The field reversals are symmetric in z:

$$D_2(R) = \begin{cases} +1 & R > R_1^R \\ -1 & R_2^R < R \leq R_1^R \\ +1 & R_3^R < R \leq R_2^R \\ -1 & R \leq R_3^R, \end{cases} \tag{4.4}$$

where $+1$ means a clockwise direction as seen from the Galactic North Pole, $R_1^R = 7.5$ kpc, $R_2^R = 6$ kpc and $R_3^R = 5$ kpc . The second model, the ASS+ARM model, features reversals following logarithmic spiral arms. The parameters corresponding to $D_1(R, z)$ are $R_0 = 8.5$ kpc, $z_0 = 1$ kpc, $R_c = 5.3$ kpc, $B_0 = 2$ µG and $B_c = 2$ µG. A logarithmic spiral arm edge is defined according to

$$\phi(R) = a \cdot \ln\left(\frac{R}{R_0^A}\right) + \phi_0^A \tag{4.5}$$

where $a = \frac{1}{\tan p^A}$, with p^A the pitch angle of the spiral arm, defined as the angle between the direction of the spiral arm (i.e. increasing ϕ) and the *anti-clockwise* tangent to a Galactocentric circle; the pitchangle is again defined to be positive if it is directed outside that circle. The ASS+ARM model features reversals in a single spiral arm, and in the region within R_c from the galactic centre. Hence, $D_2(R, \phi)$ is given by

$$D_2(R,\phi) = \begin{cases} -1 & R \le R_c \\ -1 & R > R_c \text{ and} \\ & \left[R^A_{0,inner} \cdot \exp\left(\frac{\phi' - \phi^A_{0,inner}}{a}\right)\right] < R < \left[R^A_{0,outer} \cdot \exp\left(\frac{\phi' - \phi^A_{0,outer}}{a}\right)\right] \\ & \text{for } \phi' = \phi + n \cdot 360°,\ n \in \mathbb{N}_0 \\ +1 & \text{otherwise} \end{cases} \tag{4.6}$$

where $p^A = 12°$, the inner edge of the spiral arm is located at the inner edge of the Scrutum-Crux spiral arm ($R^A_{0,inner} = 3.2$ kpc, $\phi^A_{0,inner} = 57°$) and the outer edge of the spiral arm is located at the inner edge of the Sagittarius-Carina arm ($R^A_{0,outer} = 3.5$ kpc, $\phi^A_{0,outer} = 0$). Both disk fields are plotted in Figure 4.3. Both models have the same

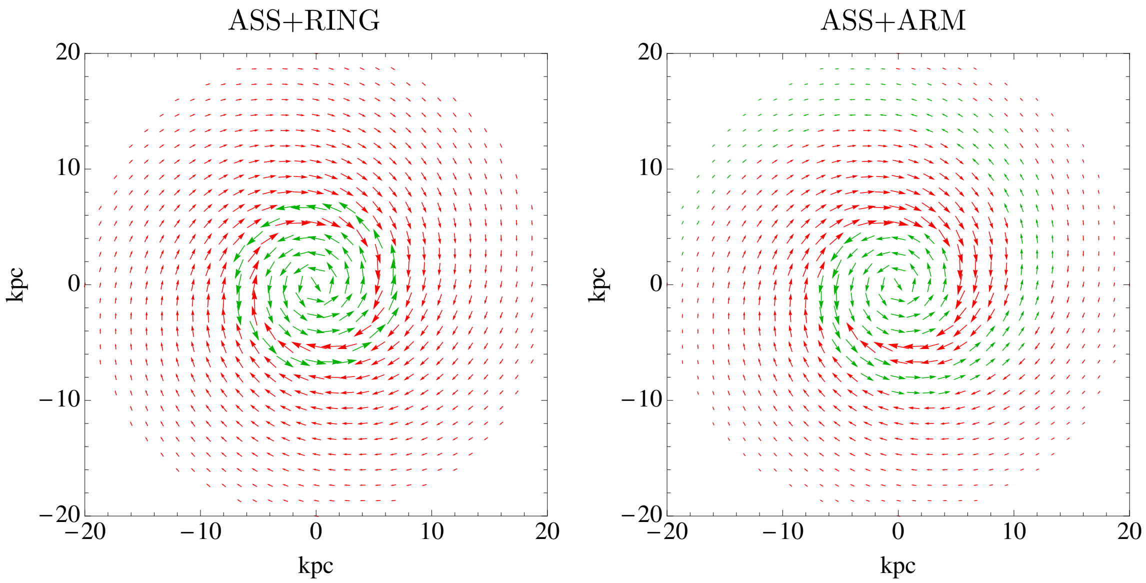

Figure 4.3: The disk components of the two Galactic magnetic field models by Sun *et al* [1] that produce the best fit with Faraday rotation measures and polarisation data.

halo component; a regular double-torus field component above the Galactic plane and the reversed direction below the Galactic plane:

$$B^H_\phi(R,z) = \frac{z}{|z|} \cdot B^H_0 \frac{1}{1 + \left(\frac{|z| - z^H_0}{z^H_1}\right)^2} \frac{R}{R^H_0} \exp\left(-\frac{R - R^H_0}{R^H_0}\right) \tag{4.7}$$

where $B_z^H = B_\phi^H = 0$, $z_0^H = 1.5$ kpc, $z_1^H = z_{1a}^H = 0.2$ kpc for $|z| < z_0^H$ and otherwise $z_1^H = z_{1b}^H = 0.4$ kpc, $B_0^H = 2\mu G$ [2] and $R_0^H = 4$ kpc. The strength of the Halo field above the Galactic plane is shown in Figure 4.4. Finally, as mentioned before, in order to

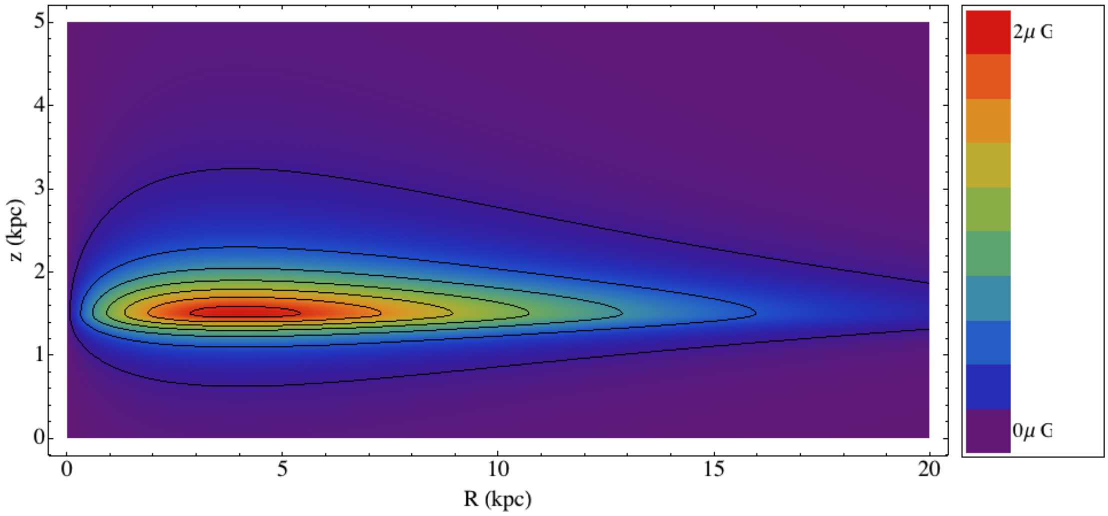

Figure 4.4: The strength of the regular halo magnetic field component of the GMF models by Sun *et al.* [1, 2] above the Galactic plane, as a function of the distance to the Galactic centre R and the distance to the Galactic plane z. Contours start at 0.1 µG and increase by 0.3 µG. The field below the plane has the same strength but is reversed.

take into account the uncertainty in the existence of a vertical component we will repeat all simulations with these two models by adding an out-of-the-plane component, in the hope that this helps getting the cosmic rays out of the Galactic plane. We use a simple dipole field pointing North at the location of the Sun with a strength of $5\mu G$ ($1\mu G$) for proton (iron) cosmic rays. Although a dipole component of 5 µG is unrealistically large, a dipole of 1 µG is insufficient to significantly deflect protons. A dipole component of 5 µG will make it easy to contrast the simulations with and without the dipole field.

4.2.2 Jansson & Farrar's GMF model

A new model of the GMF has been proposed very recently (April 2012) by Jansson & Farrar [3] (JF). Simulations with a large amount of new synchrotron emission data and Faraday rotation measure data show that this model seems to fit the data better than previous models. The model has been fitted to the data using 21 free parameters. We briefly describe the four components in the model (a striated component and an X-shaped out-of-the-plane component being the main difference with Sun *et al.*'s fields) and refer to [3] for the detailed functional forms and a list of optimal values for the 21 parameters and their uncertainties.

The JF model consists of a disk field, a halo field, an X-shaped out-of-the-plane component and a striated component (ignored in this thesis), all of which are made divergenceless explicitly. The disk field allows for 8 spiral arms (4 at the position of the spiral arms formed by population II stars, and 4 in between those arms). However, the best fit to the data suggests a significant field reversal for only one spiral arm (adjacent to the one in the ASS+ARM model) and weaker evidence for a second spiral arm. The typical strength of the disc field is slightly larger than in the first two models; the typical strength of the Halo field is slightly lower. The halo component is purely toroidal like our first two models, but features an exponential scale height and differs in strength and extent above and below the Galactic plane. The out-of-the-plane field is in the shape of an X, which is inspired by the observed magnetic field of other galaxies. This X-shaped field is easiest explained by referring to Figure 4.5. The field has no azimuthal component, nor does it depend on the azimuthal angle ϕ. The elevation angle (i.e. the angle between the field and the Galactic plane) is constant for $R > 4.8$ kpc and increases with decreasing R for $R \leq 4.8$ kpc until it becomes vertical at the Galactic Centre. The field decays exponentially in the z-direction. The striated component is everywhere aligned with the combined regular field.

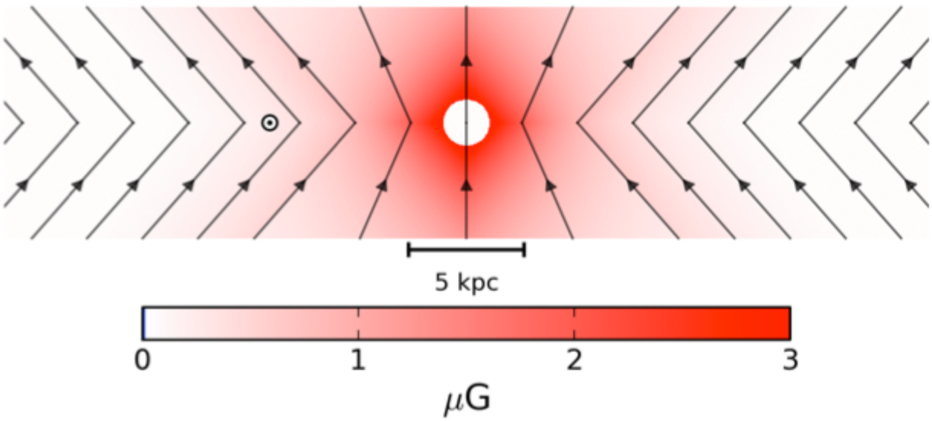

Figure 4.5: A slice of the Galaxy, intersecting the Sun and the Galactic centre perpendicular to the Galactic Plane, showing the X-shaped out-of-the-plane component of the JF Field. The black lines crossing the mid-plane at $R = 4.8$ kpc trace the boundary between the outer region with constant elevation angle, and the inner region with varying elevation angle. The black arrows show the direction of the field. Reproduced courtesy of R. Jansson and G. Farrar [3].

Chapter 5

Simulations I: Obtaining latitudinal spread for protons & iron nuclei

Prior to considering specific source distributions, we examine whether it is at all possible for cosmic rays emitted from Galactic sources to cover all regions of the sky as observed by the PAO. We want to get them out of the Galactic plane and create latitudinal spread. UHE cosmic ray trajectories are simulated with the publicly available source code CRT (see Appendix A), which offers two different methods: forwardtracking and backtracking. When opting for the former method, particles are injected at specified source positions and followed until they hit the Earth. Backtracking of a cosmic ray particle with charge q and arrival velocity $\vec{v}$ (at Earth) is accomplished by tracing the trajectory of the antiparticle with charge -q injected at the Earth with an initial velocity $-\vec{v}$. Under the assumption of negligible energy losses, this will trace the trajectory of the original particle back in time, which provides information on possible source locations. In this chapter both complementary methods, forwardtracking and backtracking, are used. In the former case, we perform a scan over all regions in the Galaxy and quantify the latitudinal spread using 'latitude envelopes'. In the latter case, we backtrack the arrival directions observed by the PAO and record the intersections of the tracks with the Galactic plane, in order to discover any possible forbidden regions, i.e. regions on the sky that cannot be populated with cosmic rays coming from the Galactic disk. For protons we expect that only low latitude regions lead back to the Galactic plane. For iron we expect that either all events connect to the Galactic plane, or the highest latitudes are forbidden.

5.1 Forwardtracking

In order to perform a scan over the Galaxy, we run simulations with sources distributed on Galactocentric circles with a radius R_{Gc} increasing in steps of 1 kpc up to 14 kpc.

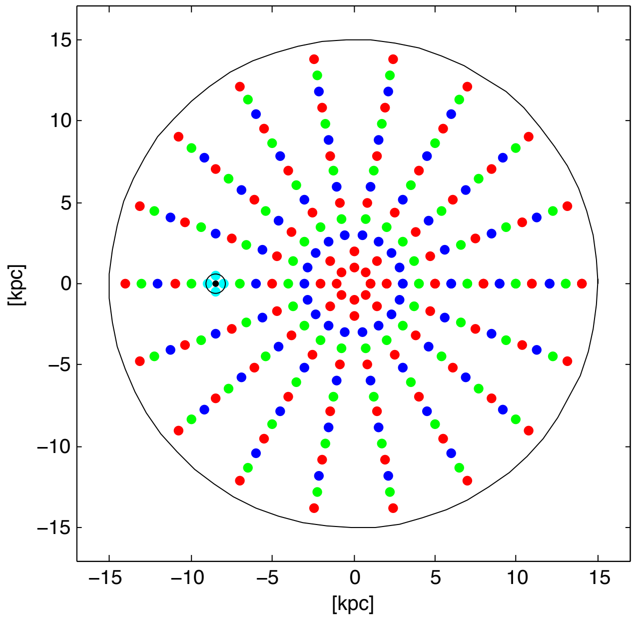

Figure 5.1: Source template used to perform a scan over the complete Galaxy. The sources are distributed on Galactocentric circles (red, green and dark blue) with a radius R_{Gc} increasing in steps of 1 kpc up to 14 kpc. The sources are located 20° apart, except for $R_{Gc} \leq 2$ kpc where they are 45° apart. The sources closest to the Sun in the Galactocentric circles with radii of 8 and 9 kpc are replaced by a Heliocentric circle (light blue) with a radius of 0.5 kpc containing 4 equidistant sources.

The sources are located 20° apart, except for $R_{Gc} \leq 2$ kpc where they are 45° apart, see Figure 5.1. This source template reflects the symmetries of the GMF and obtains its highest source density around the Galactic centre where the field strength is highest. The circles with Galactocentric radii of 8 and 9 kpc both contain one source at a distance of 0.5 kpc from the Sun, $\odot$. These sources touch the Earth when a detector radius of 0.5 kpc is used, and are hence replaced by a Heliocentric circle with a radius 0f 0.5 kpc containing 4 equidistant sources. Separate simulations with this Heliocentric circle are run using a detector radius of 0.1 kpc. All sources emit 1000 cosmic rays (see Appendix A for the remaining source parameters).

The arrival directions of simulated cosmic rays that hit the detector are binned in bins of 30° longitude. Within each bin, the two arrival directions with the maximum and minimum latitude are selected. A 'maximum latitude curve' is generated by connecting all the selected 'maximal latitude events'; a 'minimum latitude curve' is generated by connecting all the selected 'minimal latitude events'. The area between these curves forms a 'latitude envelope' and provides a measure of the latitudinal spread obtained. It should be realised though that, in general, the arrival directions within the latitude envelope are not homogeneously spread, see for instance the arrival directions for the ASS+ARM+Dipole model in Figure 5.2 to be compared with the latitude envelope in the upper right corner in Figure 5.5.

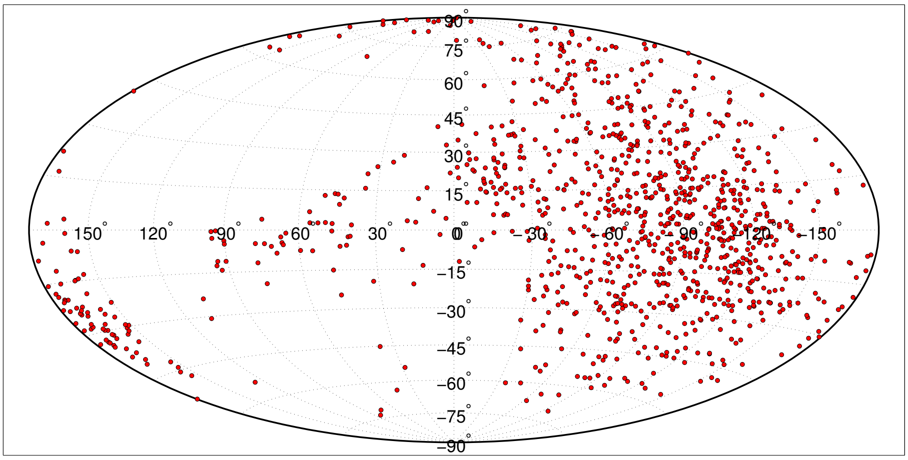

Figure 5.2: Arrival directions from all sources distributed on the Galactocentric circles in Figure 5.1, excluding the Heliocentric circle. The ASS+ARM+Dipole model has been used. This plot should be compared with the latitude envelope in the upper right corner in Figure 5.5 and forms an example of the inhomogeneous distribution within the envelope. In particular, almost no cosmic rays arrive in the upper-left quadrant.

Proton cosmic rays propagating through the regular versions of the three GMF models do not reach latitudes higher than 15° or lower than −15°, for any longitude (see Figure 5.4). The latitude envelopes enclose only a small proporation of the PAO arrival directions. Adding a dipole field increases the latitudinal spread to $\sim 40°$ degrees in both the positive and negative direction, but only for $30° \gtrsim long \gtrsim -100°$. The sources responsible for this effect are plotted in Figure 5.3. Only regions near the Galactic centre result in a large latitudinal spread, since the dipole field blows up in this region. Most sources lie below the Galactic centre (in Figure 5.3) because the dipole component points North (at the position of the Sun). The majority of the sources would lie above the Galactic centre if the dipole field component would point South. These results show that the clustering of the 12 events around $(long, lat) = (-45°, 20°)$, which are usually attributed to either the radiogalaxy Cen A $(-50.5°, 19.4°)$ or the Centaurus cluster $(-57.6°, 21.6°)$ [16], could be explained by galactic protons. However, even with the additional dipole fields, galactic protons cannot reach most of the regions of the sky covered by the PAO events, which falsifies the Galactic hypothesis for a proton composition!

The latitude envelopes for iron cosmic rays propagating through the three regular GMF models are significantly larger, see Figure 5.4. Still, the maximum latitudes are only $\sim 30° - 40°$. The minimum latitudes are as low as $\sim -60° - 80°$, but only in the direction opposite to the Galactic centre. The envelopes for the three regular GMF models still enclose only half of the PAO events, approximately. We expect that this stems from the halo fields not being sufficiently large and strong to bend all cosmic ray trajectories back towards the Galactic plane. To test this hypothesis we have repeated the simulations using the GMF models by Sun *et al.* with a stronger ($B_0^H = 3$ μG)

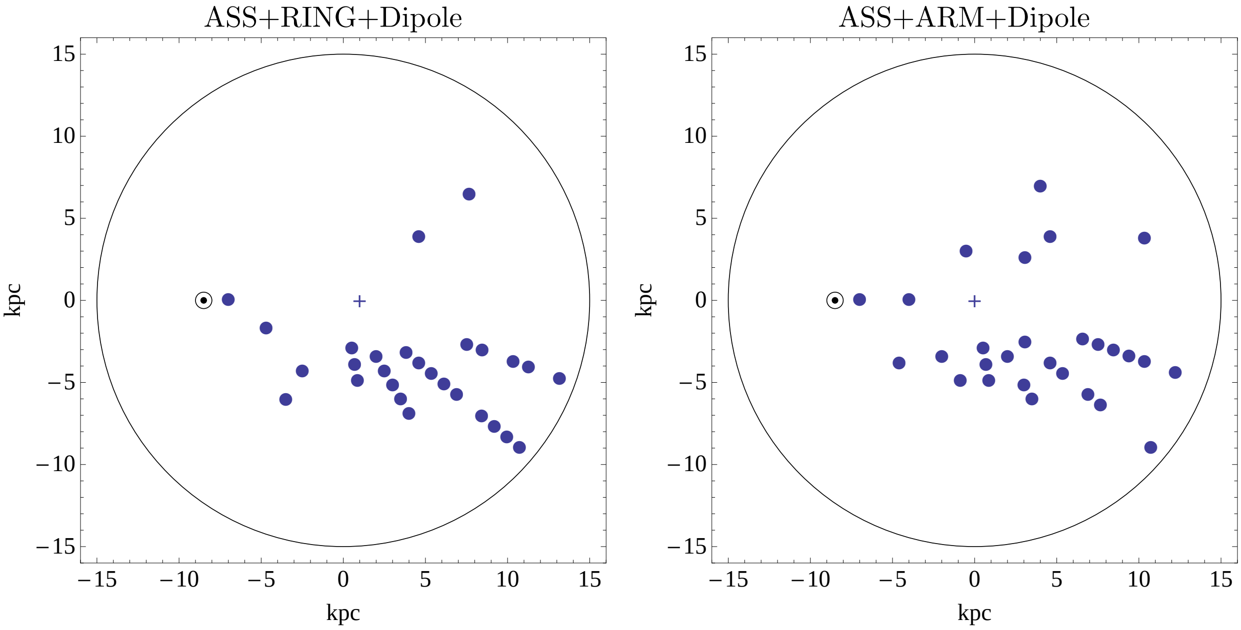

Figure 5.3: Proton sources that produce a latitudinal spread exceeding ±15° latitude, when an additional dipole field is used. It is expected that while with higher statistics more sources that contribute to high latitudinal spread would be found, the overall pattern would not change.

and larger (z_{1b}^{H} = 4kpc) halo[1]. This specific parameter choice will be justified in the next section. The corresponding latitude envelopes (Figure 5.5) enclose almost all the PAO events. The stronger and larger Halo field does succeed in deflecting most of the cosmic ray trajectories back to the Galactic plane. Latitude envelopes of similar sizes are obtained by adding a dipole field to the GMF models by Sun *et al.*. It should be noted that for these simulations, no hits were obtained from sources located within 2 kpc of the Galactic centre, at least not for the used number of emissions. This will be explained below. Concluding, even for an iron composition, Galactic sources are not capable of reproducing the complete set of arrival directions measured by the PAO, unless the GMF models by Sun *et al.* are modified by adding a dipole field or by enhancing the Halo component.

[1] For the sake of completeness, the simulations with protons have also been repeated with this modified halo field. Even with this modified halo, the latitudinal spread did not exceed 15°.

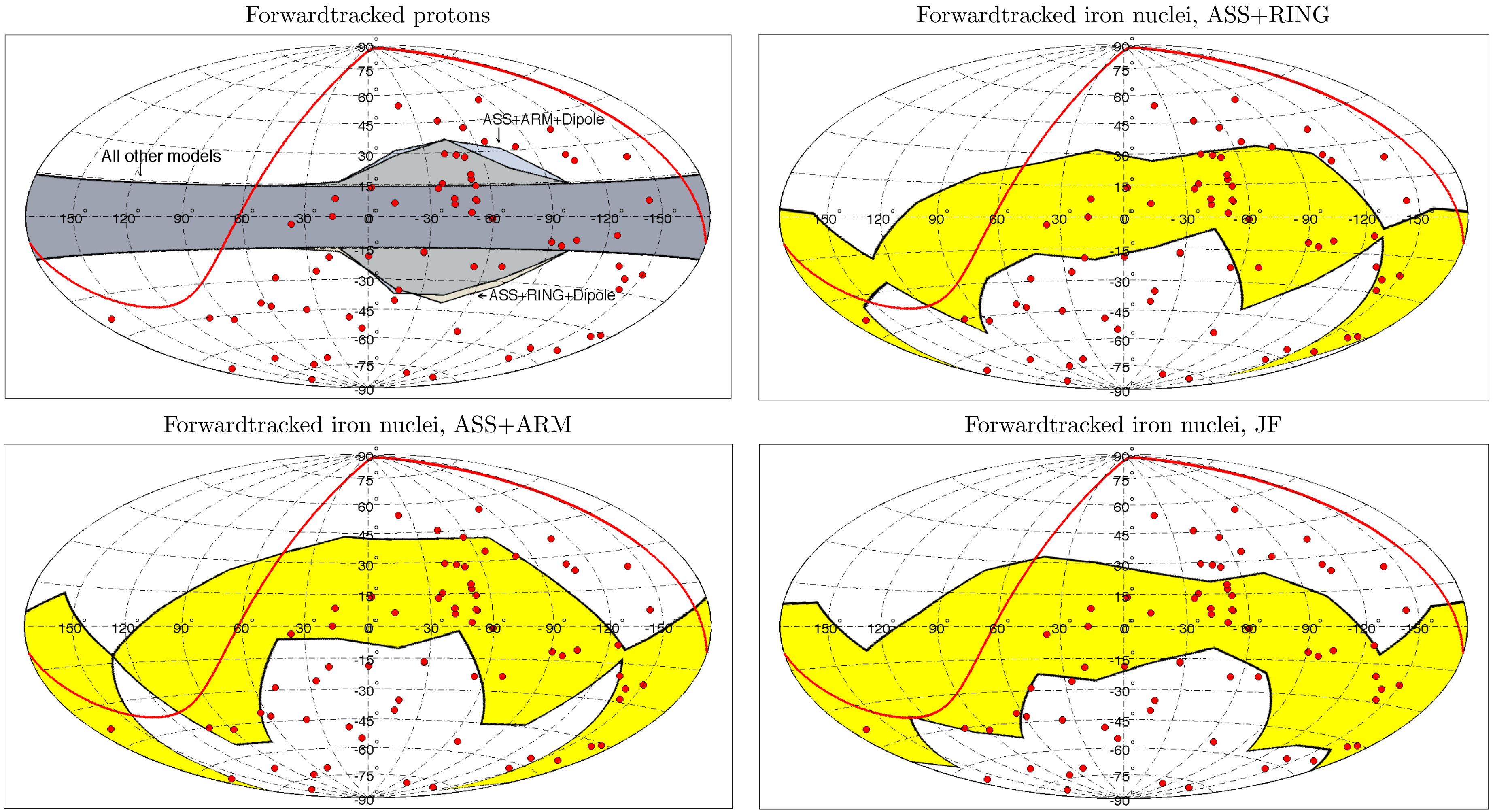

Figure 5.4: Latitude envelopes (see text) obtained from forwardtracking protons and iron nuclei from sources distributed as in Figure 5.1. The red dots represent the arrival directions observed by the PAO [16]. The red line represents the exposure boundary of the PAO.

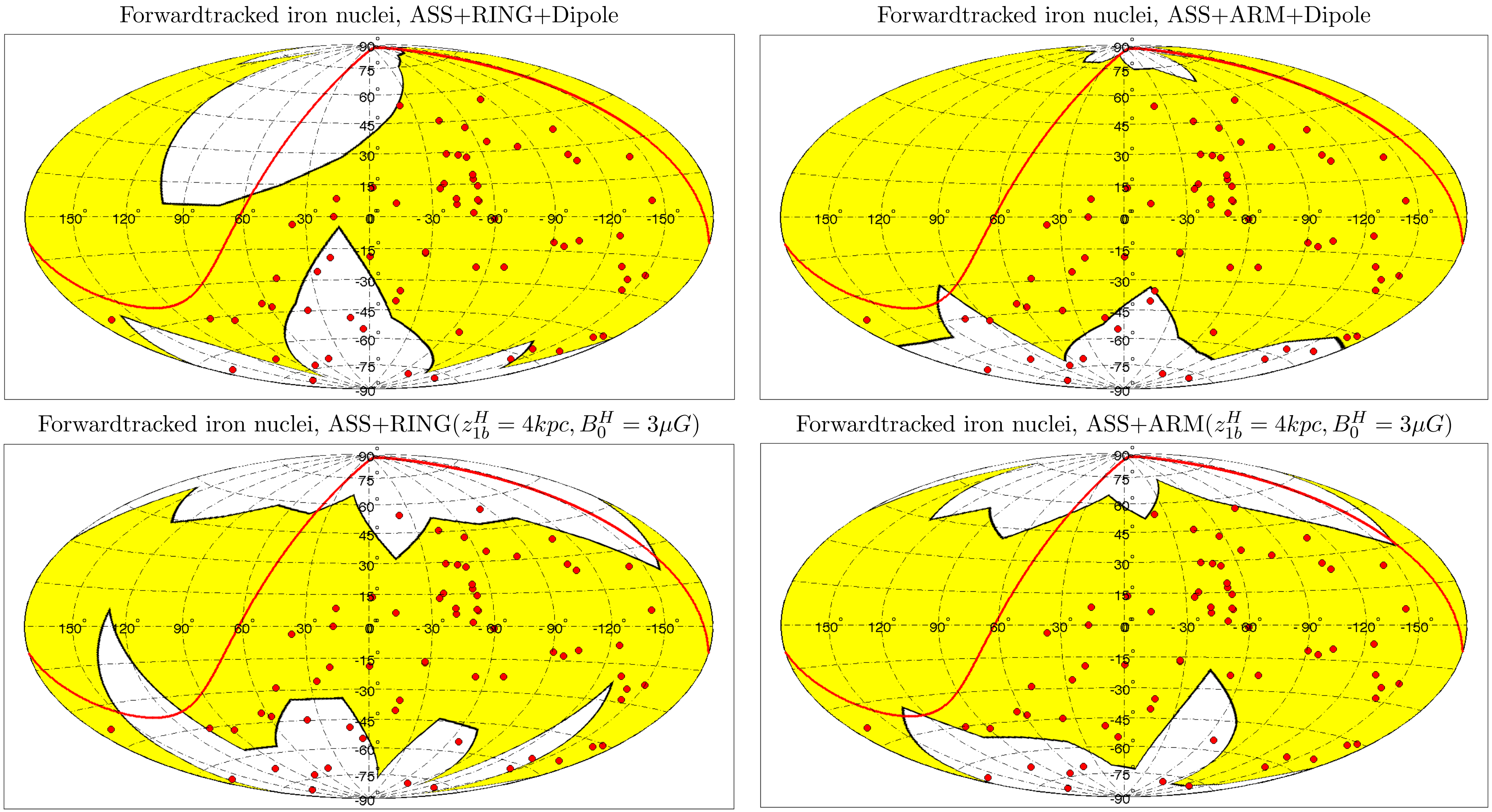

Figure 5.5: Latitude envelopes (see text) obtained from forwardtracking iron nuclei from sources distributed as in Figure 5.1. The red dots represent the arrival directions observed by the PAO [16]. The red line represents the exposure boundary of the PAO.

5.2 Backtracking

By forwardtracking cosmic rays, we have determined that modified versions of the GMF models by Sun *et al.* allow simulated iron nuclei emitted by sources in the Galactic plane to arrive at Earth from almost all latitudes. Would higher statistics cause the latitude envelopes to enclose the remaining few PAO events with latitudes near $\pm 90°$? Or are they completely disconnected from the Galactic plane? In order to answer this question definitively, we turn to the method of backtracking. We backtrack the 69 PAO events and count the number of trajectories that intersect with the galactic plane (defined as $|z| < 0.1$ kpc) at least once. Intersections within 1 kpc of the Sun are excluded. Intersections at $R_{Gc} > 15$ kpc are included.

Before presenting the results, we justify the modified Halo parameters used in the previous section. We have sampled some specific values of the magnetic field strength B_0^H, the radial scale length R_0^H and the second vertical scale height z_{1b}^H. The results, i.e. the number of backtracked trajectories that intersects the Galactic plane, are listed in Table 5.1. The first thing to notice is that the detailed structure of the disk fields (RING or ARM) hardly influences the results. Increasing R_0^H gives the smallest effect. The number of trajectories that intersect the Galactic plane is largest when z_{1b}^H is increased, contradictory to the results by [22]. Increasing z_{1b}^H corresponds to vertically stretching the part of the Halo field above $z = z_0^H = 1.5$ kpc. An even larger effect is obtained when a small increase in B_0^H is combined with a moderate increase in z_{1b}^H. The number of intersections obtained for $B_0^H = 3$ µG and $z_{1b}^H = 2$ kpc does not increase further by increasing z_{1b}^H even further. Nevertheless, we choose values of $B_0^H = 3$ µG and $z_{1b}^H = 4$ kpc for the modified Halo field used in this thesis, since this results in a slightly larger latitude envelope. The increase in these two parameters might seem unreasonably large, compared to their original values ($B_0^H = 2$ µG, $z_{1b}^H = 0.4$ kpc). However, one should keep in mind that the Halo model used to have a field strength of 10 µG in 2008 [1]. Furthermore, all GMF models depend significantly on a poorly constrained model of the Galactic electron distribution. We have seen in Chapter 4.2 that even larger field strengths are quite common in other galaxies. Most importantly, the Halo parameters chosen by Sun *et al.* have not been justified; they have not been compared to different values. In contrast, Jansson *et al.* [58] scan over the full parameter space using a Markov Chain Monte Carlo algorithm (with additional data), in order to optimize the model and parameter choice. Of all the popular models they consider, the models by Sun *et al.* produce one of the best-fits with rotation measure and polarisatin data, but for completely different parameter values. The values they obtain are $B_0^H = 4.9 \pm 0.7$ µG, $R_0^H = 18 \pm 4$ kpc and $z_{1b}^H = 8.5 \pm 1.5$ kpc. They furthermore mention that the constraints on the vertical scale heights are extremely weak, allowing even for scale heights of an order of magnitude larger than our value.

The intersections of the backtracked PAO events with the Galactic plane are plotted in Figure 5.6 (protons) and Figure 5.7 (iron nuclei). The corresponding numbers of backtracked events that intersect with the Galactic plane are listed in Table 5.2. As expected, the proton cosmic rays are hardly deflected by the GMF, except for the models

modified Halo parameters	ASS+RING	ASS+ARM
regular ($B_0^H = 2\mu G, z_{1b}^H = 0.4kpc, R_0^H = 4kpc$)	37	35
$R_0^H = 15kpc$	45	42
$B_0^H = 5\mu G$	55	57
$z_{1b}^H = 8kpc$	62	65
$z_{1b}^H = 1kpc, B_0^H = 3\mu G$	58	59
$z_{1b}^H = 2kpc, B_0^H = 3\mu G$	65	65
$z_{1b}^H = 4kpc, B_0^H = 3\mu G$	65	66
$z_{1b}^H = 8kpc, B_0^H = 3\mu G$	65	66

Table 5.1: Number of backtracked PAO events (69 in total [16]) that intersect with the Galactic plane, for iron cosmic rays propagating through the ASS+RING and ASS+ARM models with modified Halo parameters. Intersections within 1 kpc from the Sun are excluded. Intersections at a Galactocentric radius larger than 15 kpc are included.

GMF model		protons	iron nuclei
ASS+RING	regular	6	37
	+dipole	14	61
	$z_{1b}^H = 4kpc, B_0^H = 3\mu G$	7	65
ASS+ARM	regular	6	35
	+dipole	13	60
	$z_{1b}^H = 4kpc, B_0^H = 3\mu G$	7	66
JF		5	41

Table 5.2: Number of backtracked PAO events (69 in total [16]) that intersect with the Galactic plane. Intersections within 1 kpc from the Sun are excluded. Intersections at a Galactocentric radius larger than 15 kpc are included.

with an added dipole field. Hence, only a small proportion of the backtracked trajectories (i.e. those injected at small latitudes) intersects with the Galactic plane, even for the models with an added dipole field. Those trajectories are approximately parallel to the Galactic plane and form almost straight lines (or slightly curved lines when a dipole field is added) in Figure 5.6. These results are consistent with the results obtained from forwardtracking: Galactic protons cannot reproduce the full set of PAO arrival directions. For an iron composition, we observe that there are no trajectories connecting the Earth and the inner part of the Galaxy when a dipole field is added. This is consistent with the absence of hits from cosmic rays emanating from sources in the innermost region of the Galaxy, as has previously been observed with the forwardtracked simulations. In this region the dipole field, which is proportional to $1/r^3$, blows up; this suggests that iron nuclei emitted in this region either circulate forever or are ejected from the Galaxy along the Galactic poles. In the former case, the Galactic centre would function as a reservoir of cosmic rays, which would result in synchrotron radiation observable at Earth. Consistent with the forwardtracking results, only half (approximately) of the backtracked PAO trajectories connects with the Galactic plane, when the three regular GMF models are used. For the models by Sun *et al.* with either an additional dipole field, or with modified Halo parameters, almost all the PAO events connect to the Galactic plane. More interestingly, although the two PAO events with the most positive latitude are forbidden (i.e. they do not connect with the Galactic plane when backtracked) for the three regular GMF models, they are allowed for the GMF models with an additional dipole field or with modified Halo parameters. All the events with the most negative latitude are allowed for the fields with modified Halo parameters, and only some of those events are forbidden for the remaining GMF models. Concluding, it seems that, contrary to hypothesis, the forbidden regions are not around the Galactic poles. The exact forbidden regions will be discussed in Chapter 6.2.

Finally, it should be noted that a minority of the trajectories (not shown) suggests that cosmic rays can hit the Earth even if they are emitted in the opposite direction (i.e. with a beam angle larger than 90°), see for instance the loop just beneath the Galactic centre in Figure 5.6 (ASS+RING+Dipole).

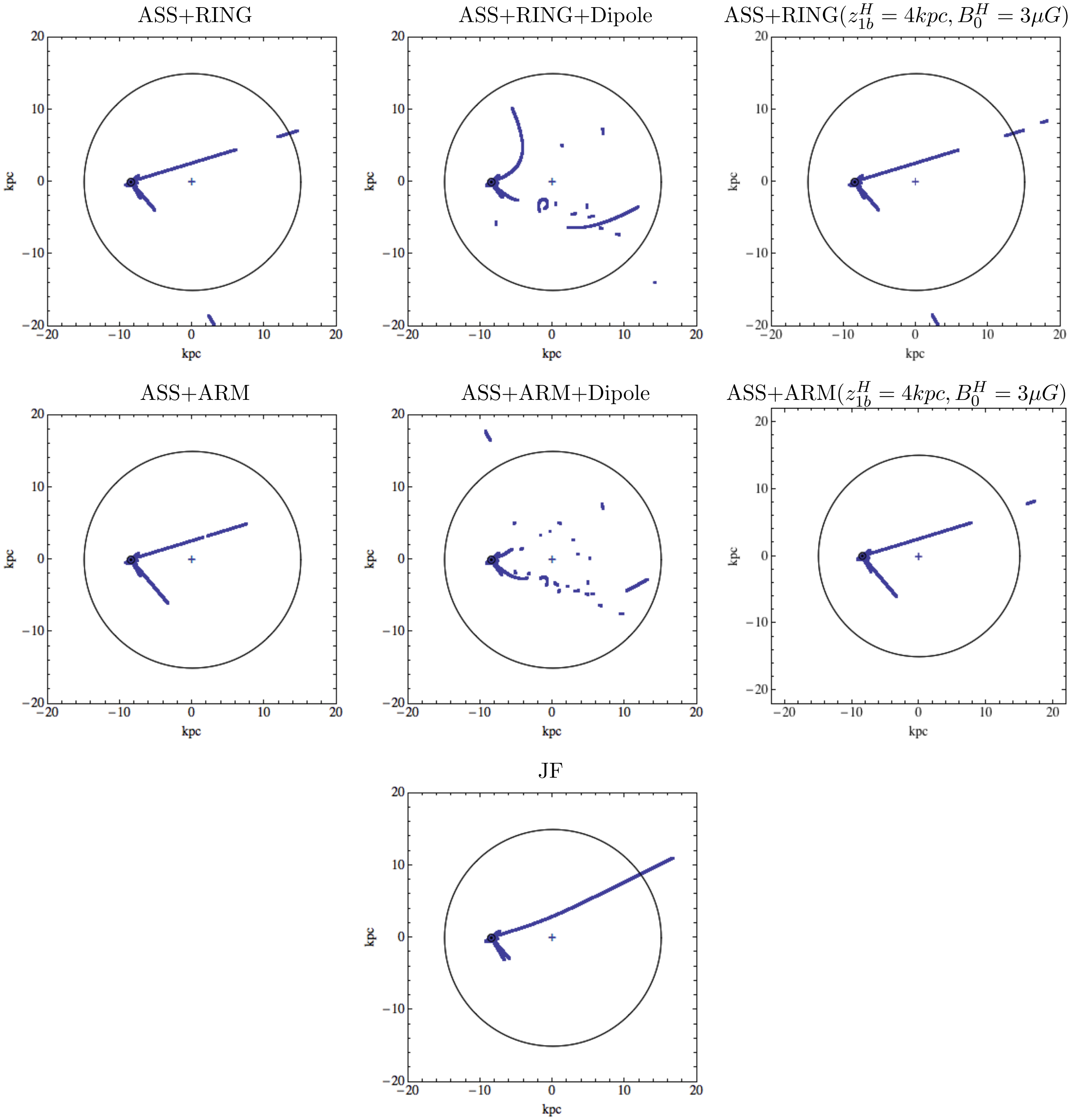

Figure 5.6: The intersections of the trajectories obtained from backtracking the 69 PAO events with the Galactic plane, assuming a proton composition.

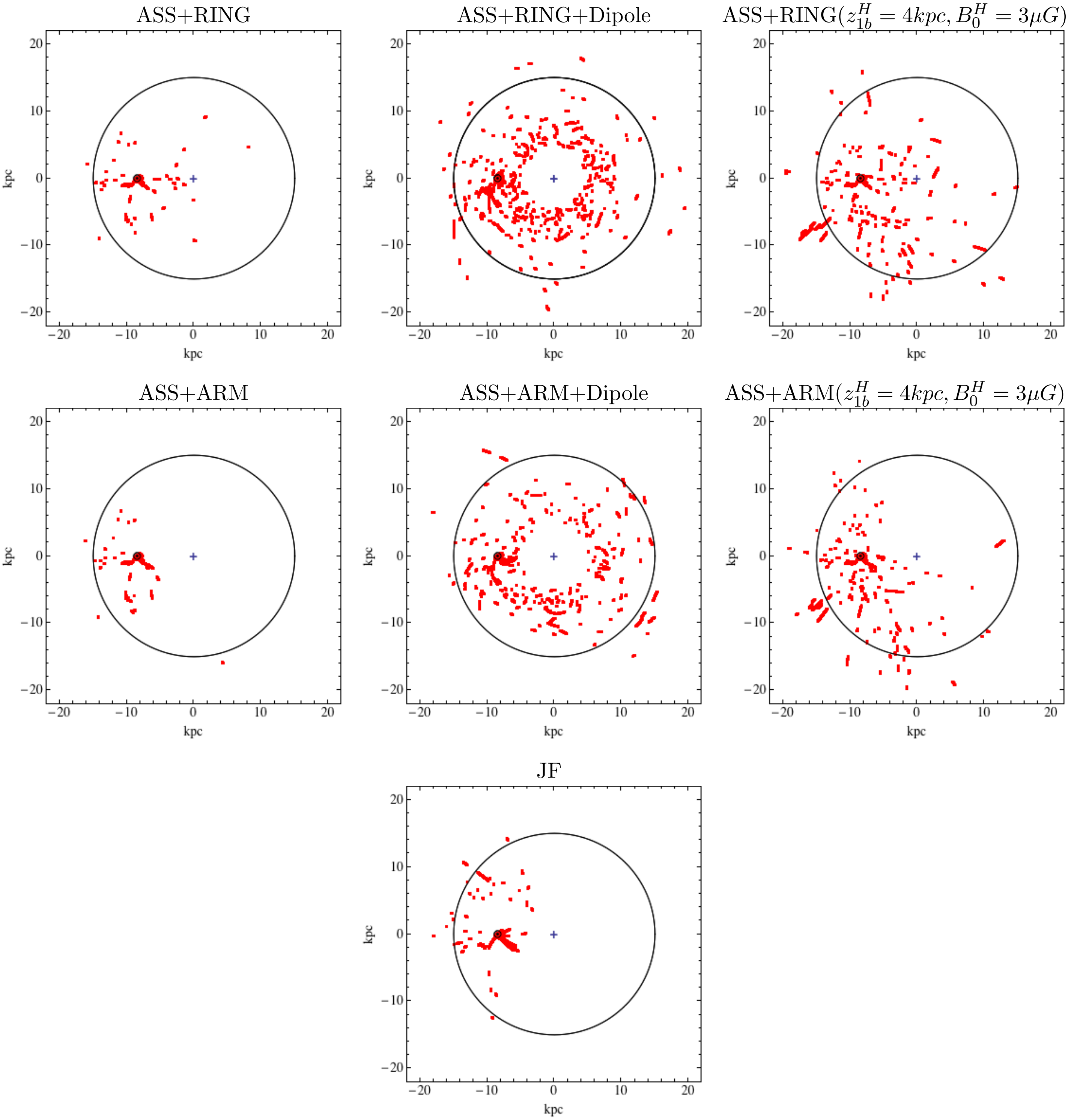

Figure 5.7: The intersections of the trajectories obtained from backtracking the 69 PAO events with the Galactic plane, assuming an iron composition.

5.3 Conclusions

- Both the forwardtracking and backtracking method rule out the possibility of Galactic protons producing the full set of arrival directions as observed by the PAO. This applies to all GMF models considered, although an additional dipole field allows protons to cover the clustering region usually attributed to Cen A or the Centaurus cluster.

- Both the forwardtracking and backtracking method confirm that only half of the PAO events can be reproduced with a iron composition, if the three regular GMF models are used. If a dipole field is added to the models by Sun *et al.*, or if the Halo field is modified, almost all PAO events can be accounted for, in some cases even the events with the most extreme latitudes. With regards to the Halo field, the vertical scale height z_{1b}^{H} is the main factor that determines how many Galactic sources are connected to the Earth (in combination with a slight increase in the Halo magnetic field strength). The differences between the RING and ARM disk fields hardly affect the cosmic ray trajectories.

- Although the majority of trajectories that connect Galactic sources to the Earth correspond to cosmic rays emitted in the direction of the Earth (i.e. a beam angle smaller than 90°), a small proportion of cosmic rays emitted in the opposite direction also reaches the Earth.

Based on these conclusions we continue our simulations in the following chapter with only the following four GMF models:

- ASS+RING+Dipole

- ASS+ARM+Dipole

- ASS+RING($z_{1b}^{H} = 4$ kpc, $B_0^H = 3$ µG)

- ASS+ARM($z_{1b}^{H} = 4$ kpc, $B_0^H = 3$ µG)

and we change the beamangle parameter (see Appendix A) from 90° to its maximum value, i.e. the sources emit cosmic rays isotropically.

Chapter 6

Simulations II: Specific (magnetar) source distributions emitting iron nuclei

In the previous chapter we have selected four GMF models that might allow Galactic sources to reproduce the PAO arrival directions. In this chapter we will use a physically motivated distribution of sources, such as magnetars, and forwardtrack cosmic rays from these sources through the four GMF models. Since the resulting dipole-anisotropies will turn out to be inconsistent with the upper bounds set by the PAO, we will subsequently backtrack an isotropic set of arrival directions to find 'intersection hotspots in the galactic disk' (and to determine the forbidden regions). These hotspots will be used to design a fine-tuned source distribution. It will be tested whether this distribution does produce a dipole-anisotropy below the experimental upper bounds.

6.1 Spiral Arm Source Distribution

Candidates for Galactic sources of UHECR, such as magnetars, are often associated with Supernovae Remnants (SNR). Hence, we model our Galactic (magnetar) source distribution according to the SNR distribution used by Ahlers, Mertsch & Sarkar [60]. Their smoothed radial SNR distribution is modeled by

$$f(r) = A \sin\left(\frac{\pi r}{r_0} + \theta_0\right) e^{-\beta r} \tag{6.1}$$

where $A = 1.96$ kpc^{-2}, $r_0 = 17.2$ kpc, $\theta_0 = 0.08$ and $\beta = 0.13$. To take into account the spiral structure of the Galaxy, four spiral arms are adopted, with a pitch angle of 12.6° and a central bar of 6 kpc length which is inclined by 30° with respect to the direction between the Sun and the Galactic centre. The width of each arm is modeled by a Gaussian with 0.5 kpc dispersion. The resulting distribution $g(r, \phi)$ has been normalized with respect to ϕ in such a way that eq. 6.1 is recovered. $g(r, \phi)$ has been plotted in

Figure 6.1 together with the 15 Galactic magnetars with approximately known distances, which fit reasonably well with the spiral arm model. Although there is admittedly no consensus about the number of magnetars in our Galaxy (estimates differ by several orders of magnitude), we adopt the values estimated by Muno *et al.* [61], who argue that there are 59^{+92}_{-32} easily detectable Galactic magnetars and < 540 magnetars in total (at the 90% confidence level). This estimate is low/intermediate compared to other estimates in the literature. If we take a random realisation of x sources from the density distribution $g(r, \phi)$, the chance of asymmetric fluctuations, which are expected to lead to a dipole-anisotropy of type a (see Figure 2.2), is greatest for low x. Hence, we intially assume 540 magnetars. As shown in Chapter 5.1 and in Figure 5.7, sources within 4 kpc of the Galactic centre can be safely neglected when a dipole field is used, in order to significantly reduce computing time.

As mentioned in Appendix A, the detector radius has to be sufficiently large to produce enough hits within the available computing time, and sufficiently small compared to the gyroradius for the results to be accurate. When using random realisations of 540 magnetars there is an additional constraint: none of the magnetars can be too close to the detector and, in particular, they cannot be located within the detector. In Figure 6.1 we have plotted the average amount of sources that would be located inside the detector, as a function of detector radius. Our previous choice, $R_{det} = 0.1$ kpc, turns out to remain appropriate.

Galactic skymaps of the simulated arrival directions (for 50,000 emissions per source) have been plotted in Figure 6.2 for the GMF models with a modified Halo component and in Figure 6.3 for the GMF models with an additional dipole component. Two things are notable. Firstly, although most parts of the sky contain at least a few hits (for the GMF models with a modified Halo), there is a significant anisotropy for all four GMF models. The simulations with the modified Halo fields show higher densities in a band that can be described approximately by a cosine ($\cos(long + long_0)$) which intersects the Galactic plane (zero latitude) at $long = 78°$ and $long = -102°$, see the red region in Figure 6.4. Hits between these longitudes arrive predominantly from positive latitudes; hits outside this longitude range arrive predominantly from negative latitudes. The band width is approximately 30° latitude. This pattern seems to stem from the local magnetic field at the position of the Sun. The magnetic field line intersecting the Sun comes from $-102°$ *long* and leaves at 78° *long*. Cosmic rays travelling along these field lines experience no Lorentz force and remain in the Galactic plane. (Positively charged) cosmic rays coming from the direction of the Galactic center are deflected Southward and cosmic rays coming from the opposite direction are deflected Northward. In case of the GMF models with an added dipole component (pointing upwards at the location of the Sun), particles originating from directions close to the Galactic centre (i.e. the majority of sources in our model) are deflected clockwise (as seen from the Galactic North pole) and hence arrive predominantly from negative longitudes. This provides a strong experimental signature: if these GMF models reflect reality, the future North Station of the PAO is expected to detect very few events compared to the current South Station. Summarising, the local magnetic field dominates the pattern of arrival directions. Secondly, we observe several 'hotspots' on the sky, plotted in red. The plots on the right of figure Figure 6.2 show that there are indeed a few dominating sources that are responsible for the majority of the hits. As expected, these sources turn out to be the sources closest to the Sun. Although we have chosen a source distribution with a large number of sources, in order to prevent a dipole-anisotropy resulting from an asymmetric source distribution (see Figure 2.2, type a), the local (asymetrically distributed) sources might produce such an anisotropy nonetheless.

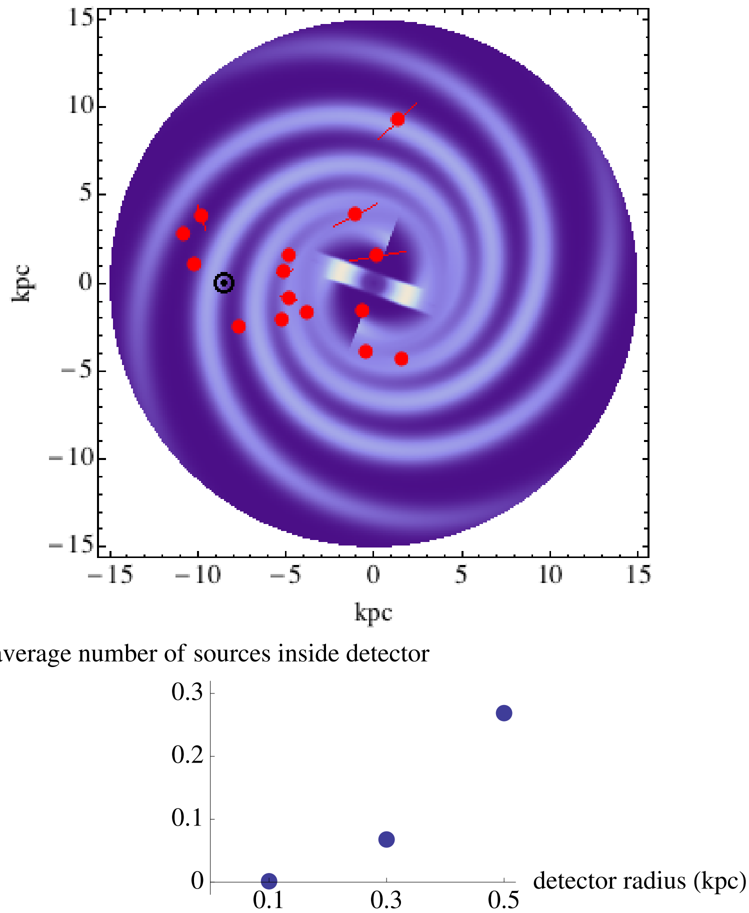

Figure 6.1: Distribution of sources in spiral arms [60]. *Above:* The spiral arm surface density is plotted together with the 15 Galactic magnetars with approximately known distances (red dots; data taken from `http://www.physics.mcgill.ca/~pulsar/magnetar/main.html`). The uncertainty in their distance is represented by red lines. *Below:* The average number of sources that is located inside the CRT detector, for random realisations of 540 source positions from the spiral arm density distribution.

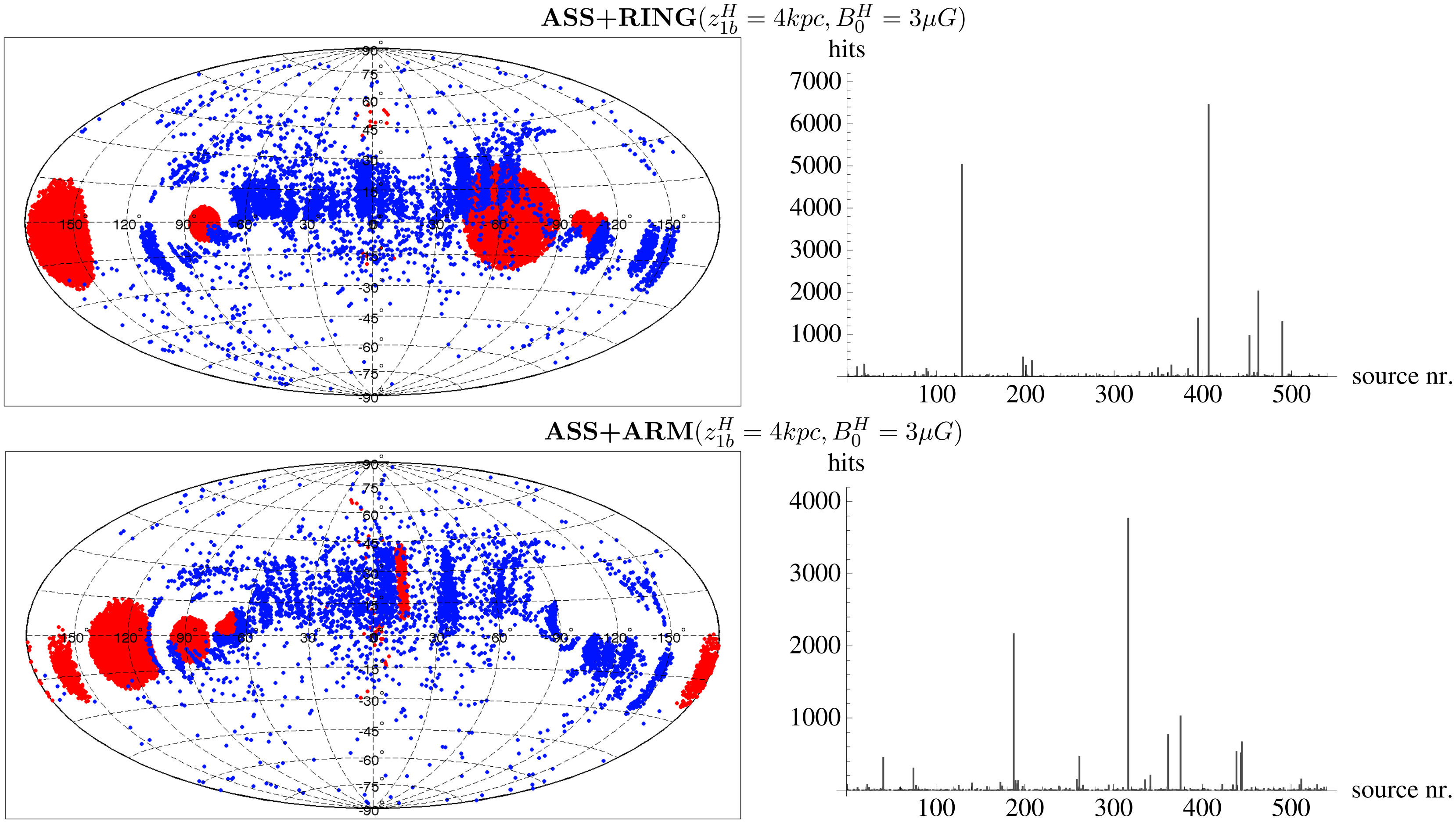

Figure 6.2: *Left:* Galactic skymaps of arrival directions of iron cosmic rays emitted from (different) random realisations of 540 magnetar positions from the spiral arm density distribution, for the ASS+RING (top) and ASS+ARM (bottom) models with modified Halo parameters. Red hits originate from the 6 (RING) or 9 (ARM) most dominant (i.e. closest) sources; the remaining hits are blue. Each magnetar emits 50,000 cosmic rays. *Right:* The corresponding hits per source.

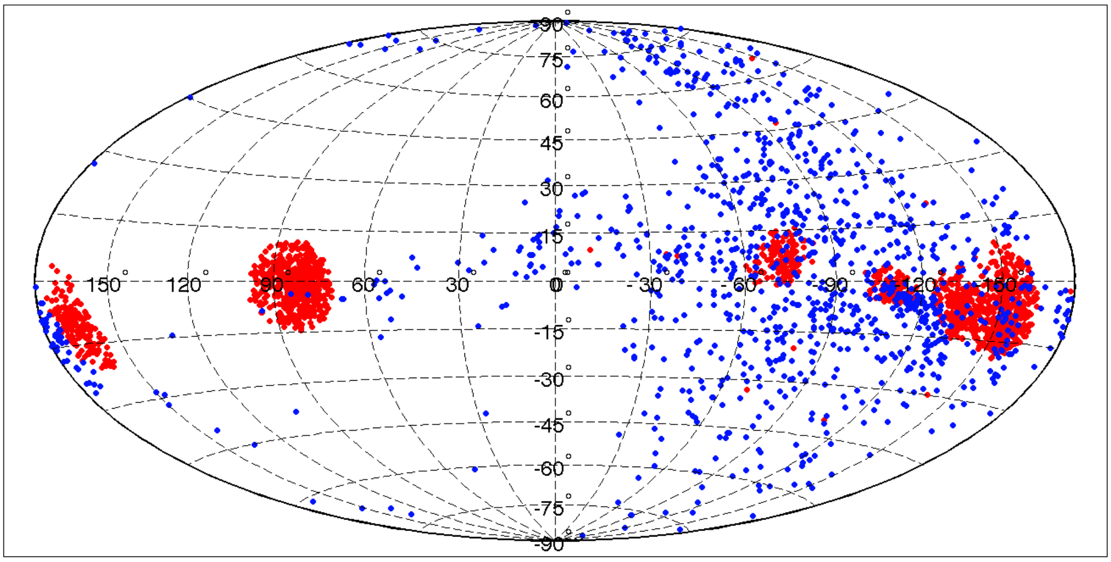

ASS+ARM+Dipole

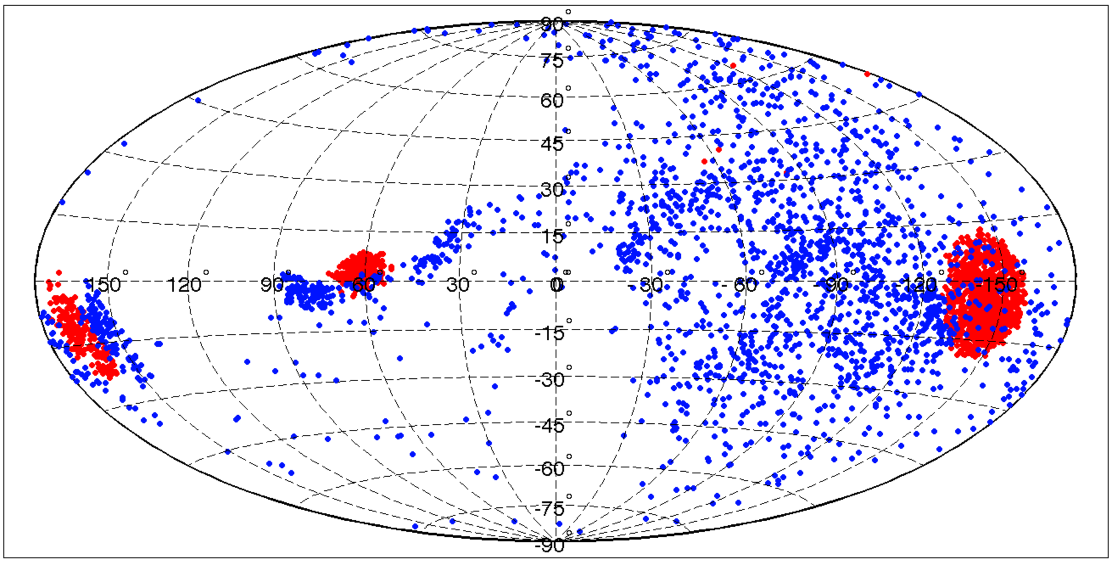

Figure 6.3: Galactic skymaps of arrival directions obtained from (different) random realisations of 540 magnetar positions from the spiral arm density distribution, for the ASS+RING+Dipole (top) and ASS+ARM+Dipole (bottom) models. Red hits originate from the 6 (RING) or 3 (ARM) most dominant (i.e. closest) sources.

The fractional dipole-anisotropies of the simulated arrival directions have been calculated using HEALPix. All data has been binned into 48 HEALPix pixels. The angular power spectrum has been computed from this binned data. The fractional dipole amplitudes have been calculated from this power spectrum and are listed in Table 6.1 together with the fractional amplitudes of the first harmonic modulation in right-ascenscion (to be compared to experimental results) and galactic longitude (to be compared to theoretical predictions). It should be mentioned that HEALPix is not completely accurate when some pixels contain zero hits. Furthermore, the first harmonic modulation in right-ascension and galactic longitude can only be equated to the dipole component in the equatorial and galactic plane, respectively, if the dipole lies (almost) in that plane. This is not true in general, and definitely not for some of the simulations. Nevertheless, the calculated values provide a useful order of magnitude and are all inconsistent with the upper bounds by the PAO ($\sim 10\%$). In order to determine whether the large dipole-anisotropies stem from the local (asymetrically distributed) sources, the previous values have been recalculated without the hits from the most dominating sources (see the values in brackets). The new dipoles are smaller in some cases, but in many cases they are significantly lager. We conclude that the dipole-anisotropies arise from a combination of the local asymmetrical distribution of sources (see Figure 2.2, type a) and the asymmetrical position of the Sun in the Galactic plane (type c). Finally, it should be noted that the dipole-anisotropy depends significantly on the specific realisation of sources used. For example, we have previously concluded that the differences in the disk fields of both models by Sun *et al.* hardly affect the cosmic ray trajectories. The dipoles do show a significant discrepancy. This stems from the different source realisation used, and not from the differences in the disk fields. A systematic approach should repeat the previous calculations for many different realisations of 540 sources. However, such a study is computationally very expensive while the current results suggest that the chances of finding a realisation with a dipole below the experimental limits is small.

One might expect that source distributions with a smaller number of sources could decrease the dipole-anisotropies, since this would reduce the chance of a few nearby sources dominating the detected cosmic rays. However, simulations with 100 and 50 sources result in dipoles of a similar order of magnitude. It could furthermore be argued that the dipole upper bound set by PAO for the energy bin ranging from 8 EeV to the highest energy, is compatible with a higher dipole for ultrahigh energies (> 55 EeV). Only 69 of the ~ 5000 events in this energy have an ultrahigh energy. A large dipole for the highest energy range could easily be averaged out by the large amount of lower energy cosmic rays in the bin. This hypothesis is falsified by simulations with energies $E \geq 8$ EeV (using the ASS+RING($z_{1b}^H = 4$ kpc, $B_0^H = 3$ µG) model), which produce a dipole of $62.6^{+4.6}_{-4.6}\%$, and amplitudes of $52.2^{+4.6}_{-4.6}\%$ and $48.8^{+4.6}_{-4.6}\%$ of the first harmonic modulation in right-ascension and galactic longitude respectively. These values are even higher than the previously obtained values for ultrahigh energies. This might indicate that higher multipoles become more important at higher energies, but probably stems from the different realisations of sources used.

GMF model	dipole	1st harmonic mod. in RA	1st harmonic mod. in Gal. long.
ASS+RING($z_{1b}^H = 4kpc, B_0^H = 3\mu G$)	$34.5^{+1.6}_{-1.5}\%$ ($128.2^{+3.1}_{-3.1}\%$)	$33.6^{+1.6}_{-1.5}\%$ ($97.8^{+2.9}_{-2.9}\%$)	$21.9^{+1.7}_{-1.3}\%$ ($84.9^{+2.9}_{-2.9}\%$)
ASS+ARM($z_{1b}^H = 4kpc, B_0^H = 3\mu G$)	$139.7^{+1.9}_{-1.9}\%$ ($125.6^{+3.4}_{-3.4}\%$)	$87.3^{+2.1}_{-2.1}\%$ ($88.1^{+3.4}_{-3.4}\%$)	$95.6^{+1.9}_{-1.9}\%$ ($84.6^{+3.4}_{-3.4}\%$)
ASS+RING+Dipole	$99.0^{+4.7}_{-4.4}\%$ ($174.4^{+7.3}_{-7.2}\%$)	$72.7^{+4.4}_{-4.4}\%$ ($113.3^{+7.3}_{-7.2}\%$)	$77.8^{+4.5}_{-4.4}\%$ ($138.9^{+7.3}_{-7.2}\%$)
ASS+ARM+Dipole	$134.8^{+4.3}_{-3.9}\%$ ($121.5^{+5.3}_{-5.2}\%$)	$100.6^{+3.9}_{-3.9}\%$ ($79.6^{+5.2}_{-5.2}\%$)	$102.8^{+3.9}_{-3.9}\%$ ($97.7^{+5.2}_{-5.2}\%$)

Table 6.1: Fractional dipoles, amplitudes of the first harmonic modulation in right-ascension and amplitudes of the first harmonic modulation in galactic longitude (90% confidence), calculated for the arrival directions obtained from simulating cosmic rays from random realisations of 540 sources from the spiral arm density distribution. The values in brackets are calculated after removing the most dominant (i.e. closest) sources.

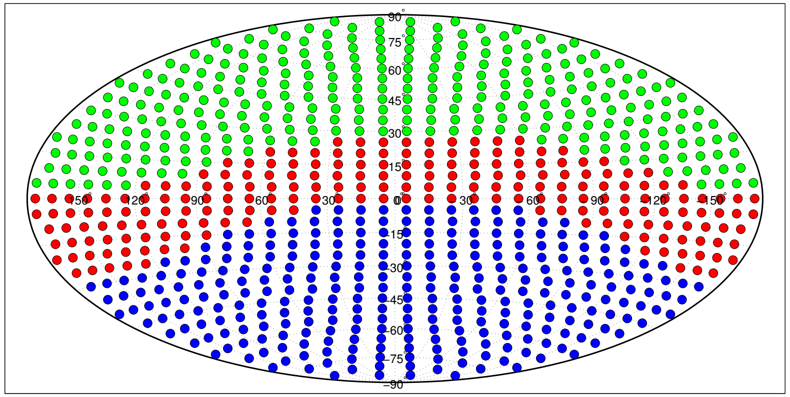

Figure 6.4: Set of ~ 800 pseudo-isotropic arrival directions. The red band reflects the effect of the local magnetic field upon cosmic ray trajectories. Its functional form is a cosine of the longitude, which intersects the Galactic plane at $long = 78°$ and $long = -102°$, the direction of the disk magnetic field line that passes through the Sun. The width of the red band is $30°$ lat. The remaining positive (negative) latitudes are colored green (blue).

6.2 Backtracking isotropic arrival directions

Although the physically motivated spiral arm source distribution in the previous section leads to results incompatible with the experimental dipole upper bounds, we will continue with backtracking an isotropic set of arrival directions. This will provide suggestions for alternative fine-tuned source distributions that might be compatible with the dipole upper bounds. It will also shed light on the connections between specific regions on the sky and specific source regions in the Galactic plane, in particular forbidden regions, i.e. regions on the sky that cannot be populated with cosmic rays by any region in the Galactic plane.

A galactic skymap of the pseudo-isotropic arrival directions is presented in Figure 6.4. Three regions are distinguished. The 'cosine band' described in the previous section is colored red. This band represents the effect of the local magnetic field (for the two GMF models with modified Halo parameters) and contained a relatively high density of hits when forwardtracking spiral arm source distributions. We are interested in source regions in the Galactic plane that generate hits in the remaining regions above (green) and below (blue) the 'cosine band'. The intersections of the backtracked isotropic arrival directions (E = 55 EeV) are plotted in Figures 6.5, 6.6 and 6.7, together with the forbidden regions. The red intersection region for the ASS+RING(z_{1b}^H = 4 kpc, B_0^H = 3 µG) model follows the local magnetic fields lines, as expected. Sources that result in arrival latitudes above and below the 'cosine band' are mainly located in the direction opposite to the Galactic centre. The results for the ASS+ARM($z_{1b}^H = 4$ kpc, $B_0^H = 3$ µG) model are less clear, but follow the same pattern. The blue and green source regions overlap; the remaining free parameter, the emission velocity, determines the arrival directions (at Earth) of cosmic rays emitted from sources in the overlapping region. For both models, the region near the Galactic centre contains hardly any intersections, presumably because the strong Halo field in that region forms a cosmic ray barrier or trap. For the models with the added dipole field, we again observe an empty central region, as explained in Chapter 5.2. The density of intersections is approximately independent of azimuthal angle and decreases with Galactocentric radius. The forbidden regions for all four GMF models are roughly consistent with the empty regions observed in the forwardtracked skymaps in Chapter 5.1. The observed empty regions are slightly smaller. This discrepancy is explained mainly by the range of energies used in Chapter 5.1 (55 EeV $< E <$ 300 EeV) compared to the single energy used in this section ($E = 55$ EeV). The finite detector size might further be responsible for a small part of this discrepancy. Interestingly, the forbidden regions are located at intermediate positive latitudes, rather than at the most positive and most negative latitudes as initially expected. Table 6.2 lists the percentages of the sky that are forbidden. For the models with modified Halo parameters, almomst every part of the sky is connected with the Galactic plane.

ASS+RING ($z_{1b}^H = 4kpc$, $B_0^H = 3\mu G$)

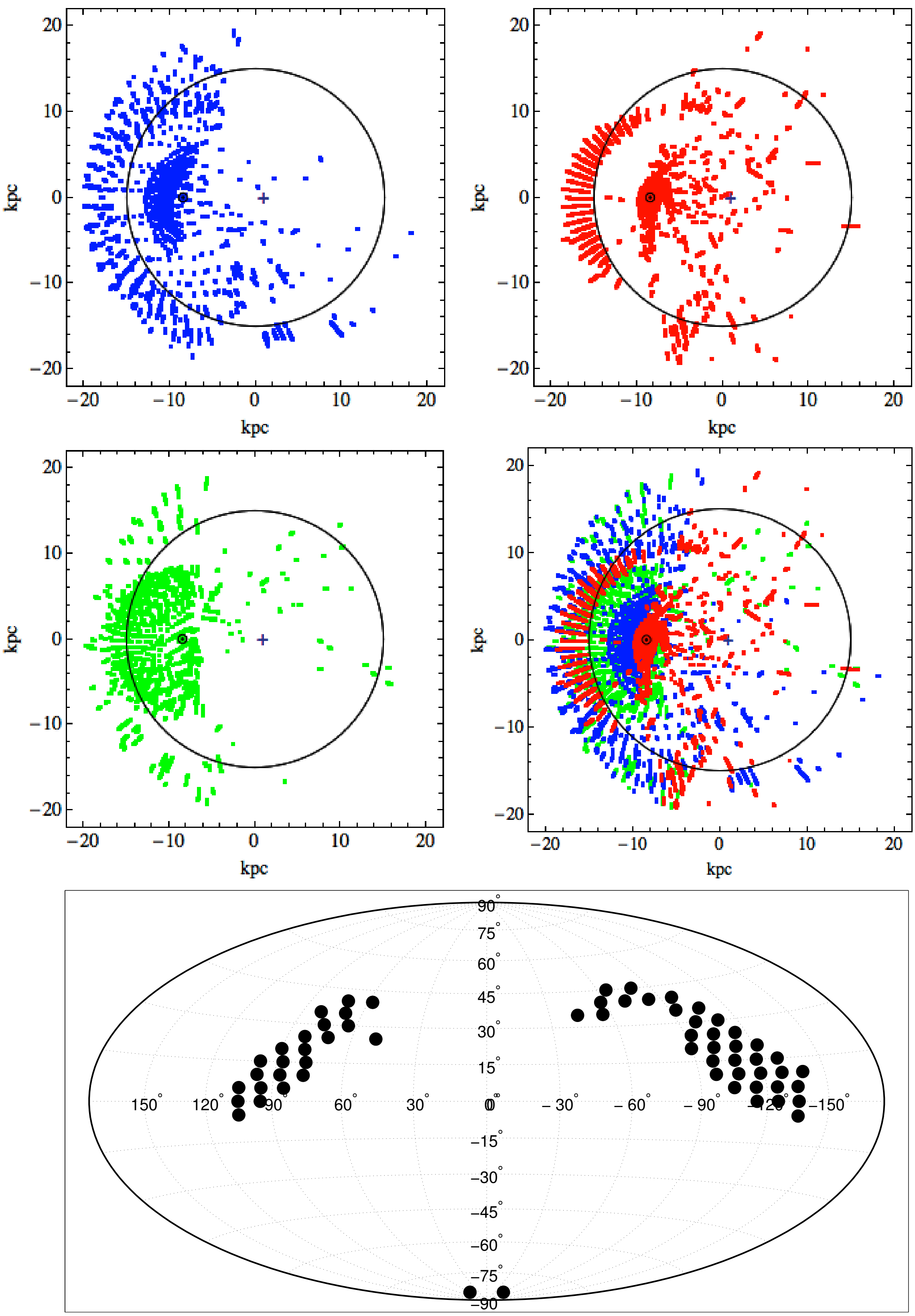

Figure 6.5: *Above:* Intersections of backtracked isotropic arrival directions ($E = 55$ EeV) with the Galactic plane. The colors correspond to the colored regions in Figure 6.4. *Below:* Forbidden regions, i.e. regions that do not intersect with the Galactic plane when backtracked.

ASS+ARM ($z_{1b}^{H} = 4kpc$, $B_0^H = 3\mu G$)

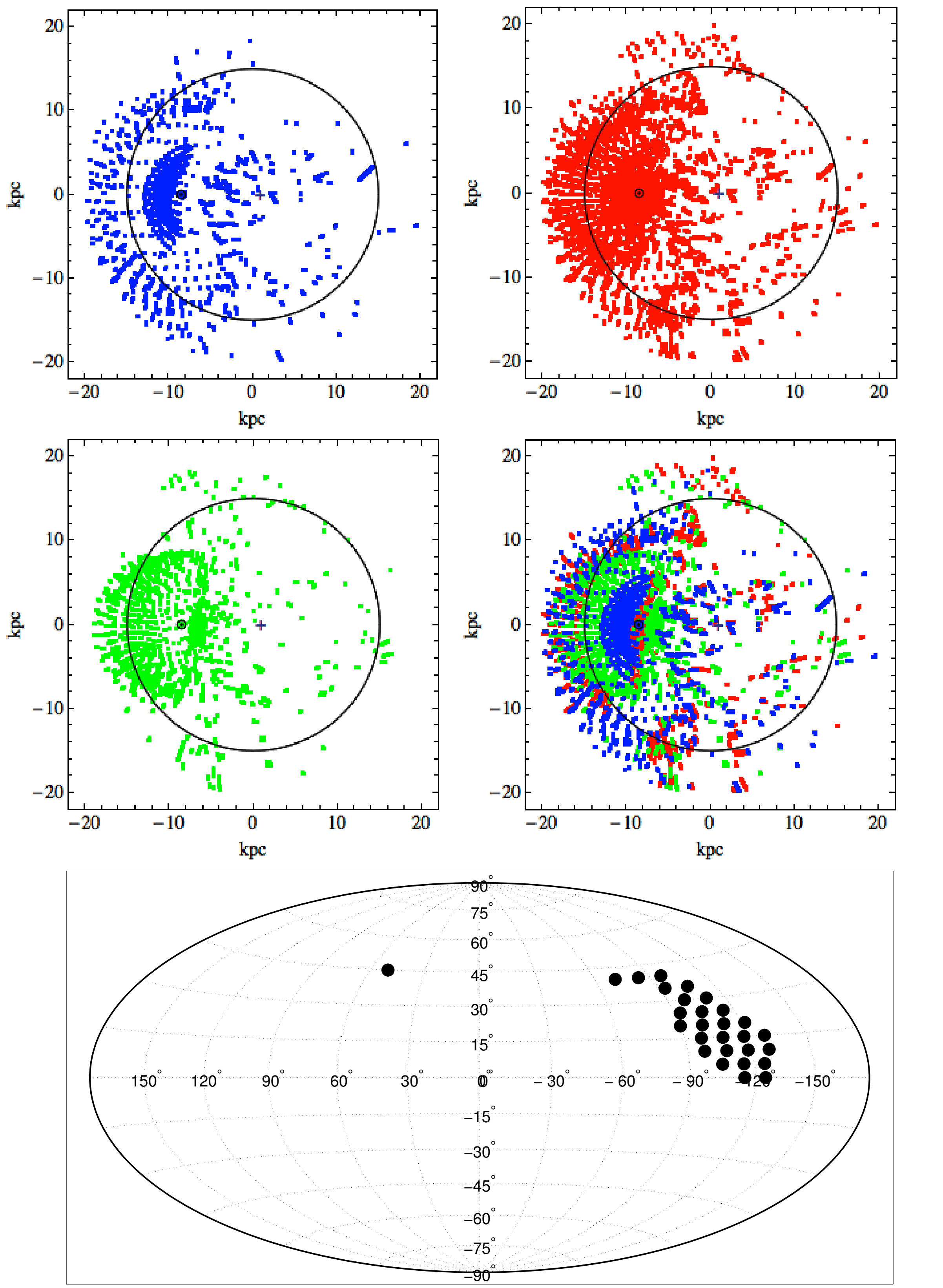

Figure 6.6: *Above:* Intersections of backtracked isotropic arrival directions ($E = 55$ EeV) with the Galactic plane. The colors correspond to the colored regions in Figure 6.4. *Below:* Forbidden regions, i.e. regions that do not intersect with the Galactic plane when backtracked.

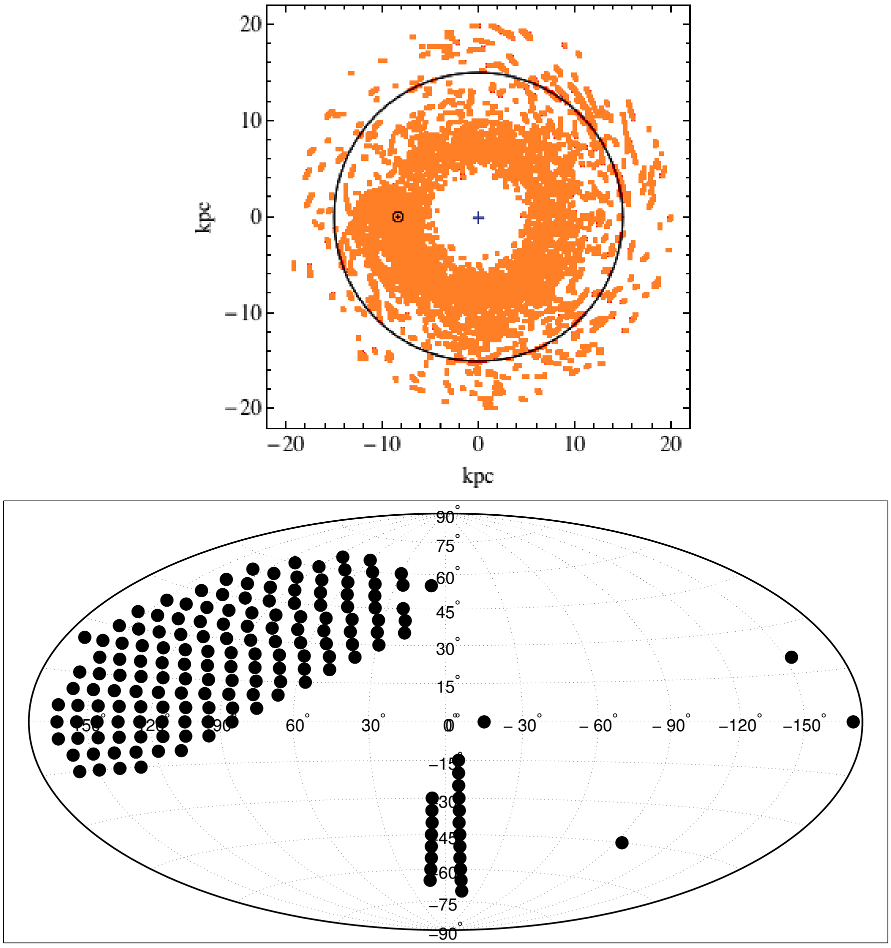

Figure 6.7: *Above:* Intersections of backtracked isotropic arrival directions ($E = 55EeV$) with the Galactic plane, for the ASS+ARM+Dipole model. *Below:* Forbidden regions, i.e. regions that do not intersect with the Galactic plane when backtracked. The results for the ASS+RING+Dipole model (not shown) are very similar.

GMF models	Forbidden region
ASS+RING($z_{1b}^H = 4$ kpc, $B_0^H = 3$ μG)	8%
ASS+ARM($z_{1b}^H = 4$ kpc, $B_0^H = 3$ μG)	3%
ASS+RING+Dipole	22%
ASS+ARM+Dipole	21%

Table 6.2: The size (%) of the forbidden regions on the sky.

6.3 Fine-tuned source distributions

In this section we focus on the blue and green regions in the Galactic plane (Figures 6.5 and 6.6) in order to increase the number of hits in the blue and green regions on the sky (Figure 6.4). It is furthermore investigated whether the source locations obtained from backtracking the PAO events (Chapter 5.2) actually reproduce the PAO observations when forwardtracked.

6.3.1 A fine-tuned source distribution

We have seen that a spiral arm source distribution generates a large dipole-anisotropy due to the abundance of arrival directions in the 'cosine band', the red region in Figure 6.4. A fine-tuned distribution of sources located in the blue and green regions in the Galactic plane (Figures 6.5 and 6.6) might reduce the dipole. If Galactic sources, such as magnetars, would turn out to emit cosmic rays only in narrow jets (e.g. along their magnetic poles), only sources that are aligned in the correct way could generate trajectories that end at the Earth. This could explain how a fine-tuned distribution of correctly aligned sources arises from an underlying larger (physically plausible) source distribution, such as the spiral arm source distribution. Figure 6.8 shows the fine-tuned source distribution used, and the resulting Galactic skymap (for 4000 emissions per source). The arrival directions with a positive latitude stem from the sources that are farthest away; the arrival directions with negative latitude stem from the closest sources. Hits from sources at the same Galactic longitude form a line. Most importantly, the 'cosine band' has disappeared; most regions of the sky contain hits except for two empty disk-like regions. Nevertheless, the corresponding dipole anisotropy ($82.2^{+7.4}_{-7.4}\%$) is still too large. The fractional amplitudes of the first harmonic modulations in right-ascension and galactic longitude are $71.0^{+7.5}_{-7.5}$ and $62.8^{+7.4}_{-7.4}$, respectively.

6.3.2 Source locations obtained from backtracking the PAO events

Both a physically motivated and a fine-tuned source distribution have turned out to generate dipole-anisotropies inconsistent with experimental results. However, we have determined that almost all PAO events intersect with the Galactic plane when backtracked. Would the observed set of arrival directions be reproduced if cosmic rays are emitted isotropically from the locations determined by these intersections? Denote the arrival directions observed by the PAO by AD_i and their energies by E_i, where the event index $i = 1, .., 69$. The backtracked trajectories of AD_i either do not intersect the Galactic plane, or they intersect the Galactic plane at the locations $L_{i,j}$ with velocity $V_{i,j}$. The intersection index j can have any positive integer value. Obviously, the AD_i would be reproduced if we choose one $L_{i,j}$ per trajectory, place a source on that location and emit one cosmic ray in the direction $-V_{i,j}$. However, in reality sources are not emitted in one single direction, but either in a cone/jet, in a plane, or isotropically. In this section we place sources on all the locations $L_{i,j}$ and simulate cosmic rays emitted isotropically with an energy sampled from a spectrum with spectral index -2.7, $E_{min} = 55$ EeV and

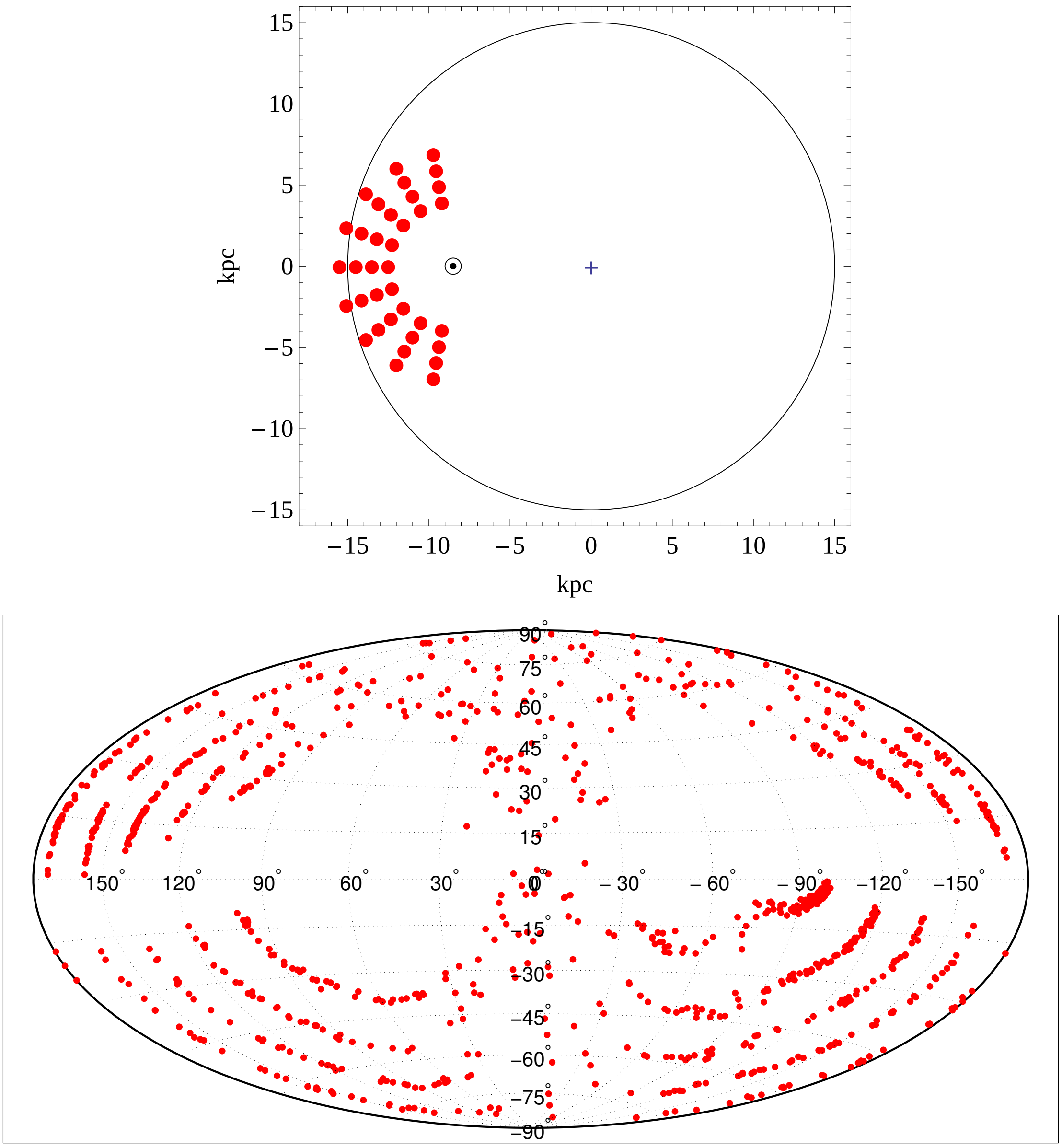

Figure 6.8: Fine-tuned source distribution (*top*) and the corresponding Galactic skymap of arrival directions (*bottom*).

$E_{max} = 300$ EeV. There are four reasons why this might not reproduce the AD_i:

- Oversampling of certain events: some trajectories intersect the Galactic plane multiple times. Since there is no reason to prefer one of the corresponding $L_{i,j}$'s over the other, they have all been included in the source distribution.
- For a finite detector size, cosmic rays emitted with a velocity sufficiently close to $-V_{i,j}$ will also hit the Earth. The opening angle of this cone-like set of emission directions will, in general, decrease with the source-Earth distance and, in detail, depend on the specific magnetic field configuration along the trajectory. A larger opening angle increases the chance that an isotropically emitted cosmic ray has one of the required velocities to arrive at Earth. Hence, a larger opening angle corresponds to a larger observed flux in the neighbourhood of the corresponding AD_i.
- Cosmic rays emitted with an energy that is not equal to the corresonding E_i will often not arrive at Earth, but might hit the Earth in a few cases, with an arrival direction radically different from AD_i.
- One or several emission velocities (and their surrounding velocities) radically different from $-V_{i,j}$ might also generate a trajectory that hits the Earth.

The first two items will produce (approximately) the correct PAO arrival directions, but some directions will be oversampled and for other directions the flux will be too low. The latter two items could lead to a completely different pattern of arrival directions. In order to check whether the last item occurs, the set of $V_{i,j}$'s has been plotted in Figure 6.9, in bins of 1 kpc^2. In the region left of the Sun ($|long| \gtrsim 90°$), all the $V_{i,j}$'s point in approximately the same direction. Hence, in this region only emissions in the neighbourhood of $-V_{i,j}$ result in a hit at the Earth. In the remaining part of the Galaxy the $V_{i,j}$'s become more chaotic; it is likely that two cosmic rays observed at Earth, which both originate in this region, have been emitted in radically different directions. Plotting these velocities for the three colored regions in Figure 6.4 separately (not shown) gives almost similar patterns. These plots also show that the argument made in the previous subsection, regaring the fine-tuned subset of sources with narrow emission jets, is highly unlikely. Since the fine-tuned sources in that subsection are all located left of the Sun, their jets/poles would all need to be aligned parallel to each other in order produce cosmic rays that hit the Earth. Finally, the arrival directions obtained by forwardtracking cosmic rays from the locations $L_{i,j}$ are plotted in Figure 6.10, for the GMF models with modified Halo parameters. They are very different from the PAO observations, due to a combination of the abovementioned four reasons. No simulations have been done for the GMF models with an additional dipole field, for reasons of limited computing time and the similarity of the corresponding $L_{i,j}$'s with the source distributions in Chapter 5.1 and 6.1.

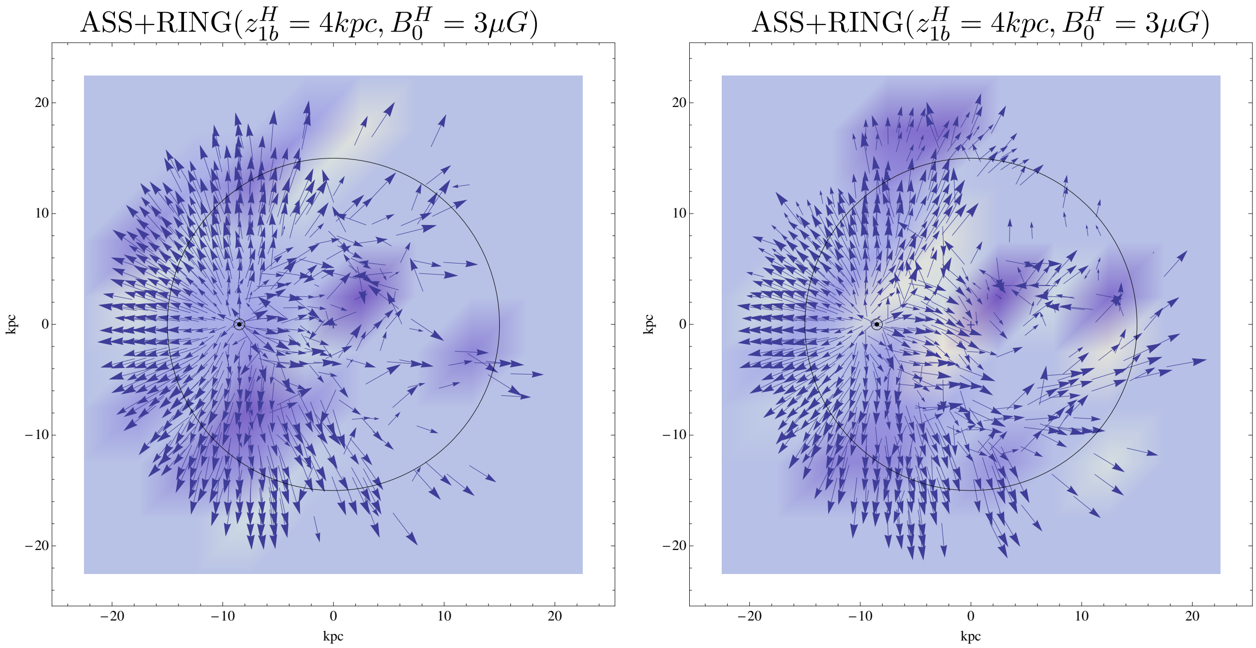

Figure 6.9: Velocities of backtracked isotropic arrival directions when intersecting the Galactic plane, binned in squares of 1 kpc^2. The arrows represent the velocity in the plane; the background color represents the out-of-plane-velocity. Regions without arrows are not intersected by any of the backtracked trajectories. Inverting the plotted velocities would give the emission directions required to hit the Earth.

6.4 Conclusions

- Although almost all regions on the sky contain at least a few hits, the local field configuration and nearby sources form the main determinants of the pattern of arrival directions, resulting in a 'cosine band' and hotspots, respectively.

- Hence, the arrival directions obtained by forwardtracking iron cosmic rays from random realisations of 540 source positions from a spiral arm source density distribution are characterised by dipole-anisotropies several times the upper bound set by the PAO. These results apply to all four GMF models (i.e. both models by Sun *et al.* with either an additional dipole component or modified Halo parameters), and remain valid for a lower number of sources and after removing the nearby dominant sources.

- Backtracked trajectories intersect with the Galactic plane for almost every arrival direction. Nevertheless, although a fine-tuned source distribution does not show the 'cosine band' or the hotspots, its dipole-anisotropy is still several times the upper bound set by the PAO. Forwardtracking cosmic rays from locations obtained from intersections of backtracked PAO events with the Galactic plane does not generate a sufficiently small dipole-anisotropy either.

ASS+RING($z_{1b}^{H} = 4kpc, B_0^H = 3\mu G$)

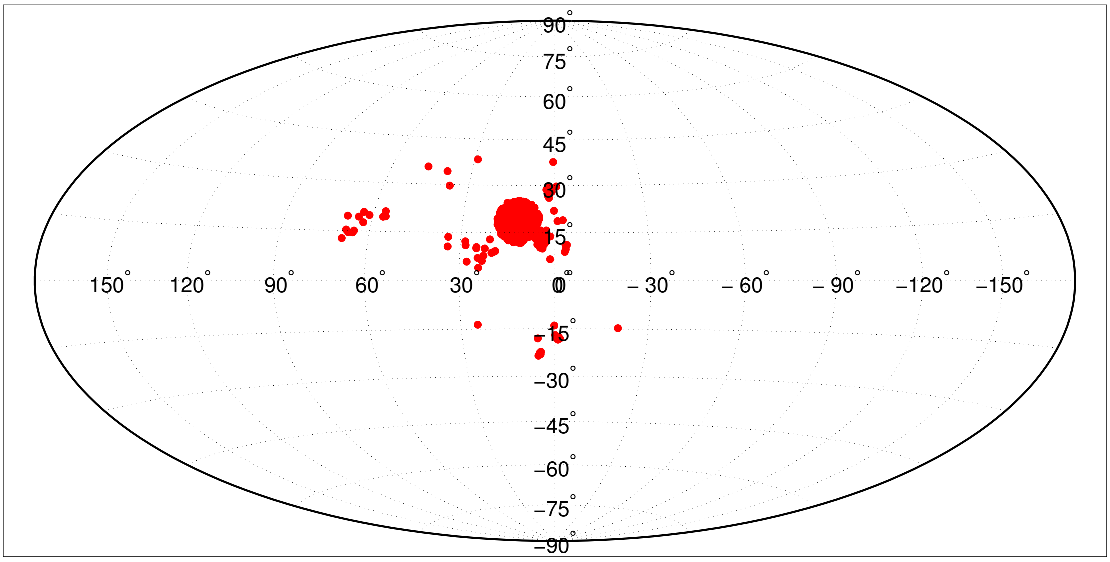

ASS+ARM($z_{1b}^{H} = 4kpc, B_0^H = 3\mu G$)

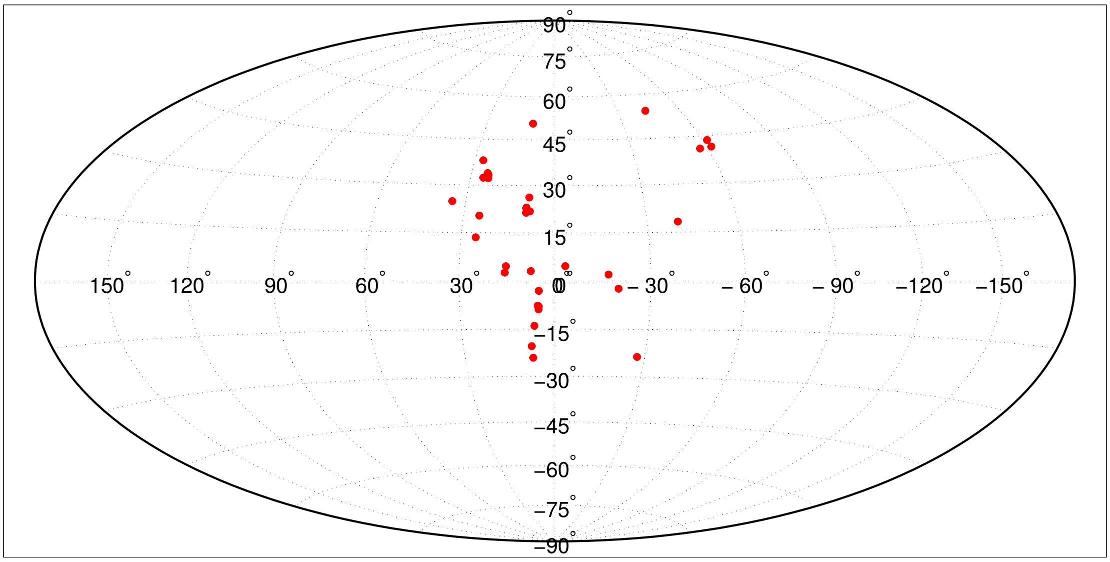

Figure 6.10: Galactic skymap of arrival directions obtained by forwardtracking cosmic rays from source locations which correspond to the intersections of the backtracked PAO events with the Galactic plane.

Chapter 7

Discussion

As mentioned in Appendix A, the detector size must be much smaller than the gyroradius of the simulated cosmic rays in the neighbourhood of the detector, in order for the simulated arrival directions to be accurate. The field strength at the Sun is ~ 2 μG for the three GMF models used, which corresponds to a maximum gyroradius of ~ 1 kpc for iron nuclei. Hence, a detector radius of 0.1 kpc has been used. In order to check whether the curvatures of the simulated iron cosmic ray trajectories indeed do not exceed kpc^{-1}, a varied range of arrival directions at Earth has been backtracked. The curvatures of these trajectories have been sampled every 100 lightyears, within 2 kpc from the Sun. Histograms of these curvatures are shown in Figure 7.1. It turns out that the curvature regularly exceeds the theoretical limit of $\sim 1\mathrm{kpc}^{-1}$. The curvatures above 10^5 kpc^{-1} are explained by round-off errors due to the limited amount of significant numbers of the CRT-output (CRT is the software used to simulate cosmic rays, see Appendix A). Curvatures between 1 and 10^5 kpc^{-1} cannot be explained by round-off errors. The large scale behavior of the backtracked trajectories shows no kinks and is consistent with the theoretical curvature limit. This suggests that these high curvatures have no significant effect on the accuracy of the simulations in this thesis. The high curvatures probably stem from internal round-off errors in CRT. Further research should clarify why these high curvatures seem to occur.

Figure 2.9 shows not only experimental upperbounds of the dipole-anisotropy, but also two theoretical predictions, by Calvez *et al.* [31] and by Giacinti *et al.* [22]. Although these predictions are obtained with different methods than the methods used in this thesis, and are valid for a lower energy range only, an extrapolation of these predictions seems to be consistent with the dipole-anisotropies calculated in this thesis. Nevertheless, some critical notes can be made with regards to both predictions. Calvez *et al.* assume that the cosmic ray trajectories are dominated by the random magnetic field component (the diffusive approximation/regime). Therefor, the transport equation is used rather than the Lorentz Force law. At the highest end of their energy range, which almost coincides with our energy threshold, this assumption becomes invalid and the regular field components should be included. Furthermore, samples of 10^3 sources from an underlying source density are used, but the final results do not include the uncertain-

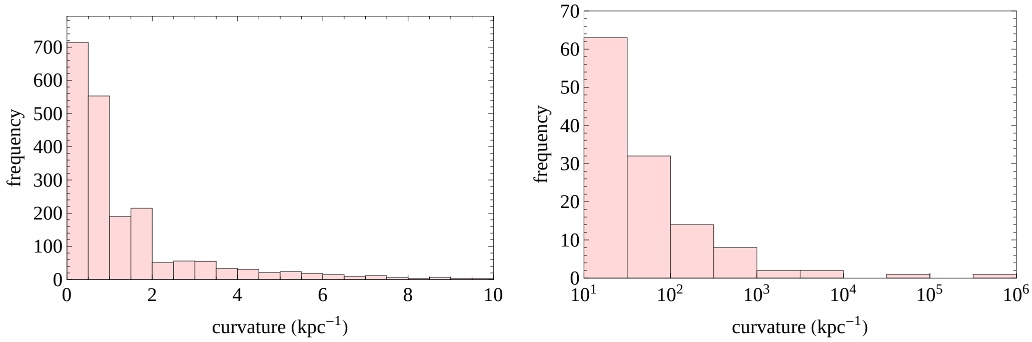

Figure 7.1: Histograms of curvatures obtained by backtracking iron cosmic rays at Earth. The curvatures of the backtracked trajectories are sampled every 100 lightyears (within 2 kpc of the Sun only). The left histogram contains curvatures from 0 to 10 kpc^{-1} and the right histogram curvatures from 10 to 10^6 kpc^{-1}. Notice the different scales on the vertical axes.

ties arising from these different samples. Giacinti *et al.* take into account both regular and turbulent magnetic fields, and propagate individual cosmic rays rather than using the transport equation. They assume a source region with a continuous homogeneous distribution of sources. A set of 10^4 randomly generated arrival directions AD_i is backtracked. For each backtracked trajectory, the length of the trajectory within the source region w_i is recorded. A larger w_i indicates that more sources are capable of contributing to cosmic rays arriving at Earth from AD_i. Hence, the set of w_i's provides a weight for each AD_i, whith which the dipole-anisotropy can be calculated. Although a rough estimation of the uncertainties in the dipole-anisotropies are given, they are not calculated systematically. Firstly, the initial set of 10^4 randomly generated arrival directions might be anisotropic itself. From the Rayleigh formula for the probability of obtaining a fractional dipole amplitude greater than r when taking N samples/measurements from an isotropic distribution,

$$P(>r) = e^{-\frac{r^2 N}{4}}, \tag{7.1}$$

we find, for instance, that there is indeed a chance of 37% that the set of arrival directions has a fractional dipole amplitude of 2 or more percent. Secondly, the uncertainty in the dipole-anisotropy could have been calculated analogously to the method used by Linsley [26], see Chapter 2.3.3. Furthermore, this method is only valid for a continuous source distributed, as acknowledged by the authors. This is approximately correct for 540 sources/magnetars, but not for e.g. 50 sources. On a different note, Giacinti *et al.* suggest that higher multipoles become more important at the highest energies. This is consistent with this thesis; see for instance the angular power spectrum of the arrival directions obtained by forwardtracking iron cosmic rays from a spiral arm source distribution through the ASS+RING($z_{1b}^H = 4$ kpc, $B_0^H = 3$ μG) GMF model (Figure 7.2).

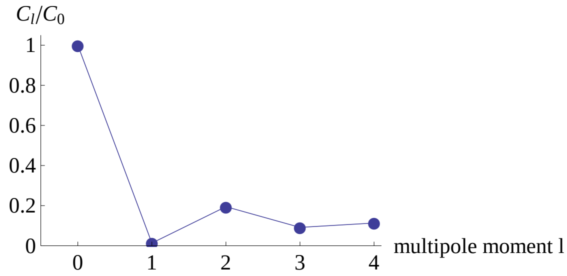

Figure 7.2: Angular power spectrum of the set of arrival directions obtained by forwardtracking iron cosmic rays from a spiral arm source distribution through the ASS+RING(z_{1b}^H = 4 kpc, B_0^H = 3 μG) GMF model. The multipole moments $l = 0, 1, 2, ...$ correspond to the monopole, dipole, quadropole, etc. The monopole (C_0) is normalised to unity.

In order to find extragalactic sources of UHECR, the scientific community has focussed mostly on increasing the global statistics and on enlarging catalogues with possible source candidates. The bottleneck in the search for the origins of UHECR is however the lack of detailed knowledge of our Galactic Magnetic Field. Although extragalactic UHECR are hardly deflected during the major part of their travel to Earth, through the intergalactic magnetic fields, heavy cosmic rays are significantly deflected during the final part of their journey, through the Galactic magnetic field. In order to show this, the PAO events have been backtracked until they leave the Galaxy. The angular difference between the velocity at Earth and the velocity of the cosmic ray when it exits the Galaxy has been plotted in Figure 7.3 for protons and in Figure 7.4 for iron nuclei. Similar plots are presented in Figure 7.5 where an isotropic set of arrival directions has been backtracked, assumning an iron composition and an energy $E = 55$ EeV. Although the GMF significantly deflects proton cosmic rays only when a dipole field component is added, iron cosmic rays are deflected up to $\sim 160°$ for all GMF models considered in this thesis. Thus, if the composition of UHECR is indeed heavy, it is useless to calculate a correlation with an extragalactic source catalogue if the GMF is not corrected for! Future research should focus on detailed knowledge of the Galactic magnetic field.

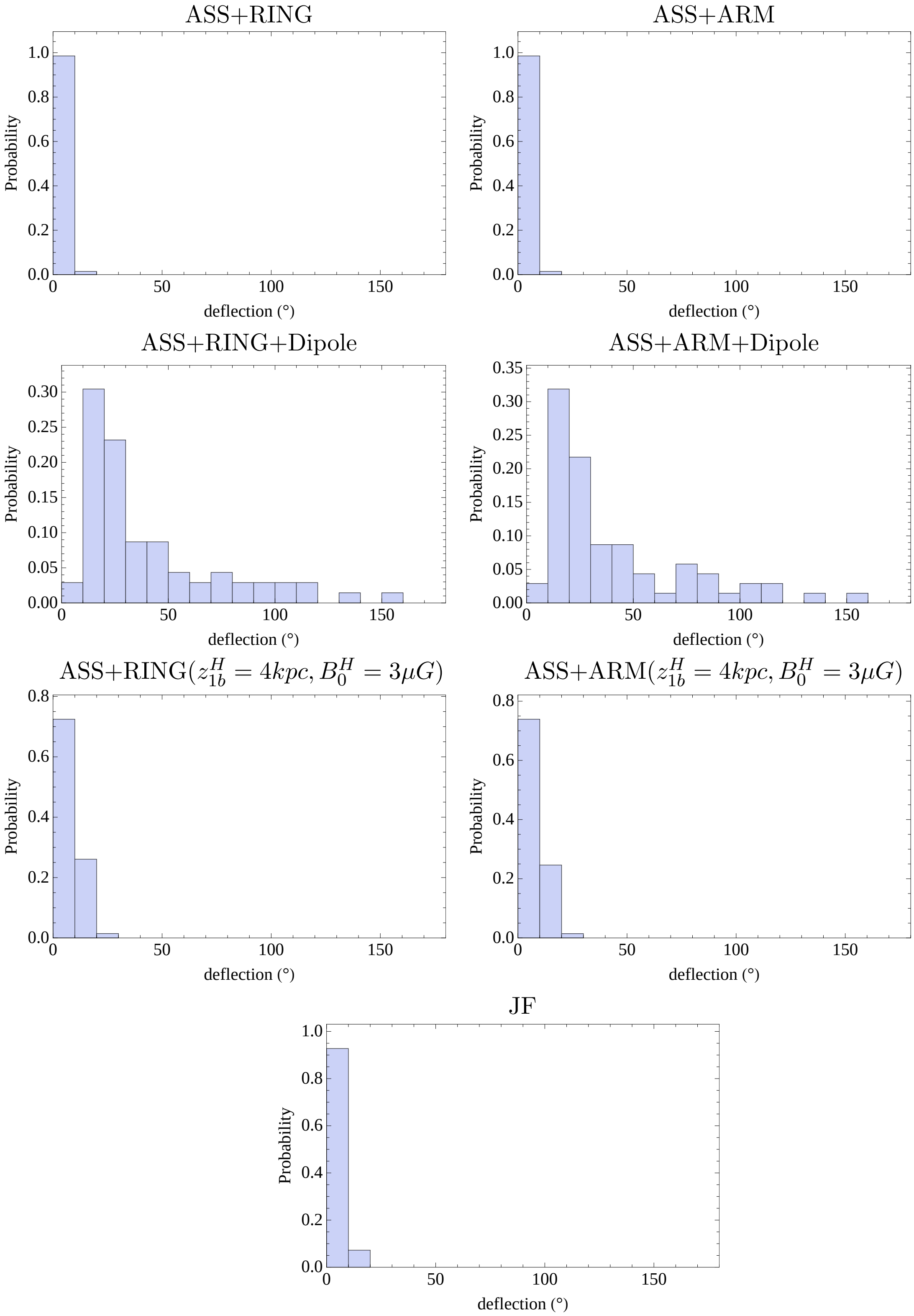

Figure 7.3: Deflections obtained by backtracking the PAO arrival directions until they leave the Galaxy, assuming a proton composition. The deflection is given by the difference between the arrival direction and the direction (not the location!) of the cosmic rays when exiting the Galaxy.

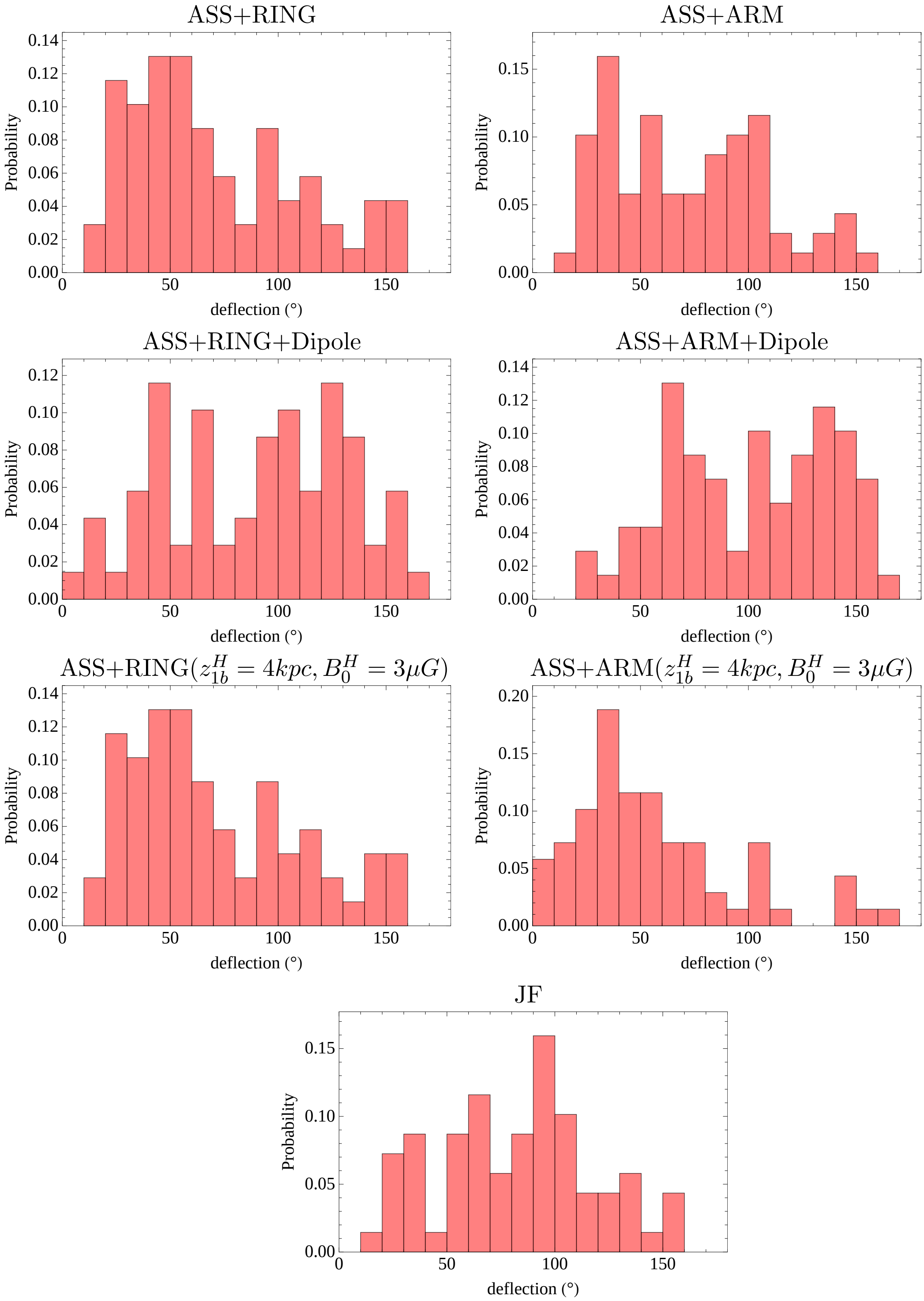

Figure 7.4: Deflections obtained by backtracking the PAO arrival directions until they leave the Galaxy, assuming an iron composition. The deflection is given by the difference between the arrival direction and the direction (not the location!) of the cosmic rays when exiting the Galaxy.

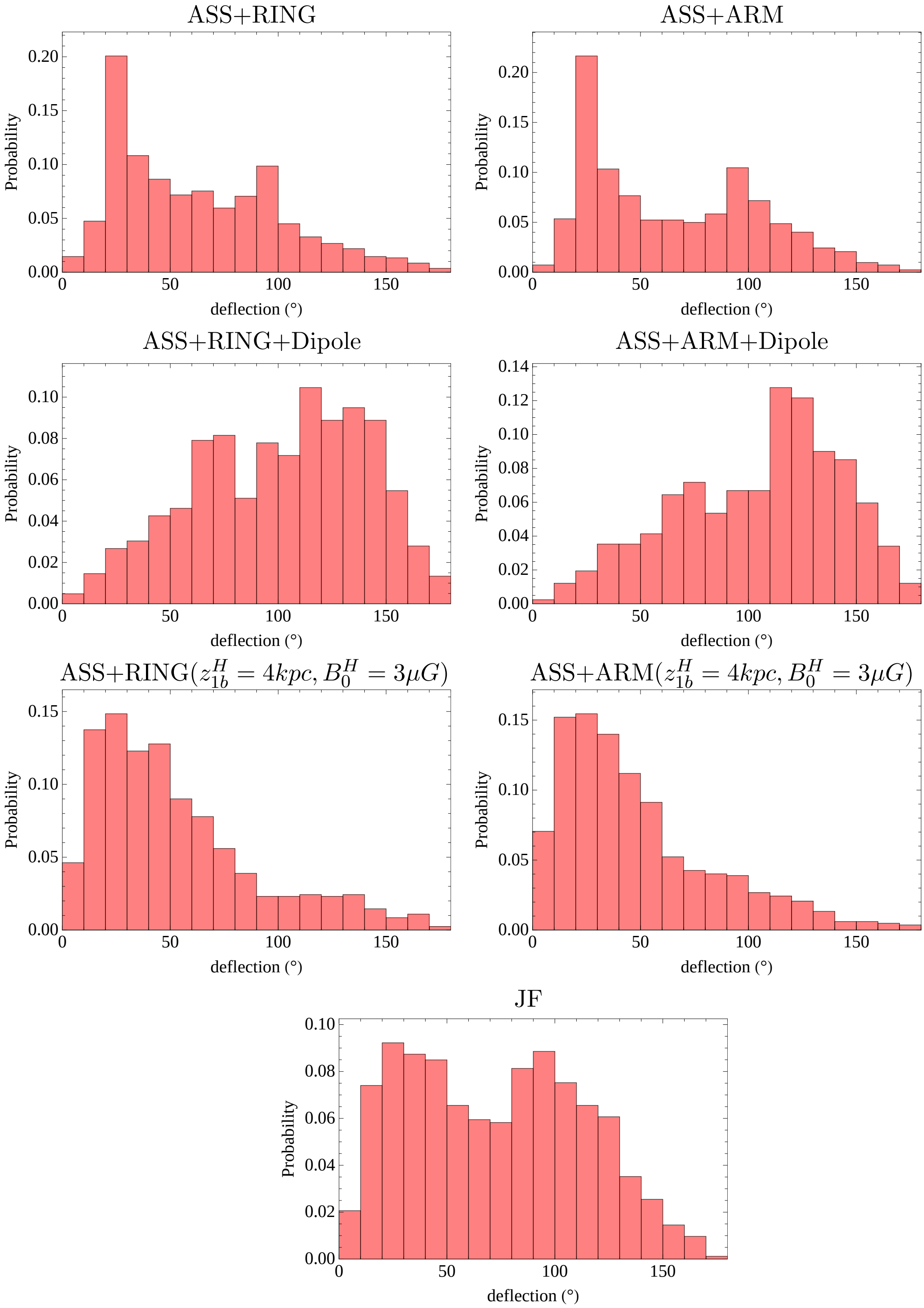

Figure 7.5: Deflections obtained by backtracking an isotropic set of cosmic ray arrival directions until they leave the Galaxy, assuming an iron composition. The deflection is given by the difference between the arrival direction and the direction (not the location!) of the cosmic rays when exiting the Galaxy.

Chapter 8

Conclusion

In this thesis we have scrutinized the four arguments that are usually mentioned in favour of an extragalactic origin of ultrahigh-energy cosmic rays, taking into account recent measurements suggesting a heavier composition at ultrahigh energies. The first two arguments have been discussed qualitatively. A quantitative response to the latter two arguments has been given by simulating ultrahigh-energy cosmic ray trajectories from several Galactic source distributions through (several versions of) two Galactic magnetic field models by Sun *et al.* and one model by Jansson & Farrar.

- **A lack of plausible Galactic source candidates.** Source candidates need to satisfy three criteria:
  The Hillas criterium: this criterium is satisfied by for instance magnetars, and for heavier compositions it is satisfied by even more source candidates.
  Energetics: a very rough estimation of the energy content of magnetars shows that even one magnetar should be sufficient to generate the UHECR flux.
  An adequate acceleration mechanism: this requirement lies outside the scope of this thesis.

- **The GZK cut-off.** The GZK effect requires sources of UHECR to be nearby, which is consistent with very nearby (Galactic) sources. If the cut-off at the end of the cosmic ray spectrum is a GZK cut-off, this only proves that cosmic rays with lower energies are extragalactic. Moreover, the cut-off can also be explained by a source cut-off or by adjusting the acceleration mechanism parameters.

- **A Milky Way of arrival directions is expected from Galactic sources, but cosmic rays from all directions are observed.** For proton cosmic rays, the backtracking method confirms that only $\sim$ 10 - 20 % of the arrival directions observed by the Pierre Auger Observatory intersects the Galactic plane when backtracked, for all three Galactic magnetic field models. This means equivalently that only $\sim$ 10 - 20 % of the PAO arrival directions could be reproduced with Galactic sources. The forwardtracking method shows that proton cosmic rays can indeed only reach latitudes of $|lat| < 15°$, unless a dipole field component is added. In this case, latitudes of $|lat| < 40^\circ$ can be reached, but only in the region that is usually attributed to the Cen A galaxy or the Centaurus cluster. Summarising, proton cosmic rays originating in the Galaxy cannot reproduce the observed arrival directions! For iron cosmic rays, it turns out that the detailed structure of the disk field hardly affects the cosmic ray trajectories. A strong and large Halo field, or a dipole component, have the largest effect upon the cosmic ray trajectories. The PAO events still cannot be reproduced for the three regular Galactic magnetic field models. However, if an additional dipole component is added, or if the Halo field is made stronger and bigger, more than 90% of the PAO events intersects with the Galactic plane when backtracked. Only a few regions on the sky are disconnected with the Galactic plane. Interestingly, these forbidden regions are not near the Galactic poles: for iron cosmic rays it is possible to reach all latitudes. Concluding, the third argument holds up for proton cosmic rays (which indeed produce a Milky Way of arrival directiosn), but is refuted for iron cosmic rays (which arrive at the Earth from almost every direction).

- **There is a strict upper bound on the dipole-anisotropy of the arrival directions, which forms the main signature of a Galactic origin.** Simulations of iron UHECR emitted by a Galactic spiral arm source distribution of 540 sources result in arrival directions covering almost all regions of the sky. However, several hotspots are visible (stemming from nearby sources) and also specific regions with a higher density (reflecting the local magnetic field configuration). Therefor, the amplitude of the dipole-anisotropies is several times the experimental upper bound. Dipole-anisotropies of the same order are obtained with a lower number of sources, with lower energies ($E > 8$ EeV) and with fine-tuned source distributions. Concluding, the dipole upper bounds rule out a Galactic origin of UHECR, even for an iron composition.

Summarising, the first two arguments against a Galactic origin of UHECR are questionable. The third argument is only valid for a proton composition, but not for iron cosmic rays. Only the fourth argument conclusively rules out a Galactic origin of UHECR, even for an iron composition.

Two further remarks are worth mentioning with regard to the search for extragalactic origins of UHECR. Firstly, the scientific community focusses on observing more UHECR and enlarging catalogues of source candidates, in order to calculate correlations between those arrival directions and source candidates. However, the main bottleneck is formed by the lack of knowledge about the Galactic magnetic field. All GMF models used in this thesis are capable of deflecting extragalactic iron cosmic rays up to 160°. These deflections need to be corrected for before attempting to calculate any correlation with extragalactic objects. Secondly, it has been shown that the UHECR flux from extragalactic sources which also occur in our own Galaxy is negligible compared to their Galactic counterpart. Since we have ruled out a Galactic origin of UHECR, this also rules out any extragalactic population of source candidates that occur in our Galaxy. We need to look for exotic extragalactic objects that do not occur in our own Galaxy.

Acknowledgements

I owe my largest intellectual debt to Prof. Dr. O. Scholten, Dr. P. Mertsch and Prof. Dr. S. Sarkar, who taught me how to be a physicist. I cannot express enough gratitude for the effort made by Prof. Dr. S. Sarkar and Prof. Dr. O. Scholten to make my dream of studying in Oxford come true. I would like to thank Xiaohui Sun for helping me understand his work, Brian Baughman & Mike Sutherland for helping me while working with CRT, and Martin Reinecke, Krzysztof Górski & Eric Hivon for helping me while working with HEALPix. I am grateful to Gwenael Giacinti for fruitful discussions about both our work, and helpful comments on this thesis. It is very much appreciated that William Hanlon, Ronnie Jansson, Glennys Farrar, Karl-Heinz Kampert, the American Astronomical Society, and many of the abovementioned persons permitted me to reproduce their figures. Corpus Christi College has provided a unique and stimulating academic environment; I have particularly valued the close contact with the Senior Common Room. I furthermore acknowledge financial support from the Huygens Scholarship Programme and the McKinsey & Company Grant.

Alessandra, Keru, Julian, Anne, Marloes, Nikita and Pierre, thank you for motivating and challenging me! Forgive me for having been so stressed near the end. A special thanks goes to Anne, for being my invaluable personal walking LaTeX manual. Last but definitely not least, I am very thankful for my family, who supported me and believed in me every step of the way.

Appendix A: CRT

Several codes for the propagation of cosmic rays are publicly available, such as GALPROP[1] [62], CRPropa[2] [63] and CRT[3] [64] (see also [12]). GALPROP is however more suited for the diffusive regime, whereas CRPropa simulates proton trajectories in Extragalactic Magnetic Fields only. We use CRT, which is suited for cosmic rays in the ballistic regime, for any user-specified composition. It furthermore has the option to choose from a wide range of GMF models and source types, and allows for user-specification of many simulation parameters. Energy losses are not considered (see [64] for a justification). CRT is a numerical tool written in C++ and has only a single dependency on the GSL random number generation libraries. It calculates the cosmic ray trajectories using 5th order adaptive Runge-Kutta integration routines; the step size is adapted at every step depending on the error tolerance specified by the user. Two different tracking methods are available: forwardtracking and backtracking. When opting for the former method, particles are injected at specified source positions and followed until they hit the Earth, which is represented by a detection disc of radius R (default 0.1 kpc) oriented orthogonal to the trajectory. Backtracking of a cosmic ray particle with charge q and arrival velocity $\vec{v}$ is accomplished by tracing the trajectory of the antiparticle with charge $-q$ injected at the Earth with an initial velocity $-\vec{v}$. Under the assumption of negligible energy losses, this will trace the trajectory of the original particle back in time, which provides information on possible source locations.

We have used adapted[4] versions of CRT Version 3.0 (which includes the ASS+RING model) and CRT Version 3.0.1 (which includes the regular components of the JF model; April 2012). The newest version (3.0.2, June 2012) includes the striated components of the JF model, but is not used in this thesis. In order to use the ASS+RING model, CRT requires the following space-separated input:

$$\text{F sun2008 ass+ring } p \ B_0 \ R_0 \ B_c \ R_c \ z_0 \ R_1^R \ R_2^R \ R_3^R \ B_0^H \ z_0^H \ z_{1a}^H \ z_{1b}^H \ R_0^H.$$

[1] http://galprop.stanford.edu/web_galprop/galprop_home.html

[2] http://apcauger.in2p3.fr/CRPropa/

[3] http://crt.osu.edu/; username: *public*; password: *tracker*

[4] The sign of the Halo field of Sun *et al.*'s models has been implemented incorrectly. The line

```
retval = (BH0 * (1./tdenom) * (r/RH0) * exp(-1.*((r-RH0)/RH0)));
```

should be changed into

```
retval = -1.*(BH0 * (1./tdenom) * (r/RH0) * exp(-1.*((r-RH0)/RH0)));
```

in the *halomag* function in the bfield_sun2008.h headerfile, followed by recompiling.

A description of these parameters, their values and units, can be found in Chapter 4.2.1. The required input corresponding to those parameter values is

F sun2008 ass+ring -12 2 10 2 5 1 7.5 6 5 2 1.5 0.2 0.4 4.

Since the ASS+ARM model is not available in the current version of CRT, we have added it. Our adjusted version of CRT requires the following input:

F sun2008 ass+arm p B_0 R_0 B_c R_c z_0 p^A $R^A_{0,inner}$ $R^A_{0,outer}$ $\phi^A_{0,inner}$ $\phi^A_{0,outer}$ B^H_0 z^H_0 z^H_{1a} z^H_{1b} R^H_0.

For the parameter values specified in Chapter 4.2.1, this corresponds to

F sun2008 ass+arm -12 2 8.5 2 5.3 1 12 3.2 3.5 57 0 2 1.5 0.2 0.4 4.

To add a dipole field, one needs to specify the strength of the magnetic field (in μG) at the position of the Sun, where the North Pole defines the positive direction:

protons: F dipole 5; *iron nuclei:* F dipole 1.

The syntax for the JF field is

F jf2012 sigma spiralscaler tornormscaler torzscaler xnormscaler xzscaler

where *sigma* specifies the allowed variation of the 21 parameters from their best fit values and the other options allow scalings of the separate field components. We use the model exactly as it is described in [3], with the best-fit values for the parameters:

F jf2012 0 1 1 1 1 1.

Two sources types are used: the P (point source) source type when forwardtracking and the C type when backtracking. The P type has the following syntax

P npsrc crshift crindex emin emax dsrc long lat beamangle pmass pcharge

which represents a point source emitting *npsrc* particles with mass *pmass* and charge *pcharge*. The particles are generated in a disk with size *crshift* (0) at a distance *dsrc* in the direction (*long, lat*) and injected with velocity vectors lying within a cone of angular size 2 x *beamangle* directed at the Earth, with an energy drawn from an energy spectrum $\propto E^{-crindex}$ ($E^{-2.7}$) ranging from *emin* (55 EeV) to *emax* (300 EeV). The C type has the following syntax

C energy long lat pmass pcharge

and represents the backtracking of a particle of mass *pmass* and charge *pcharge* that arrived at the Earth with energy *energy* from the direction (*long, lat*).

Four user-specifiable parameters determine the runtime (per hit) and accuracy: the maximum time a particle is being tracked, the maximum error allowed when performing the adaptive integration routine, the beam angle of point sources and the detector radius

R_{det}. The former two are left at their default values, 10^6 years and 10^{-8} respectively. We expect (especially for protons) that only particles which are emitted approximately in the direction of the Earth (i.e. with a small beam angle) will result in a hit. Setting the beam angle unnecessarily large will result in many irrelevant simulations. Hence, in Chapter 5 we set the beamangle to 90°. We will find out in Chapter 5.2 that a tiny fraction of particles emitted at a larger beam angle can still reach the earth. Although this has no consequences for the conclusions derived from that Chapter, the beam angle is conservatively set to the maximum value (i.e. emission in all directions) in Chapter 6. The radius of the detector significantly influences the number of hits. On the one hand, large statistics are required, especially when calculating the uncertainties in the dipole-anisotropy (see eqs. 2.5-2.9). However, the detector size needs to be small compared to the radius of curvature of the trajectories in order for the arrival directions to be accurate. The field strength at the Sun is ~ 2 μG for the three GMF models used, corresponding to a maximum gyroradius of ~ 1 kpc for iron nuclei. Keeping in mind that we do not aim to calculate a correlation with a detailed source catalogue but are interested in the rough distribution of arrival directions over the sky, a detector radius of 0.1 kpc is considered to form the optimal balance. Nevertheless, we use a larger size (0.5 kpc) in Chapter 5 to increase the number of hits. All simulations showing effects (i.e. latitudinal spread) from nearby sources (and samples from simulations with distant source effects) are repeated with $R_{det} = 0.1$ kpc. This choice of detector size allows us to check many scenarios within reasonable computing time and to reject all the scenarios incapable of reproducing the PAO events, although we risk wrongly accepting some scenarios. These scenarios will however be ruled out subsequently in Chapter 6 where $R_{det} = 0.1$ kpc is used unless mentioned otherwise.

Appendix B: Thesis related activities

Completed

- Presentation *Magnetars as possible sources of UHECR*, informal Corpus Christi College Graduate House Mini-Seminar (self-organised), 24 nov 2011.
- Brief summary of my research in Volume 16.2 of the Magazine *Francken Vrij* published by T.F.V. Professor Francken, the Study Assocation for Applied Physics at the University of Groningen.
- *Viva voce* at the KVI, University of Groningen, 22 August 2012.

In preparation

- Brief summary of my research in the Magazine *Periodiek* (year 2012, volume 2) published by the FMF, the Study Assocation for Physics & Mathematics at the University of Groningen.
- Full-length article in the Magazine *Periodiek* (year 2012, volume 3) published by the FMF, the Study Assocation for Physics & Mathematics at the University of Groningen.
- Chosen and sponsored for participation in the *Summer School and Workshop on the Standard Model and Beyond*, Corfu Summer Institute, Corfu, 8-17 September 2012.
- Presentation, Corpus Christi College MCR-SCR Seminar, 12 October 2012.
- Presentation, Particle Theory Journal Club, Oxford University, Michaelmas Term 2012.
- Full-length article, prepared for submission to peer-reviewed journal.

Bibliography

[1] A. Waelkens X.H. Sun, W. Reich and T.A. Enβlin. Radio observational constraints on galactic 3d-emission models. *Astronomy & Astrophysics*, 477, 2008.

[2] X.H. Sun and W. Reich. The galactic halo magnetic field revisited. *Research in Astronomy and Astrophysics*, 10(12), 2010.

[3] R. Jansson and G.R. Farrar. A new model of the galactic magnetic field. *Submitted to the Astrophysical Journal [arXiv:1204.3662v1]*, 2012.

[4] A. Letessier-Selvon. Ultrahigh energy cosmic rays. *arXiv:1103.0031v1*, 2011.

[5] Donald Perkins. *Particle Astrophysics*. Oxford University Press, 2009.

[6] J. Linsley. Evidence for a primary cosmic-ray particle with energy $10^{20}ev$. *Physical Review Letters*, 10(4), 1963.

[7] S. Sarkar. Ultrahigh energy cosmic rays & neutrinos. http://www-thphys.physics.ox.ac.uk/people/SubirSarkar/astropartphyslectures/astropart4b.pdf, july 2012.

[8] K. Fang, K. Kotera, and A.V. Olinto. Newly-born pulsars as sources of ultrahigh energy cosmic rays. *arXiv:1201.5197v1*, 2012.

[9] H. Takami and K. Sato. Distortion of ultra-high-energy sky by galactic magnetic field. *arXiv:0711.2386V1*, 2007.

[10] H. Takami and K. Sato. Does galactic magnetic field disturb the correlation of the highest energy cosmic rays with their sources. *arXiv:0909.1532v2*, 2010.

[11] H. Takami. Propagation of ultra-high-energy cosmic rays in galactic magnetic field. *arXiv:1104.0278v1*, 2011.

[12] A.R. Van Vliet. Ultra-high-energy cosmic rays in the galactic magnetic field. Master's thesis, KVI Theory Group/ University of Groningen, march 2011.

[13] N.M. Nagar and J. Matulich. Ultra-high energy cosmic rays detected by auger and agasa. *Astronomy and Astrophysics*, 523(A49), 2010.

[14] K. Nakamura. 24. cosmic rays. *JPG*, 37(075021), 2010.

[15] The Pierre Auger Collaboration. Correlation of the highest-energy cosmic rays with nearby extragalactic objects. *Science*, 318(938), 2007.

[16] The Pierre Auger Collaboration. Update on the correlation of the highest energy cosmic rays with nearby extragalactic matter. *Astroparticle Physics*, 34, 2010.

[17] The Pierre Auger Collaboration. Upper limit on the cosmic-ray photon flux above 10^{19} ev using the surface detector of the pierre auger observatory. *Astroparticle Physics*, 29, 2008.

[18] The Pierre Auger Collaboration. Upper limit on the cosmic-ray photon fraction at eev energies from the pierre auger observatory. *Astroparticle Physics*, 31, 2009.

[19] A.M. Hillas. The origin of ultra-high-energy cosmic rays. *Ann. Rev. Astron. Astrophys.*, 22, 1984.

[20] The Pierre Auger Collaboration. Correlation of the highest-energy cosmic rays with the positions of nearby active galactic nuclei. *Astroparticle Physics*, 29, 2008.

[21] The Pierre Auger Collaboration. Search for first harmonic modulation in the right ascension distribution of cosmic rays detected at the pierre auger observatory. *Astroparticle Physics*, 34, 2011.

[22] G. Giacinti *et al.* Cosmic ray anisotropy as signature for the transition from galactic to extragalactic cosmic rays. *JCAP*, 31, july 2012.

[23] K.M. Górski *et al.* Healpix: A framework for high-resolution discretization and fast analysis of data distributed on the sphere. *The Astrophysical Journal*, 622, 2005.

[24] P. Sommers. Cosmic ray anisotropy analysis with a full-sky observatory. *Astroparticle Physics*, 14, 2001.

[25] J. Aublin and E. Parizot. Generalised 3d-reconstruction method of a dipole anisotropy in cosmic-ray distributions. *A&A*, 441, 2005.

[26] J. Linsley. Fluctuation effects on directional data. *Physical Review Letters*, 34(24), 1975.

[27] N.W. Evans, F. Ferrer, and S. Sarkar. The anisotropy of the ultra-high energy cosmic rays. *Astroparticle Physics*, 17:319–340, 2002.

[28] K.-H. Kampert and M. Unger. Measurements of the cosmic ray composition with air shower experiments. *Astroparticle physics*, 35, 2012.

[29] The Pierre Auger Collaboration. Measurement of the depth of maximum of extensive air showers above 10^{18} ev. *Physical Review Letters*, 104(091101), 2010.

[30] N. Hayashida *et al.* The anisotropy of cosmic ray arrival directions around 10^{18} ev. *Astroparticle Physics*, 10, 1999.

[31] A. Calvez, A. Kusenko, and S. Nagataki. Role of galactic sources and magnetic fields in forming the observed energy-dependent composition of ultrahigh-energy cosmic rays. *PRL*, 105(091101), 2010.

[32] K. Greisen. End to the cosmic-ray spectrum? *Physical Review Letters*, 16(17), 1966.

[33] G.T. Zatsepin and V.A. Kuz'min. Upper limit of the spectrum of cosmic rays. *Journal of Experimental and Theoretical Physics Letters*, 4, 1966.

[34] G. Ghisellini, G.Ghirlanda, F. Tavecchio, F. Fraternali, and G. Pareschi. Ultra-high energy cosmic rays, spiral galaxies and magnetars. *Mon. Not. R. Astron. Soc.*, 390, 2008.

[35] K. Kotera. Ultrahigh energy cosmic ray acceleration in newly born magnetars and their associated gravitational wave signatures. *arXiv:1106.3060v1*, 2011.

[36] C. Kouveliotou, R.C. Duncan, and C. Thompson. Magnetars. *Scientific American*, February, 2003.

[37] R.C. Duncan and C. Thompson. Formation of very strongly magnetized neutron stars: Implications for gamma-ray bursts. *The Astrophysical Journal*, 392, 1992.

[38] R.C. Duncan. 'magnetars', soft gamma repeaters & very strong magnetic fields. http://solomon.as.utexas.edu/magnetar.html, march 2003.

[39] McGill Pulsar Group. Mcgill sgr/axp online catalog. http://www.physics.mcgill.ca/~pulsar/magnetar/main.html, july 2012.

[40] M. Broekroelofs. Uhecr acceleration in a magnetar wind using the concept of plasma wakefield acceleration. http://irs.ub.rug.nl/dbi/4d64ff56b8e56. Master's thesis, KVI Theory Group/ University of Groningen, feb 2011.

[41] J. Arons. Magnetars in the metagalaxy: An origin for ultrahigh-energy cosmic rays in the nearby universe. *The Astrophysical Journal*, 589, 2003.

[42] R.D. Blanford. Acceleration of ultra high energy cosmic rays. *Physica Scripta*, T85:191–194, 2000.

[43] W.R. Webber. A new estimate of the local interstellar energy density and ionization rate of galactic cosmic cosmic rays. *The Astrophysical Journal*, 506, 1998.

[44] M.S. Longair. *High energy astrophysics*. Cambridge University Press, 1981.

[45] M. Solway. Observational evidence for neutron stars. http://www.physics.rutgers.edu/~jackph/2010s/supp.html, march 2012.

[46] S. Mereghetti. The strongest cosmic magnets: Soft gamma-ray repeaters and anomalous x-ray pulsars. *arXiv:0804.0250v1*, 2008.

[47] N.D. Kylafis, I. Contopoulos, D. Kazanas, and D.M. Christodoulou. Formation and destruction of jets in x-ray binaries. *arXiv:1104.1578v1*, 2011.

[48] K.J. Hurley, B. McBreen, M. Rabbette, and S. Steel. The lognormal properties of the soft gamma-ray repeater sgr 1806-20 and the vela pulsar. *Astron.Astrophys.*, 288, 1994.

[49] L. Stella, S. Dall'Osso, and G.L. Israel. The giant flare of 2004 dec 27 from sgr1806-20 and fundamental physics from magnetars. *Mem. S.A.It.*, 80, 2009.

[50] B. Zink, P. D. Lasky, and K. D. Kokkotas. Are gravitational waves from giant magnetar flares observable? *arXiv:1107.1689v3*, 2011.

[51] L. Gualtieri, R. Ciolfi, and V. Ferrari. Structure, deformatioins and gravitational wave emission of magnetars. *arXiv:1011.2778v1*, 2010.

[52] Abadie *et al.* Search for gravitational wave bursts from six magnetars. *arXiv:1011.4079v2*, 2011.

[53] R. Beck. Galactic and extragalactic magnetic fields - a concise review. *Astrophys. Space Sci. Trans.*, 5:43–47, 2009.

[54] R. Beck. Galactic magnetic fields. *Scholarpedia*, 2(8):2411, 2007.

[55] S.A. Mao et al. A survey of extragalactic faraday rotation at high galactic latitude: the vertical magnetic field of the milky way toward the galactic poles. *The Astrophysical Journal*, 714:1170–1186, 2010.

[56] J.M. Cordes and T.J.W. Lazio. Ne2001.i. a new odel for the galactic distribution of free electrons and its fluctuations. *arXiv:astro-ph/0207156v3*, 2011.

[57] M. Prouza and R. Šmída. The galactic magnetic field and propagation of ultra-high energy cosmic rays. *Astronomy & Astrophysics*, 410:1–10, 2003.

[58] R. Jansson *et al.* Constraining models of the large scale galactic magnetic field with wmap5 polarization data and extragalactic rotation measure sources. *JCAP*, 021, 2009.

[59] M.S. Pshirkov *et al.* Deriving the global structure of the galactic magnetic field from faraday rotation measures of extragalactic sources. *The Astrophysical Journal*, 738(192), 2011.

[60] M. Ahlers, P. Mertsch, and S. Sarkar. Cosmic ray acceleration in supernova remnants and the fermi/pamela data. *Physical Review D*, 80(123017), 2009.

[61] M.P. Muno *et al.* A search for new galactic magnetars in archival *chandra* and *xmm-newton* observations. *The Astrophysical Journal*, 680(639), 2008.

[62] A.W. Strong and I.V. Moskalenko. Propagation of cosmic-ray nucleons in the galaxy. *The Astrophysical Journal*, 509, 1998.

[63] E. Armengaud *et al.* Crpropa: a numerical tool for the propagation of uhe cosmic rays, γ-rays and neutrinos. *Astroparticle Physics*, 28, 2007.

[64] M.S. Sutherland, B.M. Baughman, and J.J. Beatty. Crt: A numerical tool for propagating ultra-high energy cosmic rays through galactic magnetic field models. *Astroparticle Physics. See also* http://crt.osu.edu/., 34, 2010.